



TECHNISCHE
UNIVERSITÄT
WIEN

Vienna University of Technology

Dissertation

The role of coating architecture and diffusion on phase evolution and mechanical properties of Al-Cr-N and Ti-Al-N based materials

ausgeführt zum Zwecke der Erlangung des akademischen Grades eines Doktors der technischen
Wissenschaften / der Naturwissenschaften unter Leitung von

Univ.Prof. Dipl.-Ing. Dr. mont. Paul Heinz Mayrhofer

E308

Institut für Werkstoffwissenschaften und Werkstofftechnologie

eingereicht an der Technischen Universität Wien
Fakultät für Maschinenwesen und Betriebswissenschaften

von

Dipl.-Ing. Corinna Sabitzer

Matrikelnummer: 0530687
Launsdorf 2, 9314 Launsdorf, Österreich

Wien, am 13.11.2014

Diese Dissertation haben begutachtet:

.....

ACKNOWLEDGEMENT

I would like to thank Paul Mayrhofer for giving me the chance to write this thesis and collect great experiences, for his supervision, for all the helpful suggestions, for his patience and for everything I was able to learn from him.

I would also like to express my gratitude to all the people from Paul's coating group for the pleasurable working atmosphere and for having such a great time. Especially, I am deeply grateful to Christian, Fedor, Helmut, Holger, Liangcai, Matthias, Robert and Stefan for your great support and advice when I needed it and of course for all the great and funny moments during working as well as non-working activities.

Further on, I would like to express my thanks to my supervised student Christian for working hard on creating a very good diploma thesis. You did an excellent job.

I am very thankful for the great time at the Montanuniversität Leoben. Many thanks to all the friends I made there, as well as to all people of the Department of Physical Metallurgy and Materials Testing.

I would also like to express my thankfulness to all friends from Strutzi's Pub, who have been and are still there when I need them. I have made so many wonderful memories over the years and looking forward for even more.

DANKSAGUNG

Ein ganz besonderes Dankeschön gilt meiner Familie – meinen Eltern, Barbara und Willibald, meinem Bruder Christian, Sabine und meinen Großeltern – die mich stets in allem unterstützt und in schwierigeren Zeiten ermutigt haben. Ich bin sehr dankbar dafür Menschen wie euch in meinem Leben zu haben und zu wissen, dass ihr immer für mich da seid.

CONTENTS

1	<i>Introduction</i>	1
2	<i>Theoretical Background</i>	3
2.1	Deposition Techniques	3
2.1.1	Sputter deposition	3
2.1.2	Cathodic Arc Evaporation	5
2.1.3	Structure Zone Model (SZM)	7
2.2	Material Systems	9
2.2.1	Hard ceramic materials	9
2.2.2	Targets	10
2.2.3	Coatings	12
2.3	Material properties	15
2.3.1	Phase stability	15
2.3.2	Nucleation and growth	17
2.3.3	Spinodal decomposition	18
2.3.4	Strengthening Mechanisms	19
2.3.5	Diffusion	21
2.3.6	Atomistic Mechanisms of Diffusion	23
2.4	Characterization techniques	27
2.4.1	Chemical and structural Investigations	27
2.4.2	Mechanical Investigations	29
2.4.3	Thermal analyzes	30
3	<i>Reactive and non-reactive sputter deposition of Al-Cr-N coatings using metallic, intermetallic, and ceramic targets</i>	32
3.1	Introduction	32

3.2	Experimental	33
3.3	Results and Discussion	34
3.4	Summary and Conclusion	39
4	<i>Influence of bias potential and layer arrangement on structure and mechanical properties of arc evaporated Al-Cr-N coatings</i>	41
4.1	Introduction	41
4.2	Experimental	42
4.3	Results and Discussion	43
4.4	Summary and Conclusion	48
5	<i>Impact of bias potential and layer arrangement on the thermal stability of arc evaporated Al-Cr-N coatings</i>	50
5.1	Introduction	50
5.2	Experimental Details	51
5.3	Results and Discussion	53
5.3.1	As deposited structure and morphology	53
5.3.2	DSC and TGA investigations	54
5.3.3	Development of Structure with Annealing Temperature	59
5.3.4	Development of Mechanical Properties with Annealing Temperature	63
5.4	Discussion	65
5.5	Summary and Conclusion	67
6	<i>Diffusion behavior of C, Cr, and Fe in arc evaporated TiN- and CrN-based coatings and their influence on thermal stability and hardness</i>	69
6.1	Introduction	69
6.2	Experimental	70
6.3	Results and discussion	71
6.3.1	Morphology and structure	71
6.3.2	Hardness	77

6.3.3	Diffusion coefficients	79
6.4	Summary and Conclusion	85
7	<i>Summary and Contribution to the field</i>	87
8	<i>Acknowledgment for financial and experimental support</i>	90
9	<i>References</i>	91

Hard coatings like TiN, $Ti_{1-x}Al_xN$, CrN, and $Cr_{1-x}Al_xN$ synthesized by physical vapour deposition processes like cathodic arc evaporation or sputtering are widely used to protect tools in numerous machining and forming applications during which they have to sustain high temperatures and tribological loads. Their high usage is based on their excellent properties, such as high hardness, high thermal stability, high wear and oxidation resistance. It is well known that the coating performance can be tailored, for example, by the deposition parameters used – like partial pressure, gas mixture, bias potential, or temperature – or by the coating architecture (e.g. multilayer or even superlattice arrangements, graded composition, and defect or stress design by applying alternating bias potentials). However, also the target material itself can significantly influence the coating structure and thus the coating properties.

Therefore, we have studied the impact of specially developed targets – with a comparable Al/Cr ratio, powder metallurgically prepared from metallic Al and Cr, intermetallic Al_8Cr_5 , or ceramic AlN and CrN powder – on structure, morphology, mechanical properties, and thermal stability of reactively and non-reactively sputtered $Al_xCr_{1-x}N$ coatings. All reactively sputtered coatings exhibit a pronounced columnar structure with a preferred (111) orientation whereas the coating deposited non-reactively from the ceramic target is nanocrystalline with a preferred (200) orientation. Furthermore, the hardness is highest for this non-reactively sputtered nitride coating and the deposition rate is twice as high as for coatings reactively sputtered from metallic Al/Cr targets. Also the thermal stability, especially with respect to the onset of Cr-N dissociation, is shifted to higher temperatures for coatings prepared from ceramic targets.

Further on, monolithically grown as well as multilayered $Al_xCr_{1-x}N$ coatings were deposited by cathodic arc evaporation using metallic Al_xCr_{1-x} targets with compositions of $x = 0.7, 0.75, 0.85$, and 0.9 . Monolithically grown $Al_{0.7}Cr_{0.3}N$ and $Al_{0.75}Cr_{0.25}N$ coatings exhibit a single phase cubic structure. A mixed cubic/hexagonal structure is observed for $Al_{0.85}Cr_{0.15}N$, and a single phase hexagonal structure for $Al_{0.9}Cr_{0.1}N$ coatings. Multilayer variations, combining single phase cubic layers (using $Al_{0.7}Cr_{0.3}$ and $Al_{0.75}Cr_{0.25}$ targets) with the mixed

cubic/hexagonal (using $\text{Al}_{0.85}\text{Cr}_{0.15}$ targets) or hexagonal layers (using $\text{Al}_{0.9}\text{Cr}_{0.1}$ targets) show also hexagonal phase fractions in addition to the cubic phases when applying low bias potentials of -40 V. However, increasing the bias potential supports the coherency strains to suppress the growth of the less dense hexagonal phase. Therefore, even for a high overall Al/Cr ratio of 77/23 at% hardness values around 33 GPa are obtained.

However, the thermal stability, with respect to phase decomposition and Cr–N dissociation to cubic Cr under N_2 -release, is reduced by increasing the applied bias potential. Due to the reduced thermal stability, the hardness gain by increasing the bias potential is already lost for an annealing temperature ≥ 600 °C in (as deposited) single-phase cubic structured coatings. Therefore, the $\text{Al}_{0.7}\text{Cr}_{0.3}\text{N}$ coatings prepared with -40 V outperform their -120 V bias counterparts in hardness already for an annealing temperature ≥ 600 °C. This is different for the multilayer coatings comprising cubic and hexagonal wurtzite type phases. Especially for $\text{Al}_{0.75}\text{Cr}_{0.25}\text{N}/\text{Al}_{0.9}\text{Cr}_{0.1}\text{N}$ multilayers the increased bias during deposition helps to prepare dense coatings and the arrangement with high Al-containing layers allows for an improved resistance against decomposition and Cr–N dissociation.

As nitride thin coatings are exposed to very high temperatures during metalworking the diffusion of C, Cr, and Fe – which are common transfer – elements during machining – into such TiN, $\text{Ti}_{0.5}\text{Al}_{0.5}\text{N}$, CrN, and $\text{Cr}_{0.3}\text{Al}_{0.7}\text{N}$ coatings is studied. Our results show that the mechanical properties of nitride thin coatings are not always negatively influenced by the inward-diffusion of such foreign elements. For example, the hardness of TiN is nearly unaffected by the diffusion of C, Cr, and Fe up to 1000 °C and 30 min. It was shown that especially C and Cr exhibit almost 15 and 10 times larger diffusion coefficients in $\text{Ti}_{0.5}\text{Al}_{0.5}\text{N}$ than in TiN coatings. In CrN, C exhibits an even up to 35 times larger diffusion coefficient than in $\text{Cr}_{0.3}\text{Al}_{0.7}\text{N}$. Based on our results we can conclude that microstructural changes within coatings significantly determine diffusion processes. The diffusion of C, Cr, and Fe is more pronounced within $\text{Ti}_{0.5}\text{Al}_{0.5}\text{N}$ than in TiN but less pronounced within $\text{Cr}_{0.3}\text{Al}_{0.7}\text{N}$ than in CrN.

ZUSAMMENFASSUNG

Durch physikalische Gasphasenabscheidung hergestellte Hartstoffschichten, wie z.B. TiN, $\text{Ti}_{1-x}\text{Al}_x\text{N}$, CrN, und $\text{Cr}_{1-x}\text{Al}_x\text{N}$, werden heute aufgrund ihrer ausgezeichneten Eigenschaften häufig zum Schutz von Werkzeugen vor hohen Temperaturen und tribologischen Beanspruchungen während dem industriellen Einsatz verwendet. Die Eigenschaften solcher Schichten sind von zahlreichen Faktoren abhängig und können unter anderem durch Verwendung unterschiedlich hergestellter Target Materialien, Variationen der Beschichtungsparameter sowie durch die Abscheidung unterschiedlicher Schichtarchitekturen optimiert werden.

Um den Einfluss des Target Materials auf die Eigenschaften reaktiv- und nicht-reaktiv gesputterter $\text{Al}_x\text{Cr}_{1-x}\text{N}$ Schichten zu untersuchen wurden pulvermetallurgisch hergestellte, metallische Al/Cr, intermetallische Al_8Cr_5 bzw. keramische AlN und CrN Targets verwendet. Die durch reaktives Sputtern hergestellten Schichten weisen unabhängig vom verwendeten Target Material, eine ausgeprägte stängelige Struktur mit bevorzugter (111) Orientierung auf. Durch die Verwendung keramischer Targets im nicht-reaktiven Sputter-Prozess wurden hingegen Schichten mit nanokristalliner Struktur und bevorzugter (200) Orientierung hergestellt. Der nicht-reaktive Prozess führte neben einer Verdopplung der Beschichtungsrate im Vergleich zu den reaktiven Prozessen, auch zur Abscheidung der Schichten mit der höchsten Härte. Zusätzlich konnte durch die Verwendung keramischer Targets die thermische Stabilität der Schichten bzw. jene Temperatur, bei der die Cr-N Zersetzung beginnt, erhöht werden.

Für die Abscheidung unterschiedlicher $\text{Al}_x\text{Cr}_{1-x}\text{N}$ Schichten mittels Lichtbogenverdampfung wurden pulvermetallurgisch hergestellte $\text{Al}_{0.7}\text{Cr}_{0.3}$, $\text{Al}_{0.75}\text{Cr}_{0.25}$, $\text{Al}_{0.85}\text{Cr}_{0.15}$ und $\text{Al}_{0.9}\text{Cr}_{0.1}$ Targets verwendet. Die daraus resultierenden $\text{Al}_{0.7}\text{Cr}_{0.3}\text{N}$ und $\text{Al}_{0.75}\text{Cr}_{0.25}\text{N}$ Schichten weisen eine einphasige kubische Struktur auf. Dagegen zeigen $\text{Al}_{0.85}\text{Cr}_{0.15}\text{N}$ Schichten eine zweiphasige kubische/hexagonale Struktur und $\text{Al}_{0.9}\text{Cr}_{0.1}\text{N}$ Schichten eine einphasige hexagonale Struktur. Des Weiteren wurden diese einphasigen, kubischen Lagen mit gemischten kubisch/hexagonalen oder hexagonalen Lagen zur Abscheidung verschiedener Multilagenschichten kombiniert. Dabei führt das Anlegen einer geringen Biasspannung von -

40 V, zu Multilagenschichten die sowohl hexagonale als auch kubische Phasenanteile aufweisen. Durch Erhöhung der Biasspannung kann das Wachstum der hexagonalen Phase, die ein höheres spezifisches Volumen einnimmt als die kubische, unterdrückt werden. Dies unterstützt die Al-ärmeren kubischen Lagen, durch Kohärenzspannungen, die Al-reicheren Lagen ebenfalls in die kubische Struktur zu zwingen. Dadurch ist es möglich, dass auch bei einem sehr hohen durchschnittlichen Aluminium/Chrom Verhältnis von 77/23 at%, nahezu einphasige kubische Schichten mit sehr hohen Härtewerten von bis zu 33 GPa hergestellt werden können.

Gleichzeitig wird aber die thermische Stabilität der einphasigen kubischen Schichten durch Erhöhung der Biasspannung verringert. Zum Beispiel geht der durch erhöhte Biasspannung erzielte Härteanstieg der $\text{Al}_{0.7}\text{Cr}_{0.3}\text{N}$ Schichten bereits ab Glühtemperaturen $\geq 600\text{ }^{\circ}\text{C}$ verloren. Deshalb besitzen jene $\text{Al}_{0.7}\text{Cr}_{0.3}\text{N}$ Schichten, die mit einer Biasspannung von -40 V hergestellt wurden, bereits ab Glühtemperaturen $\geq 600\text{ }^{\circ}\text{C}$ höhere Härtewerte als Schichten gleicher Zusammensetzung, die mit einer Biasspannung von -120 V hergestellt wurden.

Im Allgemeinen sind solche Hartstoffschichten während ihres Einsatzes in der zerspanenden Industrie sehr hohen Temperaturen ausgesetzt, was unter anderem zur Diffusion von C, Cr, und Fe führen kann. Deshalb wurde in dieser Studie auch das Diffusionsverhalten dieser Elemente in TiN, $\text{Ti}_{0.5}\text{Al}_{0.5}\text{N}$, CrN und $\text{Al}_{0.7}\text{Cr}_{0.3}\text{N}$ Schichten und deren Einfluss auf die Schichteigenschaften untersucht. Es konnte gezeigt werden, dass die mechanischen Eigenschaften dünner Schichten durch Diffusion nicht notwendigerweise negativ beeinflusst werde, da z.B. die Härte von TiN auch nach dem Vakuumglühen bei $1000\text{ }^{\circ}\text{C}$ nicht durch die Eindiffusion von C, Cr, oder Fe verringert wird. Detaillierte Untersuchungen haben auch gezeigt, dass die Diffusionskoeffizienten in den unterschiedlichen Schichten sehr stark variieren. Im Speziellen besitzen C und Cr nahezu 10 bzw. 15 mal höhere Diffusionskoeffizienten in $\text{Ti}_{0.5}\text{Al}_{0.5}\text{N}$ - als in TiN-Schichten. Dies lässt sich hauptsächlich auf die deutliche Änderung der Mikrostruktur der $\text{Ti}_{0.5}\text{Al}_{0.5}\text{N}$ Schichten infolge thermischer Behandlung zurückführen. Auch in CrN Schichten besitzt C bis zu 35 mal höhere Diffusionskoeffizienten als in $\text{Al}_{0.7}\text{Cr}_{0.3}\text{N}$ Schichten. Diese Ergebnisse zeigen, dass Diffusionsprozesse in dünnen Schichten hauptsächlich von der Mikrostruktur der Schichten und damit auch von deren thermischer Stabilität bestimmt werden.

CHAPTER 1

Introduction

Thin film deposition technology and science have progressed rapidly in the last decades as coatings became indispensable from a wide range of industrial applications (e.g. machining, in automotive, aerospace, electronical, and medical industries). They can completely change the mechanical, electrical, optical, and thermal properties of substrates and surfaces and thus, are used to protect them from tribological loads, corrosive environment, and chemical exposure.

Especially, transition metal nitrides, such as TiN or CrN and transition metal aluminum nitrides, such as $\text{Ti}_{1-x}\text{Al}_x\text{N}$ and $\text{Cr}_{1-x}\text{Al}_x\text{N}$ are of great interest in the metal forming and machining industry due to their outstanding properties, like high hardness, high thermal stability, and high wear and oxidation resistance [1–7]. Thereby, the Al content plays an important role regarding the coating properties [8–11]. Up to a critical AlN content the coatings crystallize in their metastable single phase cubic structure. Exceeding this critical AlN content will result in the formation of a dual phase structure, cubic and hexagonal (wurtzite-type) phases, or even in a single phase wurtzite structure, with generally decreased mechanical properties and coating performance.

Furthermore, virtually every property of the coating is related to and can be adjusted by the deposition process (e.g. physical vapor deposition processes like sputtering and arc evaporation or chemical vapor deposition processes) and the deposition parameters used (partial pressure, temperature, bias potential, gas mixture, and many more) [12–15].

The ever increasing demand for further improving properties lead to the deposition of multilayer or even superlattice coatings as they enable a pronounced increase in hardness, toughness and oxidation resistance [16–21]. Thereby, the additional interfaces act as barriers for dislocation movement and increase the mechanical properties. Further on, the interfaces provide obstacles for crack propagation and contribute to increased fracture toughness.

For machining applications high thermal- and oxidation stability is essential, as depending on physical and chemical properties of the work-piece and cutting tool material temperatures of more than 1000 °C are obtained at the cutting edge [22]. These high temperatures result in diffusion processes and thereby promote material transfer between cutting tool, coating, and work-piece, which is detrimental for the coating performance, as especially diffusion driven wear can be severe.

Therefore, the focus of this thesis is on modifying properties of $\text{Al}_x\text{Cr}_{1-x}\text{N}$ coatings by varying the deposition process, deposition parameters, and coating architecture. Moreover, diffusion studies of C, Cr, and Fe in Cr- and Ti-based nitride coatings were conducted.

In chapter 2 a short introduction to the used material systems, their properties and related characterization techniques, and deposition processes is given. As coating properties can be modified in various different ways, in chapter 3 the influence of the target material and deposition process – in terms of reactively and non-reactively sputtering – onto the microstructure and properties of $\text{Al}_x\text{Cr}_{1-x}\text{N}$ coatings is discussed. In chapters 4 and 5 the influence of the bias potential and multilayer arrangement on $\text{Al}_x\text{Cr}_{1-x}\text{N}$ coatings is considered. While in chapter 4 the structure and mechanical properties in the as deposited state of monolithically grown and multilayered $\text{Al}_x\text{Cr}_{1-x}\text{N}$ coatings is described, in chapter 5 their thermal stability and high temperature properties are discussed. As nitride thin coatings are widely used in the machining industry where they are exposed to high temperatures and tribological loads, diffusion in such coatings becomes interestingly. Thus, In chapter 6 the diffusion behaviour and the influence of C, Cr, and Fe onto the structure and mechanical properties of TiN, $\text{Ti}_{0.5}\text{Al}_{0.5}\text{N}$, CrN, and $\text{Al}_{0.7}\text{Cr}_{0.3}\text{N}$ coatings is described. Chapter 7 provides a short summary and conclusion of the main findings.

Theoretical Background

2.1 Deposition Techniques

Nowadays, physical vapor deposition (PVD) is one of the most important techniques for depositing thin protective coatings on a broad variety of technical relevant substrates. One of the biggest advantages is that it enables the deposition of virtually every kind of inorganic materials, e.g. metals, alloys, compounds as well as some organic materials. The main steps in PVD processes are (i) the creation of the vapor phase, (ii) the transfer of the vapor from the source to the substrate and (iii) the condensation of vapor and nucleation and growth onto the substrate [23,24].

2.1.1 Sputter deposition

As already mentioned above, the creation of the vapor phase is a main step within PVD processes. During sputtering this is realized by bombarding the target material by energetic particles (ions), provided by a glow discharge (plasma), see Fig. 2.1.1. First, the chamber is evacuated and subsequently a working gas – typically argon – is inserted. To ignite the plasma a high voltage has to be applied to the target. Once the plasma is ignited and stable Ar^+ is accelerated towards the negatively charged cathode, hitting the target material atoms which results in collision cascades as well as in implantation within the target material. As a consequence atoms are ejected from the target and move – due to the momentum gain – to the substrate on the opposite, forming the thin film.

Additionally, a negative bias potential can be applied to the substrates, allowing to control the bombarding process/efficiency during film growth and hence, modifying the morphology and in further consequence coating properties [23,24].

Reactive sputter deposition

Typically, electrically conducting target materials, mainly metallic targets are used in sputtering processes making powering the magnetron much easier as other alternatives. However, this limits the variety of coating materials that can be deposited. Therefore, a reactive gas like oxygen or nitrogen can be added during the deposition, forming oxide, nitride, and oxynitride hard coatings [23–25]. The chemical reactions to form the compounds all take place at surfaces, like chamber walls, targets, and substrates. Reactions in the gaseous state are unlikely as during the collision of two atoms in the gas phase it is not possible to conserve energy and momentum. However, surfaces – target or substrate – provide conserving energy and momentum as well as a longer interaction time between the atoms. Reactions on the substrates are favored, as reactions on the target lead to poisoning of the target and as a consequence the deposition process is affected and deposition rates are drastically reduced. A benefit of the reactive sputtering process is that with variation of the partial pressure of the reactive gas, the stoichiometry of the deposited film can be adjusted.

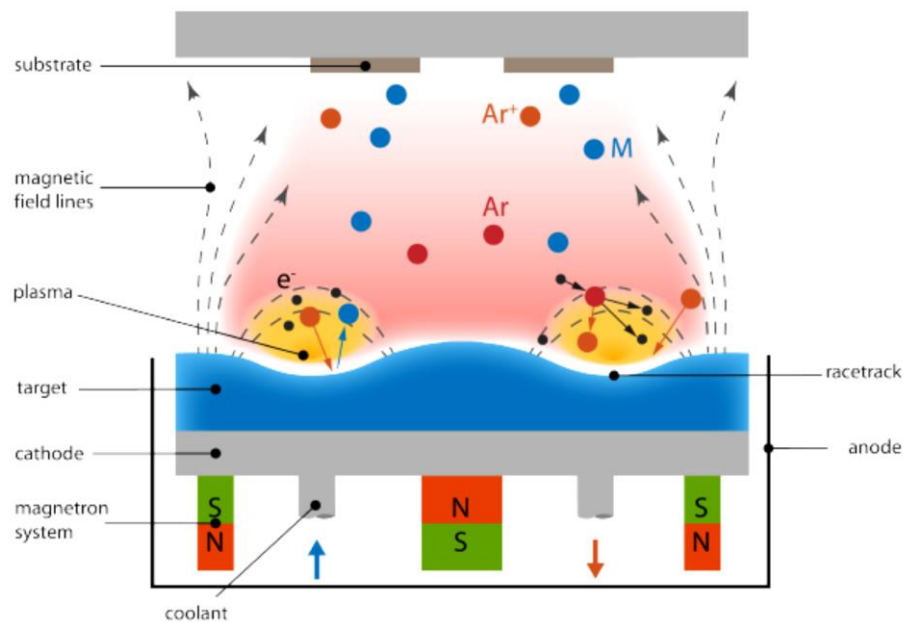


Fig. 2.1.1: Schematic of a typical magnetron sputtering system [26].

2.1.2 Cathodic Arc Evaporation

Cathodic arc evaporation uses low discharge voltages in the range of 20-100 V and high currents between ~ 30 A up to several kA to heat and thereby vaporize the target material [24,27,28]. The arc discharges are characterized by collective electron emission and are typically focused on a small area, called cathode spot (shown in detail in Fig. 2.1.2) which moves over the target surface with velocities of 1-100 m/s. As a consequence of surface heating by ion bombardment and electron current molten tracks appearing on the target surface from which mainly ionized target material as well as macroparticles, so called droplets, are ejected, compare Fig. 2.1.2. Hence, within the cathode spot all phases of matter – solid, liquid, gas, plasma – can be found.

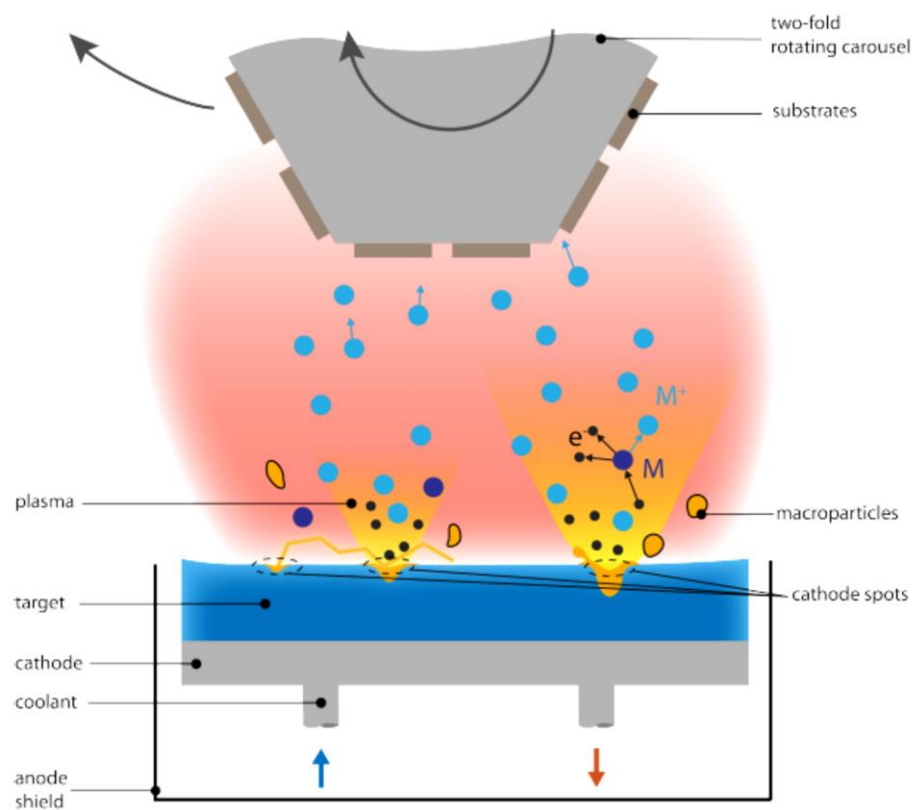


Fig. 2.1.2: Schematic of a cathodic arc evaporation process [26].

Basically, three types of cathode spots can be distinguished depending on the target material, namely type 1 and 2 spots on metals as well as type 3 spots on semi- and non-metals [27]. While at the beginning of arc operations – on contaminated surfaces – type 1

spots are typical, the spot changes to type 2 when contaminations are removed from the surface due to spot motion. During reactive deposition arc spots work mainly via type 1 or a mixture of type 1 and 2. Type 3 spots are characterized by significantly smaller spot velocities than for type 1 or 2, even with the tendency to getting stuck at the same site on the targets surface. However, the spot motion can either occur randomly or steered. Randomly means that the location of ignition of a new emission site moves in the absence of an external magnetic field. In the presence of an external magnetic field the ignition of emission locations is steered, avoiding deviations from random motion due to preferred ignition sites like scratches, located surface contaminations, and interface to a different material. Further on, spot steering results in increased spot velocities as well as decreased spot residence time and consequently, in less and smaller droplets [24,27].

Macroparticles

As mentioned afore, during cathodic arc evaporation the ejection of droplets from the cathode spot is possible as between the cold solid cathode and the hot plasma a transition zone of liquid cathode material exists [24,27]. This liquid zone is subject of varying plasma pressure and once it yields to the plasma pressure, macroparticles are ejected. Generally, droplets are liquid when they are formed and cool down on their way to the substrate. Once they arrive on the substrate they can either be incorporated to the growing coating, affecting further film growth, see Fig. 2.1.3a or reflected and cause a defect. Typical sizes of droplets are in the range between $\sim 0.1 \mu\text{m}$ and $\sim 10 \mu\text{m}$ but the caused defect is even larger as film growth is affected by the droplets, see Fig. 2.1.3b [24]. Depending on the application of the coatings, these droplets not necessarily influence the coating performance negatively [29]. However, due to resulting inhomogeneous density and defect sites (see Fig. 2.1.3b), thermal stability and oxidation behavior might be deteriorated as additionally diffusion pathways are provided [29,30].

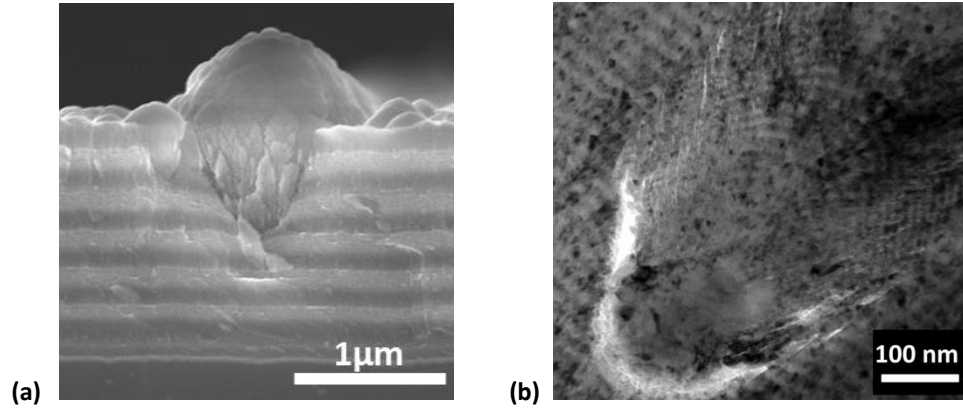


Fig. 2.1.3: Cross sectional (a) SEM image and (b) TEM image of a droplet in a AlCrN multilayer coating

Reactive arc evaporation

In contrast to sputtering, where target poisoning is undesired due to significantly decreased deposition rates and arcing, arc spot ignition during arc evaporation is desirable. As a consequence of the compound layer formed on the target surface in the presence of a reactive gas, arc ignition and type 1 cathode spots are promoted by the local high electric field strength. As a consequence, fewer and smaller droplets are ejected and additionally, macroparticle incorporation to the film might further be reduced due to their interaction with the reactive gas [27].

2.1.3 Structure Zone Model (SZM)

Structure zone models are used to illustrate the effect of deposition parameters onto the film structure in a simplified way. Within the first SZM – introduced by Movchan and Demchisin [25] – which was developed for thick evaporated coatings, the film thickness is plotted against the homologous temperature given by T_s/T_m (T_s is the substrate temperature and T_m is the melting temperature of the deposited coating). They concluded that three zones can be distinguished:

Zone 1, which corresponds to the temperature range $T_s/T_m < 0.3$, is characterized by a fine fibrous under-dense or amorphous microstructure as a consequence of low ad-atom mobility and limited surface diffusion. At higher temperatures $0.3 < T_s/T_m < 0.5$ zone 2 films are formed as a consequence of increasing surface diffusion. The film is composed of homogenous columnar crystals with similar orientation, resulting in a faceted surface. With

increasing T_s , the grain size increases, while the porosity decreases. For $T_s/T_m > 0.5$ bulk diffusion is decisive resulting in a recrystallized and dense film with large grains, this is zone 3.

Barna and Adamik [31] used slightly different temperature ranges and in agreement with Thornton [12] a fourth zone, called zone T (transition zone), located between zone 1 and zone 2, is indicated. In this transition zone, surface diffusion is observable but grain boundary migration is limited. The film shows a fine crystalline structure at the substrate and V-shaped grains further away from the substrate. In the upper part of thick coatings, the grains can also be columnar. Further on, they stated that process induced segregations of co-deposited impurities or additive species should be considered.

However, during the film deposition also the process pressure significantly influences the obtained microstructure. This was taken into account by Thornton [12] who observed that with increasing inert gas pressure the transition temperatures between the individual structure zones increase. As a consequence of an increased pressure the mean free path for collisions between the inert gas atoms and the sputtered atoms is decreased. Thereby, the energy of the deposition flux is reduced and hence further external energy is needed (i.e., heating of the substrate)

Messier et al. [32] suggested a modified SZM, substituting the pressure axis by an ion energy axis. Increasing the bias potential applied during the deposition process increases the ion flux onto the substrate. As a consequence ad-atom mobility is increased, shifting the transition between the individual zones to lower T_s/T_m values.

Anders [33] further considered plasma and ion effects on the film growth and used a generalized temperature E^* axis which includes the homologous temperature plus a temperature shift due to the potential energy of particles arriving on the surface, see Fig. 2.1.4. In addition, the pressure axis is replaced by a logarithmic axis of the normalized energy, considering displacement and heating effects caused by the kinetic energy of impinging particles. It is shown, that deposition rates are decreased with increasing particle energies due to re-sputtering effects and film densification. A further increase in E^* however, results in a negative film thickness. This means that the number of re-sputtered atoms exceeds the number of arriving atoms and is called ion etching.

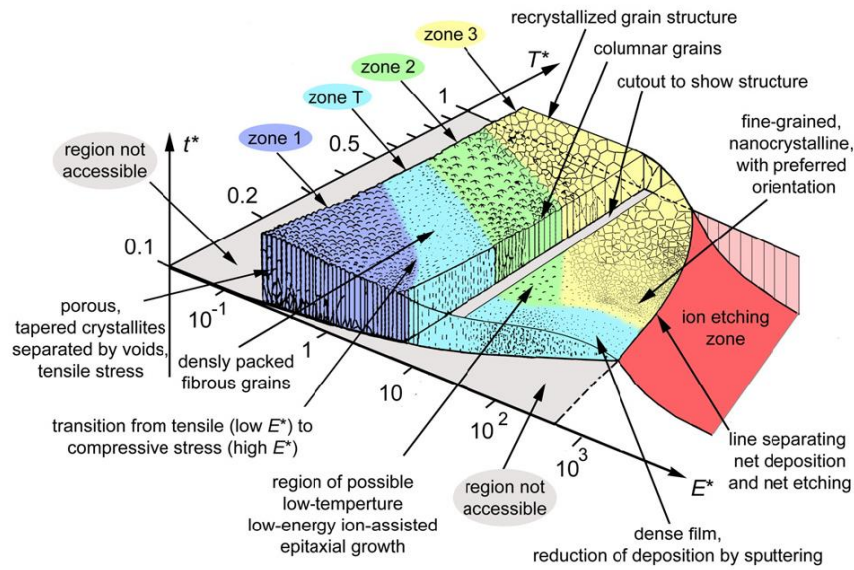


Fig. 2.1.4: Structure zone diagram according to Anders et al. [33].

2.2 Material Systems

2.2.1 Hard ceramic materials

According to Holleck [17], hard materials can be classified by their predominant bonding character and divided into three groups: metallic, covalent, and ionic hard materials, see Fig. 2.2.1. Further on, Vepřek [34] proposed that materials can be distinguished by their hardness into “normal” hard materials with Vickers hardnesses above 20 GPa, “super-hard” materials with hardnesses above 40 GPa, and “ultra-hard” materials exhibiting hardnesses above 70 GPa.

Transition metal nitrides (TMN's), such as TiN and CrN, deposited within this thesis, belong to the group of metallic hard-materials and have a strong covalent component to their metallic and ionic bonding, which is responsible for their good mechanical and chemical properties. The metallic contribution results in electrical conductivity. Further on, this component provides a certain degree of ductility and a good adhesion to the substrates. The covalent and ionic components however cause the high hardness and thermal stability.

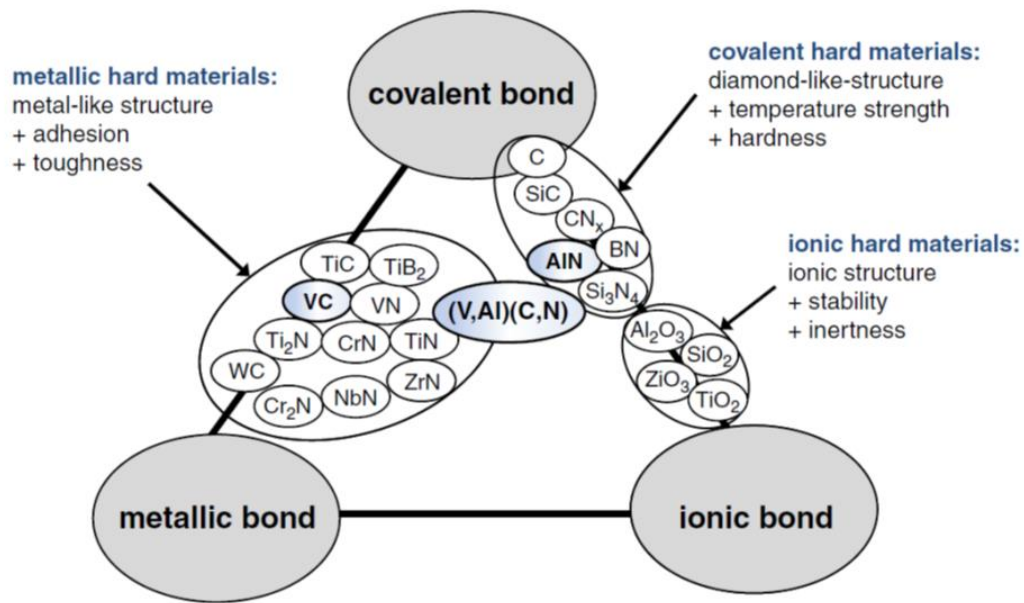


Fig. 2.2.1: Classification of hard ceramic coatings depending on their bonding character and its influence on their properties [17,35].

2.2.2 Targets

Targets used for the deposition of thin hard coatings should be as homogeneous as possible as well as pure as the desired film, as any atom in the target will contribute to the resulting coating. Homogeneity through the target thickness as well as diameter is important to avoid compositional variations with target erosion. Since for example, during sputtering nearly the entire power used leads to target heating, high thermal conductivity of the target is desired to transfer this heat to the cooling plates. Further on, a good thermal contact between the target and the cooling water has to be provided to remove the generated heat during the deposition process [23]. The targets used in arc evaporation require sufficient electrical conductivity to carry the arc current. If the conductivity is too low, high voltage drops, resulting in heating of the target. Typically, cathodic arc evaporation is limited to metals. However, there are also sufficiently conducting semiconductors and semi-metals used successfully [27]. Further on, during arc evaporation, ohmic heating might lead to expansion that brittle materials cannot accommodate. Hence, if brittle materials are used as target materials, during cathodic arc evaporation, they might fracture [27].

As porous targets typically have lower thermal conductivity the proper target manufacturing process has to be chosen. It has been shown that the target manufacturing process also has an influence on the defect density within the thin film [36].

Metallic $\text{Al}_x\text{Cr}_{1-x}$ targets, conventionally prepared by Al and Cr powder, are nowadays commonly used in both, sputter deposition and cathodic arc evaporation processes. Ceramic targets, such as TiN have successfully been used in sputter deposition, resulting in considerably higher deposition rates as compared to conventional reactive magnetron sputtering from a metallic Ti target. Thereby, stoichiometric coatings with extremely high hardness values, depending on the ion/atom flux ratio and the ion energy during deposition are obtained [37]. Thus, we used ceramic AlN/CrN_x targets to deposit $\text{Al}_x\text{Cr}_{1-x}\text{N}$ coatings. Detailed investigations on these coatings are given in Chapter 3. However, the aim was also to use such ceramic targets in the cathodic arc evaporation process. As ceramic materials inherently are more brittle than metals and also less conductive the arc gets stuck, already near the ignition site (see Fig. 2.2.2a), and crack formation is observed. Hence, it was not possible to synthesize coatings using the AlN/CrN_x target during arc evaporation.

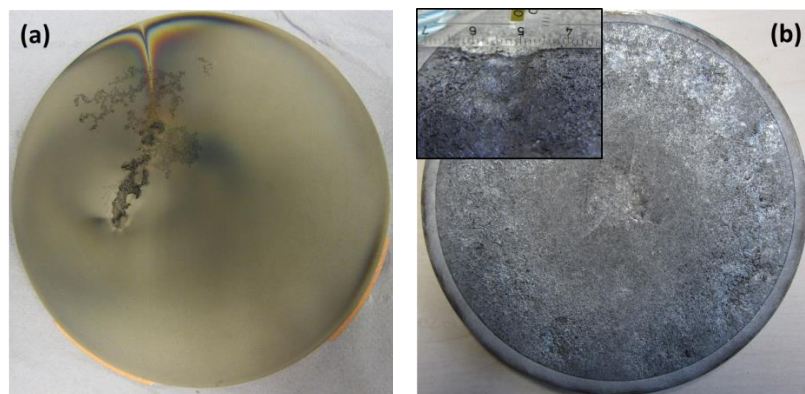


Fig. 2.2.2: Surface of (a) the ceramic target and (b) the intermetallic target after arc evaporation.

Further on, the Al_8Cr_5 phase was chosen to prepare the intermetallic target, which has been used successfully in sputter deposition (details are given in Chapter 3). We also wanted to use this target material for arc evaporation, as the high melting point indicates for a lower macroparticle density. However, intermetallic materials are known for their high strength and brittle behaviour and thus, the arc leads to delamination of parts of the target material and to cracking of the target, see Fig. 2.2.2b.

2.2.3 Coatings

2.2.3.1 Transition metal nitrides

Due to their attractive properties like high hardness, high thermal stability as well as high wear and oxidation resistance, transition metal nitrides are highly valued in industry as protective coatings. Typically they are used in automotive, aerospace, medical, electronic, and machining industries. Additionally, they are applied as diffusion barriers or even as decorative coatings, such as TiN due to its golden color.

CrN coatings are widely used as hard, protective and wear resistant coatings in e.g. metal forming or plastic molding operations as they combine low brittleness with high oxidation resistance and chemical inertness [38,39]. During the deposition process, the phase formation is mainly influenced by the N_2 pressure in the chamber. Thus, Cr-N coatings can consist of Cr, Cr_2N , and CrN phases. Coatings crystallizing in the single phase face centered cubic (fcc) CrN structure, exhibit a hardness of about 18 GPa [40], while hexagonal (h)- Cr_2N coatings show hardnesses of about 27 GPa [41]. Further on, CrN coatings start to dissociate into c-Cr and N_2 via the formation of h- Cr_2N if they are exposed to temperatures above 1000 °C in He atmosphere [42]. The high oxidation resistance of CrN coatings is related to the formation of a Cr_2O_3 layer on the coating, preventing the film underneath from further oxidation. TiN coatings typically crystallize in the fcc NaCl type structure having high hardnesses between 31 and 37 GPa, depending on the deposition conditions [14,43]. Further on, such coatings exhibit an outstanding high thermal stability in inert gas. Due to these properties, TiN is widely used as wear protective and corrosion resistant coating material on cutting tools and as diffusion barriers in semiconductor devices [2,44,45]. If TiN is exposed to high temperatures in ambient air it starts to oxidize at ~500-550 °C and forms a TiO_2 layer [46].

2.2.3.2 Transition metal aluminum nitrides ($Ti_{1-x}Al_xN$)

Due to the limited oxidation resistance of TiN, which already oxidizes at 550 °C, and to further improve the cutting performance of such coatings, Knotek et al. [7] and Münz [5] introduced the deposition of quasibinary $Ti_{1-x}Al_xN$ coatings. Despite the increased oxidation resistance of $Ti_{1-x}Al_xN$ coatings it was expected that they exhibit increased hardness as

compared to their binary counterparts. This is based on the formation of a supersaturated metastable solid solution with different electronic configurations and different atomic radii. The formation of such supersaturated metastable $\text{TM}_{1-x}\text{Al}_x\text{N}$ coatings by PVD is enabled by the limited kinetics due to high deposition rates and high cooling rates [47]. A further extensively studied $\text{TM}_{1-x}\text{Al}_x\text{N}$ coating material is $\text{Cr}_{1-x}\text{Al}_x\text{N}$ [6,11,48–50].

In general, the structure and properties of such $\text{TM}_{1-x}\text{Al}_x\text{N}$ coatings are closely related to their AlN content x , see Fig. 2.2.3 [9,51]. For $\text{Ti}_{1-x}\text{Al}_x\text{N}$ and $\text{Al}_x\text{Cr}_{1-x}\text{N}$ coatings it is observed that they crystallize in the single phase cubic (NaCl B1 type, c) structure for AlN contents (x) up to ~ 0.67 and 0.7 , respectively. For higher AlN contents a dual phase structure composed of cubic and hexagonal (ZnS B4 wurtzite-type, w) phases, or even the formation of a single phase w-structure is promoted. These typically exhibit decreased mechanical properties and decreased coating performance as their single-phase counterparts.

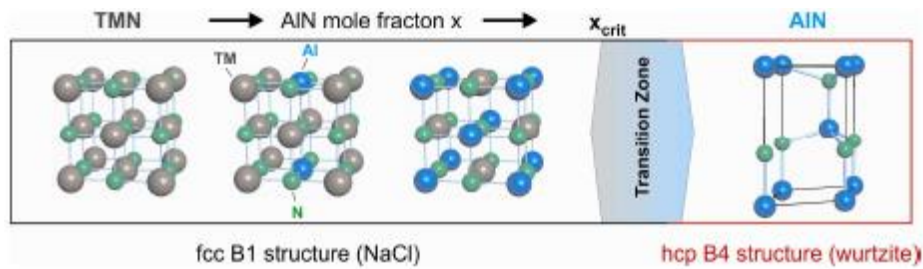


Fig. 2.2.3 Schematic of the structural evolution of $\text{TM}_{1-x}\text{Al}_x\text{N}$ coatings as a function of the AlN mole fraction. The critical AlN content for transition from the cubic to the hexagonal structure differs for different TMs [52].

Depending on the AlN content within single phase cubic structured $\text{Cr}_{1-x}\text{Al}_x\text{N}$ coatings, high hardnesses of about 38 GPa can be obtained [50]. For coatings with an AlN content of ~ 0.7 , which is close to the critical AlN for a single phase cubic structure, a slight hardness increase with increasing annealing temperature to 900 °C is observed, related to the precipitation of w-AlN. With further increasing the annealing temperature, the coatings decompose towards w-AlN and c-Cr via h-Cr₂N under nitrogen release. This is accompanied with a significantly decreasing hardness and hence, limits the thermal stability of such coatings to ~ 900 °C [49,53]. The hardness of single phase cubic structured $\text{Ti}_{1-x}\text{Al}_x\text{N}$ coatings is typically higher, ~ 40 GPa, than that of $\text{Cr}_{1-x}\text{Al}_x\text{N}$. Further on, $\text{Ti}_{1-x}\text{Al}_x\text{N}$ is capable of pronounced age hardening during service based on spinodal decomposition processes. Thereby, chemical

fluctuations result in the formation of AlN- and TiN- rich coherent regions in the temperature range 700-950 °C, which is connected with a hardness increase. A further increase in annealing temperature leads to the formation of c-TiN and w-AlN phases followed by grain coarsening and thus in a significant hardness drop [54]. However, $\text{Cr}_{1-x}\text{Al}_x\text{N}$ coatings show a significantly better oxidation resistance than $\text{Ti}_{1-x}\text{Al}_x\text{N}$ coatings as both, Cr and Al form protective oxides, leading to the formation of a dense Cr_2O_3 - Al_2O_3 outer layer and thus, preventing further oxidation of the nitride coating underneath [51]. On the other hand, on $\text{Ti}_{1-x}\text{Al}_x\text{N}$ coatings the formation of an Al_2O_3 + TiO_2 oxide layer is observed where the presence of TiO_2 limits the protection of the nitride coating underneath [55].

2.2.3.3 Multilayer arrangements

For ceramic bulk materials, it was found out that a fine grained multi-phase structure with a high phase boundary density results in increased toughness and fracture resistance [56]. Similar observations were made for coatings, where interfaces were introduced due to the deposition of ceramic/ceramic and metal/ceramic multilayer architectures. Further on, also compositionally graded films or defect or stress design by applying alternating bias potentials result in optimized coating performances [16,56–63].

The hardness increase due to the layered structure of e.g. CrN/AlN multilayer coatings is due to the additional interfaces formed, resulting in variations of the stress/strain field. Thereby, dislocation mobility is limited and hence increased mechanical properties compared to monolithically grown coatings are obtained [19,20,64,65]. The individual layers also exhibit different shear moduli and therefore, different dislocation line energies. The dislocations prefer to remain within the layer with the lower shear modulus and hence, an increased stress is required to move the dislocations in the layer with the higher shear modulus [66]. Further on, multilayer architectures enable to stabilize AlN layers in their metastable cubic structure as it has been shown for the CrN/AlN multilayer system which is based on coherency strains between alternating CrN and AlN layers [19,20,64,65].

However, the increased number of interfaces provided by the multilayer arrangements can reduce the thermal stability compared with their monolithically grown supersaturated $\text{Al}_x\text{Cr}_{1-x}\text{N}$ counterparts [49,67].

2.3 Material properties

2.3.1 Phase stability

Basically, the Gibbs free energy (G) of a system is a measure of its stability and is defined as:

$$G = H - TS, \quad (2.1)$$

where H is the enthalpy, T is the absolute temperature and S is the entropy of a system [68]. At constant temperature and pressure, this system is in its stable equilibrium state if G becomes minimal ($dG=0$), illustrated in Fig. 2.3.1 as configuration A. However, there is also the possibility that G exhibits a local minimum – hence, also fulfills the condition $dG=0$ – but not reveals its lowest possible value, see Fig 2.3.1 configuration B. In this case, the system is in a metastable equilibrium state as it is commonly known for PVD synthesized coatings [47]. The limited atomic reassembling during low-temperature PVD processes even allows to prepare thermodynamically instable materials such as $Ti_{1-x}Al_xN$ [69] and $Cr_{1-x}Al_xN$ [48] exhibiting even negative second derivatives of the Gibbs free energy. A transformation to the stable state is possible – like any transformation, which lowers the Gibbs free energy – if diffusion allows for these processes and/or the energy barrier between these states (when starting from a metastable state) is overcome. Thus, annealing of cubic structured c- $Cr_{1-x}Al_xN$ and c- $Ti_{1-x}Al_xN$ coatings leads to their decomposition into their stable constituents via nucleation and growth [49,70] and spinodal decomposition [54,71], respectively.

As already mentioned afore a chemical reaction or phase transformation can occur if thereby energy is gained or stability is acquired, thus G is minimized. This is the case if the difference between the free enthalpies before the reaction (G_1) and after the reaction (G_2) is negative, $\Delta G = G_2 - G_1 < 0$.

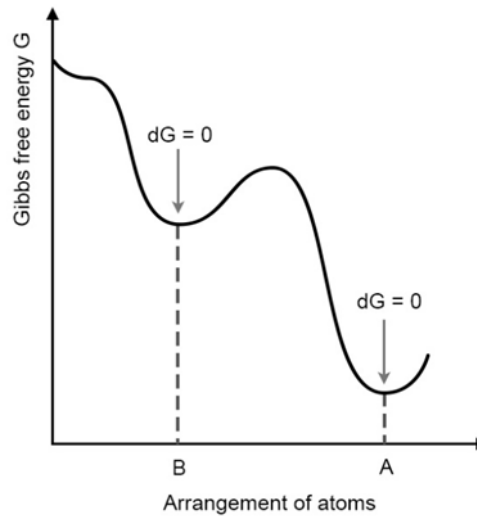


Fig. 2.3.1: Development of Gibbs free energy in dependence of the atom arrangement.

For a binary solid solution of A and B atoms, the stability can be described by the mixing enthalpy ΔG_{mix} :

$$G_2 = G_1 + \Delta G_{mix}, \quad (2.2)$$

where

$$\Delta G_{mix} = \Delta H_{mix} - T\Delta S_{mix}. \quad (2.3)$$

The free energy change on mixing a regular solution is shown in Fig. 2.3.2 for different values of Ω and temperature, with $\Omega = N_a z \epsilon$. Here, N_a is the Avogadro number, z is the number of bonds per atom, and ϵ is the difference between the A–B bond energy, and the average of the A–A and B–B bond energies.

The phase stability is determined by negative ΔG_{mix} values. The $-T\Delta S_{mix}$ term is always negative, but ΔH_{mix} can either be positive (if energy is lost) or negative (if energy is gained), due to the formation of two AB-bonds out of one AA- and one BB-bonding. If ΔH_{mix} is negative, the compound is stable at high and low temperatures, see Figs. 2.3.2a and b. However, if ΔH_{mix} is positive, the temperature determines the stability of the compound. At high temperatures ΔG_{mix} is nevertheless negative (Fig. 2.3.2c), and hence the compound is stable whereas at low temperatures ΔG_{mix} gets positive for certain compositional ranges (Fig. 2.3.2d). Thus, decomposition will occur in order to minimize the overall free energy of the system either by nucleation and growth or by spinodal (spontaneous) decomposition.

The latter will take place in the composition range, where the second derivative of the Gibbs free energy is negative.

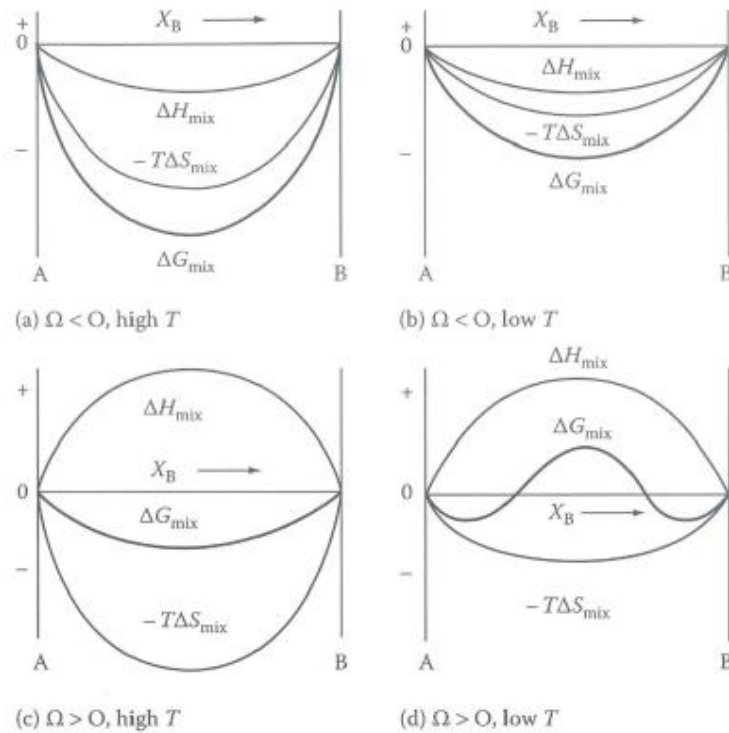


Fig. 2.3.2: The effect of ΔH_{mix} and T on ΔG shown for (a, b) negative ΔH_{mix} values and (c, d) for positive ΔH_{mix} values [68]

2.3.2 Nucleation and growth

Considering a solid solution where a B-rich β is incoherently precipitated from an A-rich α , then the free energy change due to the nucleation process is given by

$$\Delta G = -V\Delta G_V + A\gamma + V\Delta G_S. \quad (2.4)$$

The free energy is decreased by the formation of a volume V of β by $V\Delta G_V$, while it is increased by the energy for the formation of a new interface between the precipitate and matrix γ of an area A and the misfit strain energy ΔG_S per unit volume of β . Here, β has already its final composition at the beginning of precipitation. By differentiation of Eq. 2.4 a critical minimum radius of

$$r^* = \frac{2\gamma}{(\Delta G_V - \Delta G_S)} \quad (2.5)$$

is obtained in case of a globular nucleus.

In Fig. 2.3.3 the contribution of the individual energy contributions with increasing radius on the minimization of the free enthalpy is shown.

As a representative c-Al_xCr_{1-x}N is mentioned, decomposing towards w-AlN and c-Cr via the formation of h-Cr₂N under the release of nitrogen when exposed to thermal treatment [49,70].

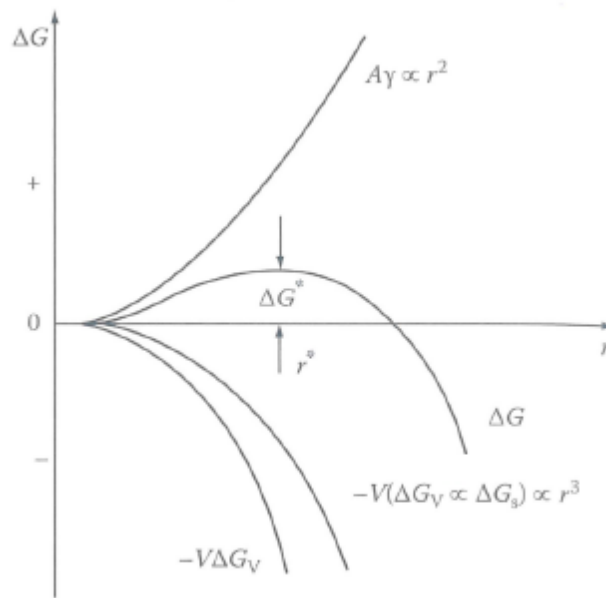


Fig. 2.3.3: The free energy change due to nucleation of an incoherent precipitate of radius r . ΔG^* and r^* indicate the critical free energy and radius for a stable precipitate [68].

2.3.3 Spinodal decomposition

In contrast to the decomposition via nucleation and growth, for spinodal decomposition no energy barrier has to be overcome. Alloys with compositions between the spinodal are unstable and able to decompose into coherent phases via chemical fluctuations as soon as diffusion allows for it, which intensify therefore with aging time. These chemical fluctuations reach their final composition only at the end of the decomposition. The free energy change accompanying the formation of fluctuations is given by:

$$\Delta G = \Delta G_c + \Delta G_\gamma + \Delta G_s, \quad (2.6)$$

where ΔG_c is the free energy change if an alloy of composition X_0 decomposes into two parts with the compositions $X_0 + \Delta X$ and $X_0 - \Delta X$, respectively, ΔG_γ is the energy change due to interfacial energy effects, known as 'gradient energy', and ΔG_s is the coherency strain energy term as a result of differences in the atom sizes within the solid solution.

In Figure 2.3.4 the schematic phase diagram of a system with miscibility gap is shown. In region 1 the solid solution is stable and no decomposition occurs. Below the incoherent miscibility gap, region 2, nucleation of incoherent precipitates and growth is possible. When also considering the formation of coherency strains, which have to be overcome, nucleation of coherent precipitates will occur in region 3, below the coherent miscibility gap and spinodal decomposition will take place within the coherent spinodal, region 4 [68,72].

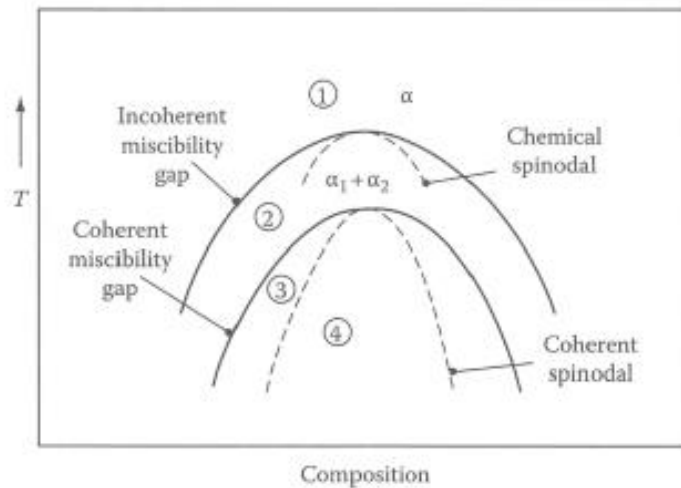


Fig. 2.3.4: Schematic phase diagram for a clustering system [68].

2.3.4 Strengthening Mechanisms

Usually the hardness of a material is defined as its resistance against local plastic deformation. In crystalline solids such a plastic deformation is a consequence of dislocation movement under applying an external stress to the material. It is obvious that any imperfection within the crystal lattice might hinder dislocation movement. To continue the dislocation movement the applied force has to be increased and thus, the material is strengthened. This dislocation movement can be obtained by gliding or climbing processes.

The basic types of dislocations are edge dislocations, see Fig. 2.3.5a, and screw dislocations, see Fig. 2.3.5b.

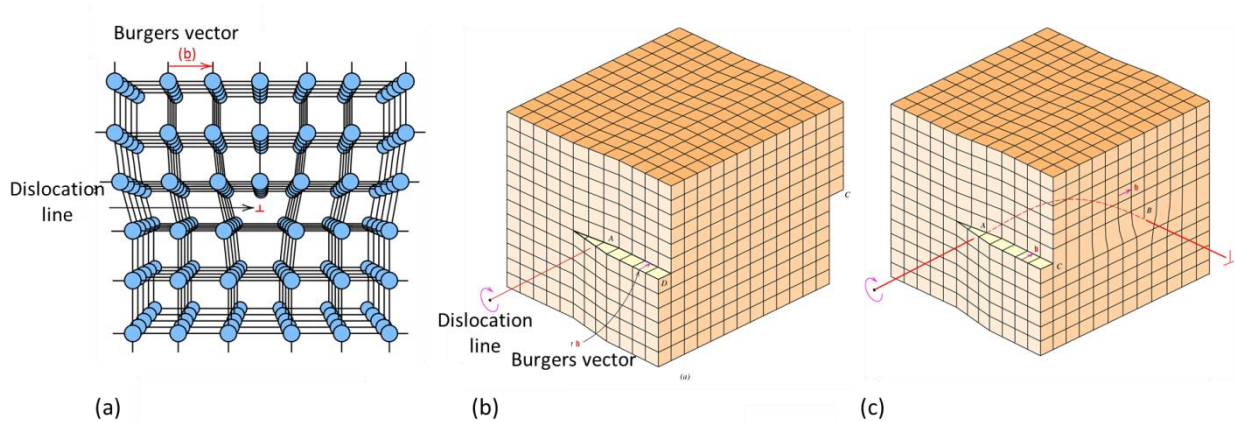


Fig. 2.3.5 (a) Edge dislocation, (b) screw dislocation, and (c) mixed dislocation in a crystal lattice [73].

An edge dislocation is a defect where a half plane of atoms is introduced to the crystal lattice. Along the end of this half plane, so-called dislocation line (Fig. 2.3.5a), local lattice distortions exist. The gliding of dislocations is only possible in slip planes having the same Burgers vector (describing the magnitude and direction of dislocations), see Fig. 2.3.5, which is in case of an edge dislocation perpendicular to the dislocation line. Screw dislocations can be visualized by a shear stress applied to the crystal resulting in distortion. As shown in Fig. 2.3.5b the upper part of the crystal is then shifted one atom distance to the right, relative to the bottom part. The dislocation line and the Burgers vector are then parallel to each other. However, in most crystalline materials mixed dislocations, having both, edge and screw components, are present, Fig. 2.3.5c. The Burgers vector stays the same but the vector of the dislocation line changes.

The movement of any dislocation having a Burgers vector different from zero is linked with their motion on slip planes. However, screw dislocations are able to cross slip and change their slip planes. Climbing processes of edge dislocations, to change their slip planes, need lattice defects and their diffusion, thus they need a higher thermal activation.

Commonly, strengthening in metallic materials during plastic deformation is a result of an increase in the dislocation density and the interaction between the dislocations. Once a dislocation, moving through the crystal under an external applied stress, encounters an

obstacle, the stress has to be increased to continue its movement and the material is strengthened. This can also be obtained by increase the grain boundary density, hence by reduction of the grain size. As typically adjacent grains exhibit different crystallographic orientations and grain boundaries are characterized by an irregular arrangement of atoms, an increased stress is required for dislocation movement from one grain into the neighboring. The correlation between the increased strengthening and the grain size d is given by the well-known Hall-Patch relation [72]:

$$\sigma_Y = \sigma_0 + \frac{k}{\sqrt{d}} \quad (2.7)$$

where σ_Y is the yield stress, describing the onset of plastic deformation, and σ_0 and k are material constants. It has to be noted that this relation is not valid for coarse-grained and very fine grained materials. Further on, the incorporation of interstitial or substitutional foreign atoms into the crystal lattice results in an increased strength or hardness of the material, known as solid solution strengthening. Thereby the strengthening effect is increased with increasing concentration of the foreign atom species [72,73]. For example, the addition of Al to CrN results in an increasing hardness of such coatings [50]. The formation of fine and homogenously distributed particles of another phase within a matrix can for certain materials also result in strengthening and hardening. In general, this is achieved by thermal treatment of a supersaturated solid solution. Also during annealing of $\text{Al}_x\text{Cr}_{1-x}\text{N}$ coatings a hardness increase with annealing temperature is observed due to the precipitation of w-AlN particles [53].

2.3.5 Diffusion

The coatings prepared within this work CrN, TiN, $\text{Cr}_{1-x}\text{Al}_x\text{N}$, and $\text{Ti}_{1-x}\text{Al}_x\text{N}$ are often used as protective coatings on tools for numerous machining and forming applications such as cutting inserts, dies, or molds due to their outstanding properties. During such applications temperatures of more than 1000 °C are obtained in the contact area between the cutting tool and work-piece, depending on physical and chemical properties of the work-piece material and cutting tool material, cutting parameters and cutting tool geometry, see Fig. 2.3.6. Due to these high temperatures, diffusion driven processes (phase transformations

and decomposition, microstructural changes) as well as material transfer between cutting tool, coating, and work-piece may occur which can be detrimental for the coating performance. Thus, it is necessary to derive a basic understanding of the fundamentals of diffusion.

The driving force for diffusion is always to minimize the Gibbs free energy, hence to transform the system from a non-equilibrium to the equilibrium state and to eliminate concentration differences. This can either occur by diffusion down the concentration gradient, where atoms diffuse from regions of high concentration to regions of low concentrations, or by diffusion up the concentration gradient, where atoms move towards regions of high concentrations. Representatively for the latter one is supersaturated $\text{Ti}_{1-x}\text{Al}_x\text{N}$, that decomposes via spinodal decomposition towards TiN and AlN .

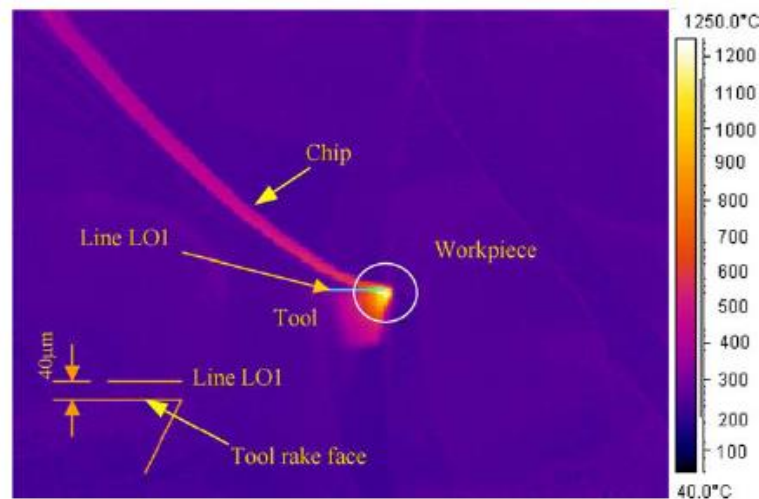


Fig. 2.3.6 Temperature distribution in work piece, tool and chip during steel cutting [22].

In Fick's first law of diffusion, the flux of a diffusing species J is connected with the concentration gradient by [68]:

$$J = -D \frac{\partial c}{\partial x} \quad (2.8)$$

where J denotes the flux of the diffusing species, c the concentration per unit volume, x the direction of diffusion, and D – as a proportionality factor – the Diffusion coefficient [cm^2/s].

The negative sign considers that the flux goes from regions of high concentrations to regions of low concentrations.

As in most practical applications the concentration variation with both distance and time is relevant, non steady state diffusion is considered in Fick's second law of diffusion as a combination of Fick's first law of diffusion (Eq. 2.8) and the equation of continuity ($\frac{\partial c}{\partial t} + \frac{\partial j}{\partial x} = 0$). It can be written as [68]:

$$\frac{\partial c}{\partial t} = D \frac{\partial^2 c}{\partial x^2} \quad (2.9)$$

if the diffusion coefficient is independent of the concentration.

In case of a thick top layer and a constant surface concentration (infinite diffusion source) the solution of Ficks's second law can be written as [68]:

$$c(x, t) = C_s \left[1 - \operatorname{erf} \left(\frac{x}{2\sqrt{Dt}} \right) \right] \quad (2.10)$$

Here, one possible solution of the medium diffusion distance relevant for the diffusion of an infinite source (not depleting) into a material is [68]:

$$x = 2\sqrt{Dt}. \quad (2.11)$$

2.3.6 Atomistic Mechanisms of Diffusion

Atom jump processes are fundamental phenomena for diffusion in solids. Basically, the atoms are oscillating around their equilibrium positions, which are positions of minimum potential energy. Once the displacement is large enough, mainly due to thermal input, the atom can jump into an adjacent vacancy or interstitial site. The energy which is required to overcome this barrier is known as the activation energy for migration, G_m , see Fig. 2.3.7.

The jump frequency Γ , is given by [68]:

$$\Gamma = z\nu \exp \frac{-G_m}{RT} \quad (2.12)$$

where z is the number of sites to which a jump can occur and v is the vibration frequency of the atoms around their equilibrium position. An atom makes v attempts per second to jump into a neighboring site and the fraction of successful jumps is given by $(-G_m/RT)$.

The diffusivity D is defined as [68]

$$D = \frac{1}{6} \alpha^2 \Gamma \quad (2.13)$$

where α is the jump distance. Combining Eq. 2.12 with 2.13 and considering that $G_m = H_m - TS_m$, where H_m and S_m are the enthalpie and entropie of migration, the diffusion coefficient can be written as [68]:

$$D = \left[\frac{1}{6} \alpha^2 z v \exp \frac{S_m}{R} \right] \exp \frac{-H_m}{RT} \quad (2.14)$$

This can be simplified to the well-known Arrhenius equation for diffusion:

$$D = D_0 \exp \frac{-Q}{RT} \quad (2.15)$$

where the pre exponential factor D_0 is a constant, independent of the temperature, and Q is the activation energy (migration enthalpy H_m) for diffusion.

There are two common mechanisms by which atom diffusion through a solid can occur, interstitial or substitutional diffusion, shown in Fig. 2.3.7.

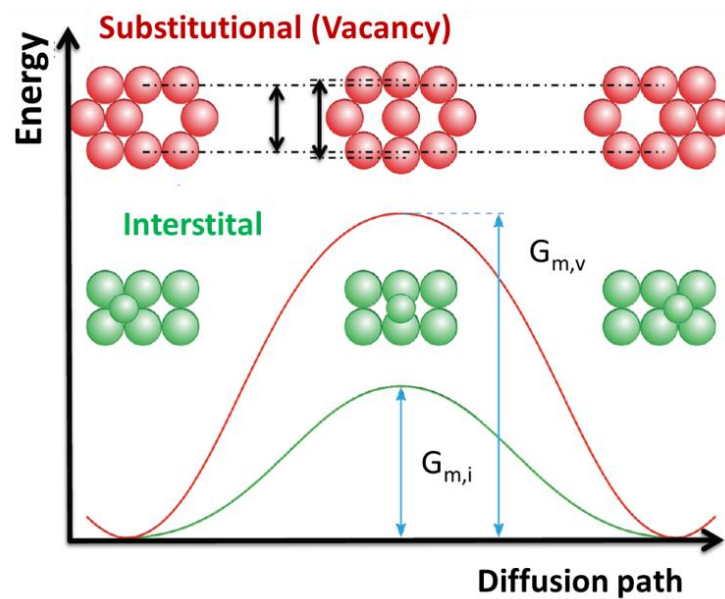


Fig. 2.3.7: Schematic of a substitutional and interstitial atomic jump process and the corresponding variation of the free energy [74].

In case of a considerably smaller solute atom within a host lattice, this atom occupies interstitial sites, preferably in octahedral sites, between the host lattice atoms and jumps after thermal activation into an unoccupied interstitial site, see Fig. 2.3.8.a and b. In general, the interstitial atom concentration is so low, that there are always unoccupied sites available for diffusion. In substitutional solid solutions most of the neighboring sites are occupied, hence, a higher barrier has to be overcome. As the diffusion of substitutional atoms into vacancies is equal to the motion of vacancies onto atom sites it is often referred to as vacancy diffusion, Fig. 2.3.8c. Further on, diffusion can occur via exchange- and collective mechanisms. Thereby, specific point defects, such as Frenkel- and Schottky defects might occur due to the atom movement. The latter one occurs as a pair of positively and negatively charged vacant lattice sites in highly ionic materials, such as in transition metal nitrides, and provides an overall neutral charging of the crystal. The Frenkel defect forms when an atom leaves its regular position becoming an interstitial and creating a substitutional vacancy. Direct exchange of positions between atoms (Fig. 2.3.8d) and a ring mechanism (Fig. 2.3.8e), in which atoms rotate in closed circles are energetically less favourable mechanisms due to the encountering of high activation barriers.

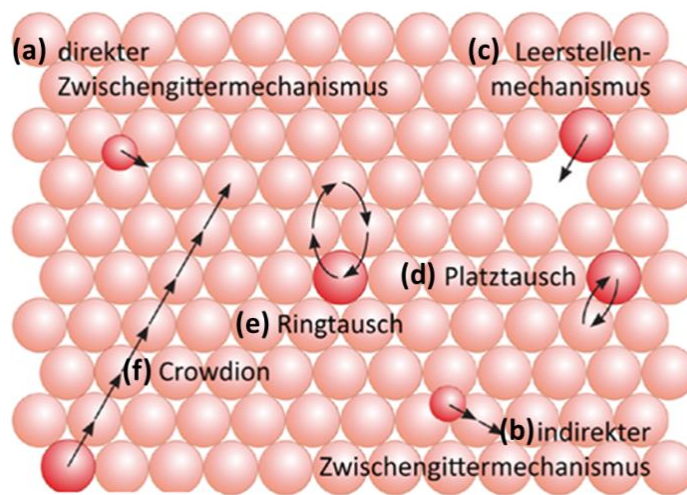


Fig. 2.3.8: Various possible exchange mechanism: (a) directly and (b) indirectly interstitial diffusion mechanism, (c) vacancy diffusion, (d) direct exchange of atoms, (e) ring mechanism, (f) crowdion [74].

Diffusion along high diffusivity paths

Free surfaces, grain- and phase boundaries, and dislocations are all present in real crystals and associated with lower packing densities as within the lattice itself. Thus, the atom movement along such disorders is much easier and takes place with lower activation energies than within the lattice. As a consequence, diffusion coefficients are significantly higher in these high-diffusivity paths than for lattice diffusion and follow the order: $D \ll D_d \leq D_{gb} \leq D_s$, where D denotes the lattice diffusivity, D_d dislocation diffusivity, D_{gb} grain boundary diffusivity, and D_s surface diffusivity.

From Eq. 2.15 it is obvious that the diffusion coefficient is highly sensitive to the temperature and the activation energy. At low temperatures, the low activation energies for atoms in high-diffusivity paths enhance their diffusion. At temperatures below $0.5 \cdot T_m$ (melting point temperature) grain boundary diffusion is noticeable and therefore important in polycrystalline materials with high melting points, like ceramics or intermetallic compounds. At high temperatures, the fraction of grain boundaries and dislocations is reduced due to grain growth and defect annihilation and thus, lattice diffusion is promoted [72,75].

Diffusion in thin films

Diffusion measurements in thin nitride films are of great interest due to their widespread application in wear-protective coatings, but are, however, difficult to perform. This is based on e.g. their high melting points. Additionally, thin films are typically metastable and often non-stoichiometric and contain impurities or growth-induced defects depending on the deposition processes. Thus, diffusion is obviously of different nature in thin films than in bulk materials. There are several data published focusing on nitride coatings like TiN, TaN, and WN acting as copper diffusion barriers [76–78]. However, all of them propose that the diffusion mainly occurs along high diffusion pathways such as grain and especially column boundaries and therefore strongly depends on the deposition parameters used. In ref. [79] a comprehensive collection of diffusion data for self-diffusion and diffusion of foreign atoms in nitride thin films is given.

2.4 Characterization techniques

2.4.1 Chemical and structural Investigations

2.4.1.1 XRD

X-ray diffraction analysis is a commonly used, non-destructive technique to obtain information about the structure of materials. Thereby, electromagnetic radiation like X-rays, are elastically scattered on periodically arranged atoms in crystalline solids. Constructive and destructive interference are fundamental phenomena of X-ray diffraction. The maximum intensity in the diffraction pattern is observed for constructive interference, given by the Bragg's equation [80]:

$$n\lambda = 2d\sin\theta, \quad (2.16)$$

where d is the lattice plane distance between adjacent planes, λ is the incident wave length, 2θ is the angle between the incident X-ray and the detector, and n is the order of interference.

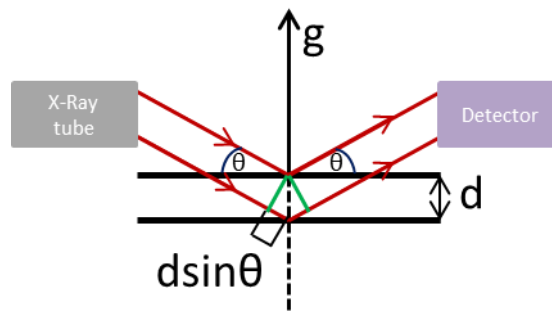


Fig. 2.4.1 Schematic of the experimental set up of a X-ray diffractometer during Bragg diffraction.

A typical measurement set up is shown in Fig. 2.4.1. The incident beam is scattered at lattice planes and then leaves the crystal. If the x-rays are scattered at different parallel lattice planes constructive interference can occur and the data are collected by the detector. In general, every material exhibits a unique diffraction pattern, depending on the crystal structure and lattice constants, allowing for its identification.

2.4.1.2 SEM

The scanning electron microscopy is based on the interaction of high energetic electrons with the sample. Thereby, the electron beam, emitted from the cathode is accelerated towards the sample by electrical field forces and focused by magnetic lenses. Once the electron beam hits the sample, electrons can either be elastically scattered, inelastically scattered, reflected, or cause secondary electrons and/or electromagnetic radiation. The latter ones are most commonly used for imaging and are generated due to the inelastic interaction of the primary beam electrons with the valence electrons of the atoms in the sample. Hence, they exhibit relatively low energies and originate from surface near regions. Back scattered electrons, which are elastically scattered and exhibit similar energies as the primary electrons, can also be used for imaging. These electrons originate from a larger excited volume. As backscattering becomes increased with increasing atom number, mass contrast imaging is possible. Further on, element specific x-rays are emitted when electrons from an inner shell are ejected and the electron holes are re-occupied by electrons from an outer shell. These characteristic x-rays can be used for chemical element analysis [81].

2.4.1.3 TEM

Transition electron microscopy can be used for investigations in the nanometer scale as even higher resolutions can be obtained as within the SEM. For TEM investigations the samples have to be thin enough to allow transmission of electrons. Therefore, the samples are mechanically grinded and polished to a few micrometers and subsequently Ar ion polished within a precision ion polishing system (PIPS). Basically, the contrast within a TEM image is achieved by the difference in atomic numbers of compound elements as well as by the crystal structure and its orientation with respect to the incident electron beam. Thereby, heavier atoms appear darker than lighter ones and crystals longitudinal to the beam appear bright. Similar to the SEM also within the TEM, EDX analysis are possible by measuring characteristic x-ray energies [81].

2.4.2 Mechanical Investigations

2.4.2.1 Nanoindentation

Nowadays nanoindentation is commonly used to determine the Hardness (H) and Indentation Modulus (E) of thin and hard coatings. During indentation tests the resistance of a material against penetration by a defined diamond indenter, which is typically a Berkovich indenter (three-sided pyramid with an included half angle of 65.3°), is measured. During the measurements, load (P) displacement (h) curves are recorded, and subsequently evaluated by Oliver and Pharr [82], schematically shown in Fig. 2.4.2. The hardness is calculated by the ratio between the applied load and the area of the residual indentation imprint. The Indentation Modulus can be derived from the slope of the initial unloading part of the load-displacement curve. For thin films, the penetration depth should not exceed 10 % of the coating thickness. Further on, the data have to be corrected by the area function for the indenter tip, as the tip used is never perfectly sharp. For arc evaporated coatings it is also useful to polish the samples prior hardness measurements, in order to minimize the influence of macroparticles on the substrate surface onto the revealed hardness values.

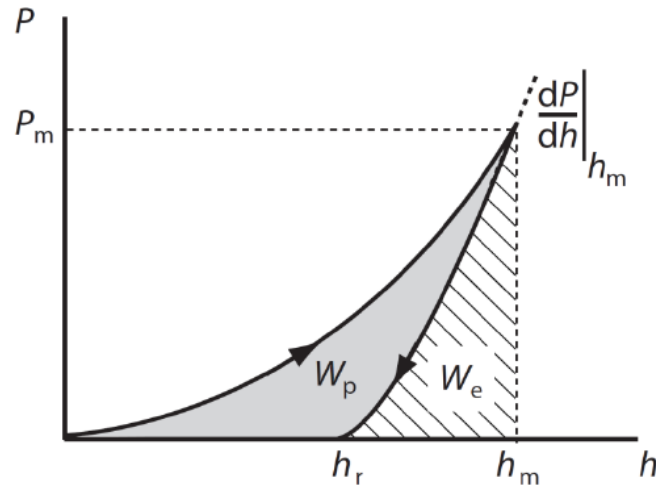


Fig. 2.4.2: Typical load-displacement curve from a nano-indentation measurement [83].

2.4.3 Thermal analyzes

2.4.3.1 DSC

Differential Scanning Calorimetry is widely used to characterize the thermal stability of materials and is based on the measurement of the heat flow from or to the sample and from or to a reference sample as a function of temperature and time. It enables the characterization of endothermic (melting or evaporation) and exothermic (crystallization or oxidation) heat changes during a user specified temperature program.

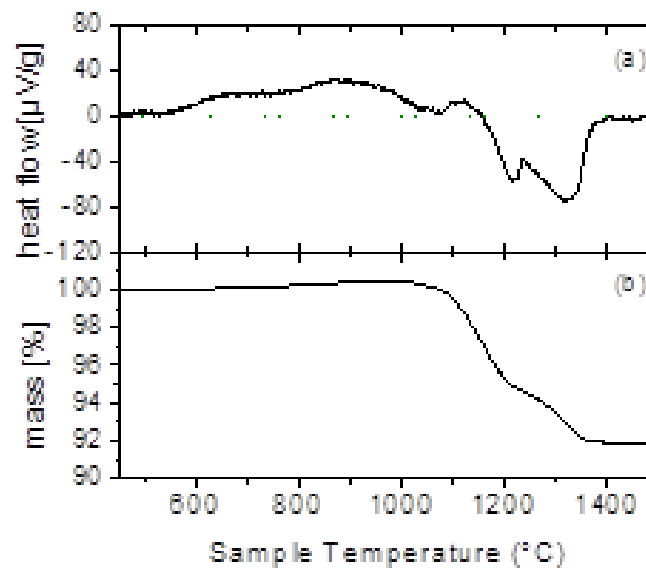


Fig. 2.4.3: Typical (a) DSC and (b) TGA signal for a $\text{Al}_x\text{Cr}_{1-x}\text{N}$ coating.

To obtain base-line corrected data, as shown in Fig. 2.4.3a for an $\text{Al}_{0.7}\text{Cr}_{0.3}\text{N}$ coating, the sample is measured two consecutive times.

The second run, which serves as a base line is then subtracted from the first run and consequently, irreversible reactions like recrystallization, recovery and decomposition processes which do not occur when the material is heated again, can be isolated. During the entire temperature program the sample mass can be measured by thermal gravimetric analysis (TGA), allowing for further information and interpretation of the data obtained, see Fig. 2.4.3b, [84].

Reactive and non-reactive sputter deposition of Al-Cr-N coatings using metallic, intermetallic, and ceramic targets

3.1 Introduction

Chromium nitride coatings are widely used in industry due to their excellent properties like high hardness, wear and oxidation resistance [6,39,85,86]. It is well known that the addition of Al, substituting Cr to form a ternary hard Al-Cr-N coating, is beneficial for these properties [6,50,85–88]. Recent studies indicated that by increasing the Al content, x of such $\text{Al}_x\text{Cr}_{1-x}\text{N}$ coatings up to ~ 0.75 , which corresponds to the solubility limit within the cubic (c) NaCl structure, the film properties can be enhanced significantly. Reiter et al. [50] showed that hardness values of around 38 GPa can be obtained for single-phase c-structured $\text{Al}_x\text{Cr}_{1-x}\text{N}$ coatings at $x = 0.7$. However, if this Al content is exceeded a dual phase cubic/wurtzite or even a single-phase wurtzite (w) structure is formed having decreased film properties [10,11,48]. Furthermore, great attention has been paid on the interrelationship between coating properties and deposition parameters. It has been shown that for example by increasing the kinetic energy during film growth (e.g., by increasing the bias voltage), a densification, smaller grain sizes, tailor made residual stress characteristics, a preferred crystallographic orientation, or even stabilization of the desired cubic structure can be obtained [13,14,33,89–94]. Nevertheless, there is only few information available on the influence of the target material itself on the microstructure of $\text{Al}_x\text{Cr}_{1-x}\text{N}$ coatings and hence, on the properties of such coatings. Mayrhofer et al. [37] have comparatively studied the effect of reactive and non-reactive sputter deposition of TiN coatings on the resulting film structure and performance. It has been shown that by using a ceramic TiN target material as cathode a higher deposition rate can be obtained compared to conventional reactive magnetron sputtering from a metallic Ti target, resulting in stoichiometric coatings with

extremely high hardness values, depending on the ion/atom flux ratio and the ion energy during deposition.

In general, powder metallurgically prepared targets, composed of metallic Al and Cr, are used to deposit $\text{Al}_x\text{Cr}_{1-x}\text{N}$ coatings. Within this study we used a metallic Al/Cr target, an intermetallic Al_8Cr_5 target, and a ceramic AlN/CrN_x target (all prepared by powder metallurgy) to prepare $\text{Al}_x\text{Cr}_{1-x}\text{N}$ coatings, in order to investigate their influence on the resulting coating structure and properties.

3.2 Experimental

All coatings were synthesized in a laboratory scaled unbalanced magnetron deposition plant (AJA Orion 5) using powder metallurgically produced metallic $\text{Al}_{0.7}\text{Cr}_{0.3}$, intermetallic Al_8Cr_5 , and ceramic $(\text{AlN})_{0.7}(\text{CrN})_{0.3}$ targets on sapphire ($10 \times 10 \times 0.53 \text{ mm}^3$) and Si ($7 \times 21 \times 0.35 \text{ mm}^3$) platelets as well as on copper foil. Prior to all depositions the substrates were ultrasonically cleaned in Acetone and Ethanol as well as thermally cleaned and Ar ion etched at a pressure of $3 \cdot 10^{-2}$ mbar (3 Pa). Reactive sputter deposition using the metallic, intermetallic and ceramic targets were carried out at a working gas pressure of $5 \cdot 10^{-3}$ mbar (0.5 Pa) in a mixed Ar/ N_2 glow discharge with an Ar to N_2 flow ratio of 1/1. Further, the ceramic target was also non-reactively (nr) sputtered in Ar atmosphere with a working gas pressure of $5 \cdot 10^{-3}$ mbar (0.5 Pa). For all depositions a constant temperature of 500 °C, a cathode power of $\sim 5.6 \text{ W/cm}^2$ as well as an rf-substrate bias of 5 W were used. Information on the film morphology as well as chemical compositions were obtained by a FEI Quanta 200 Field Emission Gun Scanning Electron Microscope (FEG-SEM) and by energy-dispersive X-ray spectroscopy (EDX, EDAX Pegasus XM4) using an acceleration voltage of 20 kV, respectively. X-ray diffraction (XRD) analyses were performed using a PANalytical X'pert Powder diffractometer, equipped with a $\text{CuK}\alpha$ radiation source, in the Bragg-Brentano mode. Evaluation of hardness (H) and modulus of indentation (E) were carried out by nanoindentation using a CSIRO ultra-micro indentation system equipped with a Berkovich tip. The indentations were conducted with normal loads ranging from 30 to 10 mN in steps of 0.5 mN and the indentation curves were analysed according to Oliver and Pharr [82] to obtain H and E . Differential scanning calorimetry (DSC) combined with thermal gravimetric

analysis (TGA) conducted in a SETSYS Evolution (Setaram instrumentation) calorimeter were used to investigate endothermic and exothermic reactions during high temperature annealing. The measurements were carried out in He atmosphere up to an annealing temperature (T_a) of 1500 °C with a heating rate of 20 K/min.

3.3 Results and Discussion

EDX analyses indicate that all reactively sputtered coatings, from the metallic, intermetallic, and ceramic targets, demonstrate a stoichiometric composition with Al contents of 0.73, 0.66, and 0.70, respectively. The slightly lower Al content of the coating sputtered from the intermetallic target material can be explained by the Al_8Cr_5 phase used to prepare the target material. This phase was chosen to prepare the intermetallic target as it exhibits a slightly extended stability range and should provide a coating composition comparable to the coatings prepared from the metallic and ceramic target. Depositing nr-Al-Cr-N from the ceramic target results in a chemical composition with a nitrogen/metal ratio of 0.64 and hence, an under-stoichiometric coating. Detailed investigations of the powder metallurgically prepared ceramic target material using XRD indicate w-AlN and face centred cubic (fcc) CrN phases see Fig. 3.3.1.

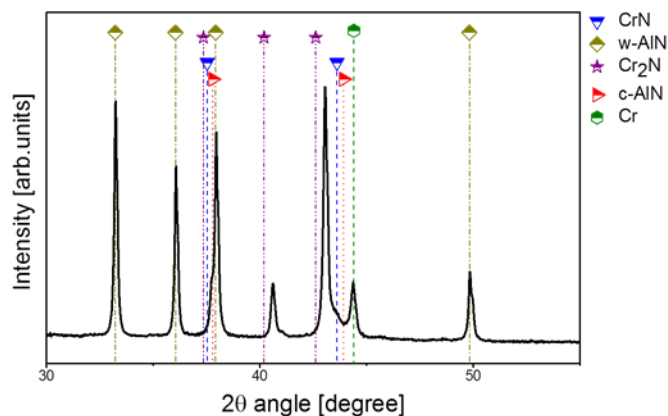


Fig. 3.3.1: XRD pattern of the ceramic AlN/CrN_x target.

However the XRD graph clearly exhibits also peaks of the hexagonal (h) Cr₂N as well as of the body centred cubic (bcc) Cr phase. This result suggests that during target processing,

the fcc-CrN powder is already decomposed into h-Cr₂N and bcc-Cr due to the higher temperatures used. Therefore, nr-deposition results also in the formation of under-stoichiometric Al-Cr-N coatings.

The fracture cross sections, shown in Figs. 3.3.2a-c indicate a columnar structure for all reactively sputtered coatings, independent of the target material used. The morphology of the nr-prepared Al-Cr-N film using the ceramic target is even denser, see Fig 2d. This change in morphology can be explained by increased growth kinetics during nr-sputtering of the ceramic target, as well as due to its composition. As mentioned afore, the ceramic target is composed of a mixture of fcc-CrN, h-Cr₂N and bcc-Cr phases which results in a slightly under-stoichiometric film during nr-deposition. As such an under-stoichiometric film is composed of hexagonal and cubic phases, continuous nucleation of different phases and their competition during growth results in the formation of an almost featureless fracture cross section [4,95]. The reactively sputtered coating thicknesses are 2.7, 4, and 3.7 μm when using the metallic, intermetallic, and ceramic target, respectively, and corresponds to deposition rates of ~ 11 , ~ 16.5 , and 15.3 nm/min , respectively. For the nr-sputtered coating even a thickness of $\sim 5.8 \mu\text{m}$, hence a deposition rate of 23.3 nm/min can be achieved, which is about two times higher as for reactively prepared coatings using the metallic target. These differences in the deposition rates might be related to the binding conditions in the target as well as to the poisoning effect during deposition. Our results are in good agreement with Mayrhofer et al. [37], who comparatively investigated reactive and nr-sputter deposited TiN indicating a three times higher deposition rate when using the ceramic targets compared to the metallic Ti target. It is stated that this effect can be related to the nitrogen target poisoning when using a gas mixture of Ar+N₂, which usually results in reduced sputter rates. Such a target poisoning also occurs during sputter deposition of Al_xCr_{1-x}N coatings and is most pronounced during sputtering of the metallic target material. Furthermore, a higher target voltage at constant power, due to a higher resistance in case of the intermetallic and ceramic target might result in an enhanced ion bombardment and hence higher sputter rates.

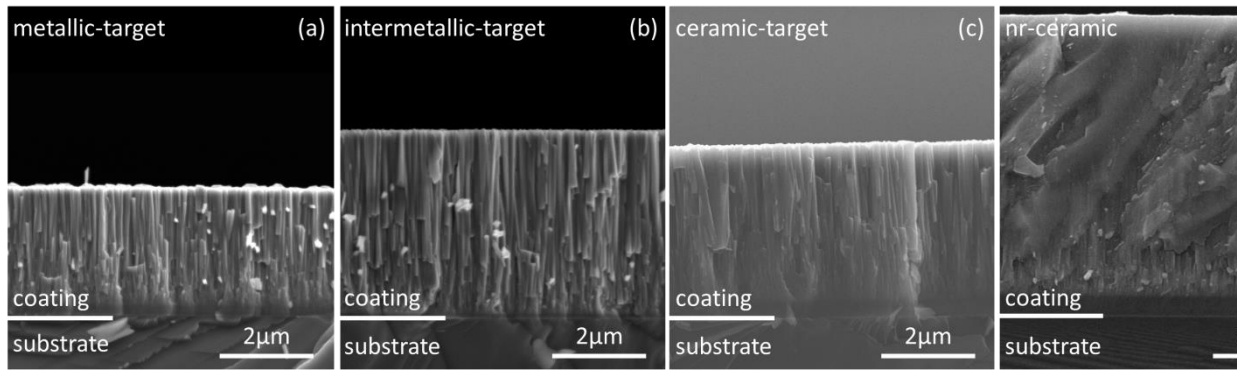


Fig. 3.3.2: SEM fracture cross sections of reactively sputtered coatings using the metallic, intermetallic, and ceramic target, (a) to (c), respectively, and of non-reactively sputtered coatings using the ceramic target (d).

XRD patterns, Fig. 3.3.3a, indicate a single-phase cubic structure for all coatings investigated. The reactively sputtered coatings clearly show a pronounced (111) orientation, whereas for the nr-sputtered Al-Cr-N coating a broad (200) oriented peak is revealed, suggesting a more nano-crystalline structure of these coatings. Petrov et al. [1,96] investigated the influence of changing growth kinetics on the resulting film configuration demonstrating that the preferential orientation of a film can be easily influenced by e.g. increasing the ion bombardment: by increasing the ion species or bias voltage during film deposition. It has also been shown that by increasing the growth kinetics, by e.g. increasing the number of metal ions in the plasma, the preferred orientation of CrN and TiN coatings can be changed from (111) to the stiffer (200) orientation [97,98]. Hence, the observed change in crystal orientation from reactive to nr-sputtering can be explained by changed growth kinetics. Furthermore, due to the competitive growth of the different phases when using nr-deposition the fcc-CrN phase is continuously re-nucleating resulting in smaller grain sizes, responsible for the broad XRD peaks.

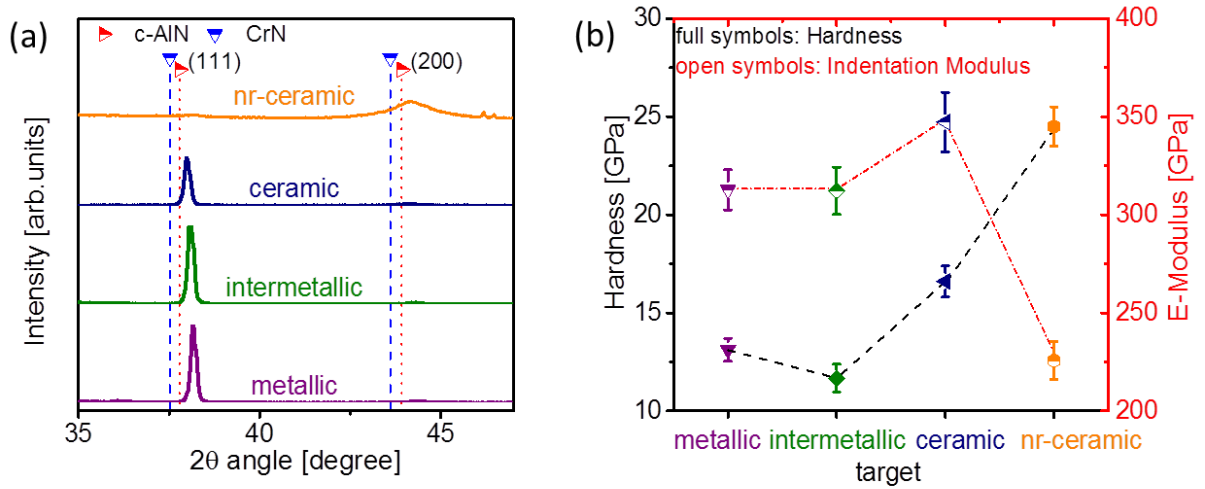


Fig. 3.3.3: XRD patterns of all coatings investigated in the as-deposited state (a) and the resulting hardness values and indentation modulus values obtained by nanoindentation (b).

Hardness values, given in Fig. 3.3.3b, are between ~13 and ~12 GPa for the reactively sputtered coatings using the metallic and intermetallic targets. These hardnesses are lower as literature reports for e.g. sputtered or arc evaporated $\text{Al}_{0.7}\text{Cr}_{0.3}\text{N}$ coatings, where peak values of about 38 GPa are obtained [7]. However, such arc evaporated $\text{Al}_x\text{Cr}_{1-x}\text{N}$ coatings exhibit fibrous-like dense morphology. We relate our lower hardness mainly to the not optimized deposition conditions, as our major goal was to compare the different target materials using identical deposition conditions. An increased hardness to around 16 GPa is obtained by using the ceramic target in the reactive sputter mode, due to an already denser morphology. When using the ceramic target in the nr-mode however, even hardness values of ~25 GPa can be obtained. The increased hardness of our nr-sputtered coatings is related to the fine crystalline structure and especially the dense morphology due to the various phases competing during film growth. Evaluation of the indentation modulus E , Fig. 3.3.3b, indicates for the reactively sputtered coatings a similar behaviour like the hardness values. However, when changing to nr-sputtering the E -modulus decreases drastically from around 350 GPa (reactively) to around 225 GPa (nr). This can be related to the under-stoichiometric film composition and the appearance of additional phase fractions which are responsible for the almost x-ray amorphous structure of this coating, see Fig. 3.3.3a.

In Fig. 3.3.4, the DSC signals and the mass loss as a function of the annealing temperature for the reactively and nr-sputtered coatings are shown. All spectra consist of several

exothermic and endothermic features. Detailed XRD investigations (not shown here) showed that the first exothermic reactions up to a temperature of ~ 900 °C can be attributed to recovery and relaxation processes, due to increased diffusivity at elevated temperatures. This is followed by exothermic reactions ranging up to ~ 1100 °C due to nucleation and growth processes of the w-AlN phase, which is superimposed by a strong endothermic reaction which can be related to the instability of Cr-N bonds, and hence its decomposition (dissociation into Cr and N) [42,49]. Consequently, nitrogen release is initiated, which is indicated by an increased mass-loss as detected by TGA at temperatures above 1000 °C. The first change in the slope of the TGA curve at ~ 1000 °C corresponds to the transformation of CrN into Cr_2N under release of N_2 , and the second change at ~ 1200 °C corresponds to the transformation of Cr_2N into Cr. For T_a above ~ 1350 °C no further exothermic or endothermic reactions are detected suggesting a completed dissociation of our coating. The peak temperatures for the first endothermic reaction, related to the instability of the Cr-N bonds are at around 1070, 1100, and 1130 °C for the stoichiometric $\text{Al}_x\text{Cr}_{1-x}\text{N}$ coatings deposited reactively from the intermetallic, metallic, and ceramic target, respectively. Consequently, an increase in thermal stability of around 60 °C is obtained when using a ceramic target to prepare $\text{Al}_x\text{Cr}_{1-x}$ coatings.

The total mass loss for the reactively sputtered coatings is mainly influenced by the decomposition of Cr-N rather than by N_2 -release from AlN. Hence, a higher Al content results in a higher amount of stable Al-N bonds and consequently, less nitrogen loss due to Cr-N dissociation. As our reactively sputtered coatings from the metallic, ceramic, and intermetallic target exhibit an Al content of 0.73, 0.70, and 0.67, respectively, the total mass loss is highest using the intermetallic target and lowest when using the metallic one. For the nr-sputtered coating the first exothermic reaction is more pronounced as for the reactively sputtered coatings, which can be related to crystallization and grain growth. This supports together with the low E -Modulus (compare Fig. 3.3.3b) the XRD indicated nano-crystalline structure. The lower mass loss compared to the reactively sputtered coatings is related to the lower nitrogen content within the coating already in the as deposited state. Furthermore, the dissociation is shifted to higher temperatures. Nevertheless, XRD after DSC to 1500 °C indicates that also for the nr-sputtered coating the decomposition and dissociation towards the stable bcc-Cr and w-AlN phases is completed.

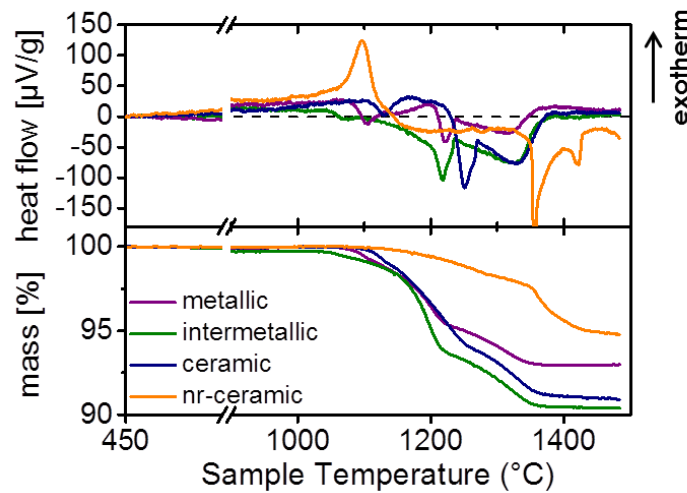


Fig. 3.3.4: DSC and TGA signals for the reactively as well as the non-reactively sputtered Al-Cr-N coatings.

3.4 Summary and Conclusion

$\text{Al}_x\text{Cr}_{1-x}\text{N}$ coatings were reactively sputtered using a dc glow discharge in an Ar-N_2 atmosphere (flow rate ratio of 1) from powder metallurgically prepared metallic $\text{Al}_{0.7}\text{Cr}_{0.3}$, intermetallic Al_8Cr_5 , and ceramic AlN/CrN_x targets. The ceramic target was also subject to non-reactive sputtering in Ar atmosphere. For the reactively sputtered coatings a pronounced (111) oriented, columnar structure is obtained. Here, using a ceramic target results in a denser, fine fibrous coating morphology as compared to the coatings prepared from the other targets. When using the intermetallic and ceramic target the deposition rate is ~50% and ~40% higher as compared to the metallic target. However, for the nr-sputtered coating using the ceramic target the deposition rate is even 100% higher and the resulting coating morphology is extremely dense with a nearly featureless fracture cross section. Also XRD investigations suggest for this coating an extremely nano-crystalline nature, most likely due to the competition of several phases during nucleation and growth, although only a low-intensity and very broad peak at the (200) orientation of the $\text{Al}_x\text{Cr}_{1-x}\text{N}$ phase can be detected. This is due to the under-stoichiometric nature of the AlN/CrN_x ceramic target. Based on the different morphology also the hardness of the coatings is different. The pronounced columnar coatings, reactively sputtered from the metallic and intermetallic targets, exhibit hardness values of ~12 and 13 GPa. The coatings prepared reactively and

non-reactively from the ceramic target are denser in morphology and therefore also harder with ~ 16.5 and even 25 GPa, respectively. Thermal analyses of the $\text{Al}_x\text{Cr}_{1-x}\text{N}$ coatings in inert atmosphere up to 1500 °C clearly show that the endothermic reactions due to Cr-N dissociations (from CrN to Cr_2N and further to Cr under N_2 -release) are shifted to higher temperatures when using the ceramic target. Based on our results we can conclude that varying the target design for a given chemical composition leads to further improved coatings (e.g., denser morphology, higher hardness) and deposition (e.g., higher deposition rate).

CHAPTER 4

Influence of bias potential and layer arrangement on structure and mechanical properties of arc evaporated Al-Cr-N coatings

4.1 Introduction

Chromium nitride coatings are widely used as protective coatings due to their high hardness, wear and oxidation resistance [46,99,100]. It is well known that in order to further improve these properties Al is alloyed, substituting for Cr to form a ternary $\text{Al}_x\text{Cr}_{1-x}\text{N}$ hard coating [40,46,50,66,99,100]. The structure and properties of such $\text{Al}_x\text{Cr}_{1-x}\text{N}$ coatings are closely related to their AlN content x [10,11,50,94]. Reiter et al. [51,101] showed that arc evaporated $\text{Al}_x\text{Cr}_{1-x}\text{N}$ coatings can be prepared in a single phase cubic (c) structure up to $x = 0.7$, exhibiting hardness values of around 38000 N/mm^2 (38 GPa), which are stable up to annealing temperatures of 900°C . Exceeding this critical AlN content will result in the formation of a dual phase structure, cubic and hexagonal (wurtzite-type, w) phases, or even in a single phase w-structure, with generally decreased mechanical properties and coating performance. Consequently, it is important to remain within the single phase cubic structure while increasing the Al content, as this is beneficial for increased bonding strength [48] and oxidation resistance. The latter is based on the formation of dense $\text{Cr}_2\text{O}_3\text{-Al}_2\text{O}_3$ outer layers, which protect the nitride coating underneath against further oxidation [51,66]. Various studies show that by multilayer architectures the film properties can be improved [18,60,61,102]. Due to the layered structure of e.g. CrN/AlN multilayer coatings, additional interfaces are formed resulting in variations of the stress/strain field and interference with dislocation mobility, and hence increased mechanical properties compared to monolithically grown coatings. It has also been shown for the CrN/AlN multilayer system, that AlN layers can be stabilized in their metastable cubic structure by coherent growth on the cubic CrN layers [19,20,61,65]. Additionally, by varying the bias voltage applied to the substrate materials, the growth morphology (e.g. density, grain sizes, crystallographic

orientation, defect density and hence residual stresses) and even structure of the coatings can be modified [13,14,91,92,94,103,104].

In this work, we present cathodic arc evaporated $\text{Al}_x\text{Cr}_{1-x}\text{N}$ coatings with different multilayer architecture combining lower Al-containing $\text{Al}_{0.7}\text{Cr}_{0.3}\text{N}$ and $\text{Al}_{0.75}\text{Cr}_{0.25}\text{N}$ layers with higher Al-containing $\text{Al}_{0.85}\text{Cr}_{0.15}\text{N}$ and $\text{Al}_{0.9}\text{Cr}_{0.1}\text{N}$ layers, respectively. These multilayer coatings are compared with their monolithically grown counterparts.

4.2 Experimental

All depositions were carried out in a Balzers INNOVA industrial scaled deposition plant using powder metallurgically prepared $\text{Al}_{0.7}\text{Cr}_{0.3}$, $\text{Al}_{0.75}\text{Cr}_{0.25}$, $\text{Al}_{0.85}\text{Cr}_{0.15}$, and $\text{Al}_{0.9}\text{Cr}_{0.1}$ targets (Plansee SE) having Al contents of 70, 75, 85, and 90 at%, respectively. The substrates were mounted on a two-fold rotating carousel with a minimum target to substrate distance of ~25 cm. The multilayer architecture can easily be realized by rotating the carousel in-between the four cathodes equipped with targets of different compositions (e.g. two $\text{Al}_{0.7}\text{Cr}_{0.3}$ next to two $\text{Al}_{0.85}\text{Cr}_{0.15}$ targets, abbreviated with $\text{Al}_{0.7}\text{Cr}_{0.3}/\text{Al}_{0.85}\text{Cr}_{0.15}$). Prior to the depositions, the substrates used were ultrasonically cleaned in acetone and ethanol, as well as thermally cleaned for 30 min at 500 °C and Ar ion etched within the chamber. The temperature during deposition was kept constant at 500 °C and the nitrogen partial pressure was adjusted to 3.5 Pa. Bias potential (U_b) variations ranging from -40 to -120 V were used for the monolithically grown coatings and their multilayered architectures. The resulting coating thickness was determined by the ball-crater technique. The surface roughness of our coatings was evaluated by profilometry using a Nanovea PS50 chromatographic white-light profilometer. Information on the film morphology as well as chemical compositions were revealed by a ZEISS EVO 50 scanning electron microscope (SEM) and by energy-dispersive X-ray spectroscopy (EDX, Oxford Instruments INCA), respectively, using an acceleration voltage of 20 keV. Quantification is obtained by means of four $\text{Al}_x\text{Cr}_{1-x}\text{N}_y$ thin film standards ($\text{Al}_{0.72}\text{Cr}_{0.28}\text{N}_{1.0}$, $\text{Al}_{0.74}\text{Cr}_{0.26}\text{N}_{0.5}$, $\text{Al}_{0.78}\text{Cr}_{0.24}\text{N}_{0.98}$, and $\text{Al}_{0.80}\text{Cr}_{0.22}\text{N}_{0.98}$), calibrated by elastic recoil detection analyses using Cl^{7+} ions with an acceleration voltage of 43 MeV. X-ray diffraction (XRD) analyses were performed using a Siemens D500 diffractometer, equipped with a $\text{CuK}\alpha$ radiation source, in the grazing

incidence configuration with an angle of incident of 2°. Hardness (H) and modulus of indentation (E) were determined using a CSIRO ultra micro indentation system equipped with a Berkovich indenter. The indentations were conducted with normal loads ranging from 30 to 10 mN in steps of 0.5 mN and the results were calculated from the loading and unloading segments according to Oliver and Pharr [82].

4.3 Results and Discussion

The nitrogen content of all coatings deposited is between 49 and 50 at%, hence we use a nomenclature for our coatings corresponding to stoichiometric nitrides. The chemical compositions of the monolithically prepared nitride coatings correspond to $\text{Al}_{0.68}\text{Cr}_{0.32}\text{N}$, $\text{Al}_{0.70}\text{Cr}_{0.3}\text{N}$, $\text{Al}_{0.82}\text{Cr}_{0.18}\text{N}$, and $\text{Al}_{0.89}\text{Cr}_{0.11}\text{N}$. Consequently, they contain slightly lower Al-contents as their respective targets $\text{Al}_{0.7}\text{Cr}_{0.3}$, $\text{Al}_{0.75}\text{Cr}_{0.25}$, $\text{Al}_{0.85}\text{Cr}_{0.15}$, and $\text{Al}_{0.9}\text{Cr}_{0.1}$, being in agreement with previous reports about arc evaporated $\text{Al}_x\text{Cr}_{1-x}\text{N}$ coatings when using composite $\text{Al}_x\text{Cr}_{1-x}$ targets [50,53]. The overall compositions of the multilayered coatings correspond to $\text{Al}_{0.75}\text{Cr}_{0.25}\text{N}$, $\text{Al}_{0.78}\text{Cr}_{0.22}\text{N}$, $\text{Al}_{0.77}\text{Cr}_{0.15}\text{N}$, and $\text{Al}_{0.79}\text{Cr}_{0.21}\text{N}$ when using $\text{Al}_{0.7}\text{Cr}_{0.3}/\text{Al}_{0.85}\text{Cr}_{0.15}$, $\text{Al}_{0.7}\text{Cr}_{0.3}/\text{Al}_{0.9}\text{Cr}_{0.1}$, $\text{Al}_{0.75}\text{Cr}_{0.25}/\text{Al}_{0.85}\text{Cr}_{0.15}$, and $\text{Al}_{0.75}\text{Cr}_{0.25}/\text{Al}_{0.9}\text{Cr}_{0.1}$ target combinations, respectively. For easier reading and a clear correlation to the used targets we will use the target composition when referring to the coatings. Hence, $\text{Al}_{0.7}\text{Cr}_{0.3}\text{N}$, $\text{Al}_{0.75}\text{Cr}_{0.25}\text{N}$, $\text{Al}_{0.85}\text{Cr}_{0.15}\text{N}$, and $\text{Al}_{0.9}\text{Cr}_{0.1}\text{N}$ indicate the monolithically grown coatings and $\text{Al}_{0.7}\text{Cr}_{0.3}\text{N}/\text{Al}_{0.85}\text{Cr}_{0.15}\text{N}$, $\text{Al}_{0.7}\text{Cr}_{0.3}\text{N}/\text{Al}_{0.9}\text{Cr}_{0.1}\text{N}$, $\text{Al}_{0.75}\text{Cr}_{0.25}/\text{Al}_{0.85}\text{Cr}_{0.15}$, and $\text{Al}_{0.75}\text{Cr}_{0.25}/\text{Al}_{0.9}\text{Cr}_{0.1}$ indicate their multilayered arrangements. As the growth morphology is similar of all coatings, fracture cross sections of the $\text{Al}_{0.7}\text{Cr}_{0.3}\text{N}/\text{Al}_{0.85}\text{Cr}_{0.15}\text{N}$ multilayer coatings, at bias potentials ranging from -40 to -120V, Figs. 4.3.1a to d, are shown representatively, indicating a very dense structure, as expected for cathodic arc evaporated coatings. Further on, macro-particles can be observed at the film surface, resulting in a roughness R_a of our coatings at around 80-180 nm, depending on the Al content and the bias voltage applied. Here, increasing the bias potential (from -40 V to -120 V) and decreasing the Al content (e.g. for the monolithically grown coatings from 0.89 to 0.68) results in increased roughness values.

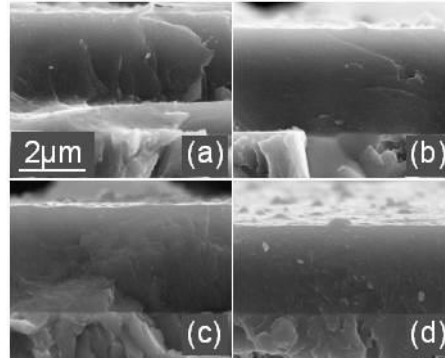


Fig. 4.3.1: SEM fracture cross sections of the $\text{Al}_{0.7}\text{Cr}_{0.3}\text{N}/\text{Al}_{0.85}\text{Cr}_{0.15}\text{N}$ multilayer coatings, grown with bias potentials of (a) -40V, (b) -80V, (c) -100V, and (d) -120V.

The growth rates of the monolithically grown coatings and the calculated bilayer period Λ of the multilayer coatings decrease with increasing bias voltage, Figs. 4.3.2a and b, respectively.

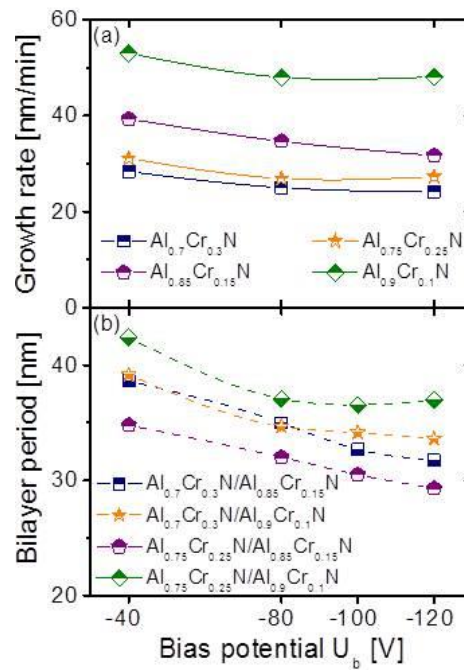


Fig. 4.3.2: (a) Growth rate of monolithically prepared coatings and (b) bilayer period of the multilayered coatings as a function of the applied bias potential.

This is mainly caused by re-sputtering effects and film densification. Further on, it can be seen that the wurtzite structured films demonstrate a factor of two higher growth rates as compared to the cubic coatings which can be related to the difference in the specific volume of cubic and wurtzite phases (see next paragraph). Therefore, the reduction of

deposition rate within our multilayer coatings is even more pronounced, as not only the film morphology changes but also the phase structure changes from pre-dominant wurtzite to mainly cubic. The XRD patterns of the monolithically grown $\text{Al}_{0.7}\text{Cr}_{0.3}\text{N}$ and $\text{Al}_{0.75}\text{Cr}_{0.25}\text{N}$ coatings indicate a single phase cubic structure independent of the bias voltage used, Figs. 4.3.3a and b, respectively. However, increasing the bias voltage from -40 to -80 V, results in a peak shift to lower 2θ diffraction angles, which can be attributed to an increased residual stresses, as shown by Wang et al. [105]. A slight peak-shift backwards to higher 2θ angles can be

observed when further increasing the bias voltage to -120 V, suggesting a decrease in compressive stresses driven by increased ad-atom mobility during increased ion bombardment. Hence, above a critical threshold of the bias potential, defect annihilation – due to increased kinetics – compensates or even overcompensates the defect generation [106]. Furthermore, the enhanced ion bombardment results in re-sputtering effects on the coating surface changing the Al to Cr ratio to lower Al values, which also results in a slight peak shift to lower 2θ diffraction angles.

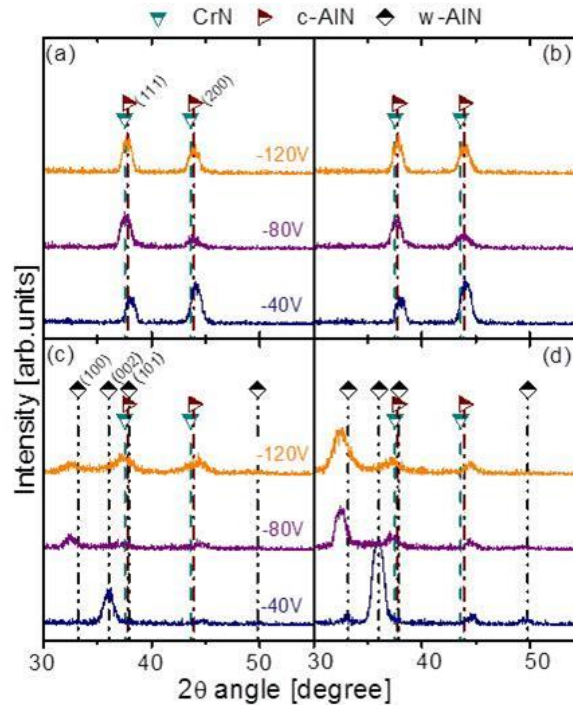


Fig. 4.3.3: GIXRD patterns of the monolithically grown coatings using (a) $\text{Al}_{0.7}\text{Cr}_{0.3}$, (b) $\text{Al}_{0.75}\text{Cr}_{0.25}$, (c) $\text{Al}_{0.85}\text{Cr}_{0.15}$, and (d) $\text{Al}_{0.9}\text{Cr}_{0.1}$ targets and various bias potentials.

The $\text{Al}_{0.85}\text{Cr}_{0.15}\text{N}$ and $\text{Al}_{0.9}\text{Cr}_{0.1}\text{N}$ coatings, Figs. 4.3.2(c) and (d) exhibit the expected (based on *ab initio* studies [48]) wurtzite structure, especially for low bias potentials. However, increasing the bias potential during deposition promotes the development of cubic structured regions resulting in a dual-phase mixed cubic-wurtzite structure. Mayrhofer et al. [48] showed that by changing the configurational entropy of $\text{Al}_x\text{Cr}_{1-x}\text{N}$ the maximum solubility of Al within the cubic structure can be varied between ~ 0.5 and 0.76 . Increasing the bias potential changes the configurational entropy of any crystal, which could explain the change from single phase wurtzite to a dual-phase mixed cubic-wurtzite structure. Furthermore, increased ion bombardment – thus increased compressive stresses – additionally promotes the growth of the denser packed cubic phases against the hexagonal wurtzite phase. Wurtzite structured AlN exhibits a $\sim 26\%$ larger specific volume as its cubic counterpart [107].

The multilayer coatings, $\text{Al}_{0.7}\text{Cr}_{0.3}\text{N}/\text{Al}_{0.85}\text{Cr}_{0.15}\text{N}$, $\text{Al}_{0.7}\text{Cr}_{0.3}\text{N}/\text{Al}_{0.9}\text{Cr}_{0.1}\text{N}$, $\text{Al}_{0.75}\text{Cr}_{0.25}\text{N}/\text{Al}_{0.85}\text{Cr}_{0.15}\text{N}$, and $\text{Al}_{0.75}\text{Cr}_{0.25}\text{N}/\text{Al}_{0.9}\text{Cr}_{0.1}\text{N}$, demonstrate a pronounced wurtzite structure at a low bias potential of -40 V, independent from the layer arrangement used, Figs. 4.3.4a, b, c, and d, respectively. A change from wurtzite to an overall cubic structure with increasing bias potential can be observed for the $\text{Al}_{0.7}\text{Cr}_{0.3}\text{N}/\text{Al}_{0.85}\text{Cr}_{0.15}\text{N}$ and $\text{Al}_{0.75}\text{Cr}_{0.25}\text{N}/\text{Al}_{0.85}\text{Cr}_{0.15}\text{N}$ multilayers, Figs. 4.3.4a and c, respectively. Such a transformation towards the cubic phase can be attributed to the densification of the film and the thereby suppressed growth of the less dense hexagonal phase as well as to the increased maximum solubility of Al in this ternary system due to the enhanced ion bombardment, as mentioned before [33,94,96]. Coherency strains to their c- $\text{Al}_{0.7}\text{Cr}_{0.3}\text{N}$ and c- $\text{Al}_{0.75}\text{Cr}_{0.25}\text{N}$ layers additionally support the crystallization of the higher Al-containing $\text{Al}_{0.85}\text{Cr}_{0.15}\text{N}$ layers in their cubic structure, respectively, leading to an overall cubic structure of these multilayers. This is in agreement to reports about CrN/AlN and TiN/AlN multilayer coatings, where the AlN layers are stabilized in their metastable cubic structure due to coherency strains to the cubic CrN and TiN layers [20,65]. However, the multilayer arrangements with the highest Al-containing layers $\text{Al}_{0.7}\text{Cr}_{0.3}\text{N}/\text{Al}_{0.9}\text{Cr}_{0.1}\text{N}$ and $\text{Al}_{0.75}\text{Cr}_{0.25}\text{N}/\text{Al}_{0.9}\text{Cr}_{0.1}\text{N}$ can not be stabilized fully in their cubic structure even for the highest bias potential used of -120 V.

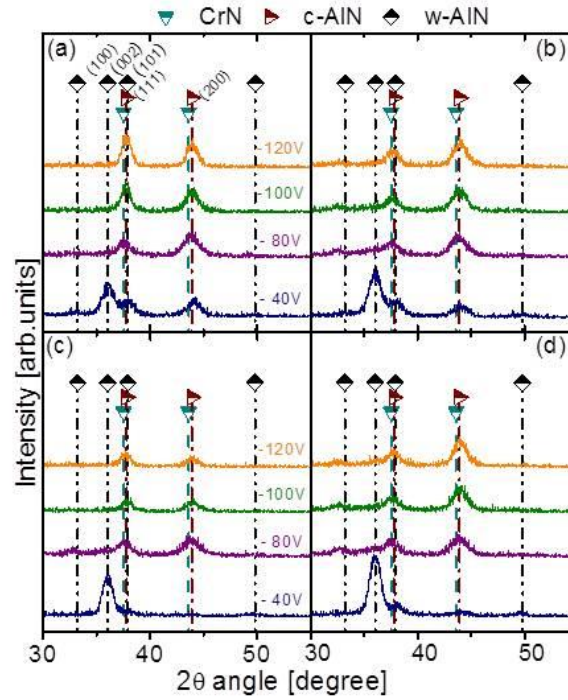


Fig. 4.3.4: GIXRD patterns of multilayered coatings prepared with (a) $\text{Al}_{0.7}\text{Cr}_{0.3}/\text{Al}_{0.85}\text{Cr}_{0.15}$, (b) $\text{Al}_{0.7}\text{Cr}_{0.3}/\text{Al}_{0.9}\text{Cr}_{0.1}$, (c) $\text{Al}_{0.75}\text{Cr}_{0.25}/\text{Al}_{0.85}\text{Cr}_{0.15}$, and (d) $\text{Al}_{0.75}\text{Cr}_{0.25}/\text{Al}_{0.9}\text{Cr}_{0.1}$ target-combinations and various bias potentials.

Our monolithically grown $\text{Al}_{0.7}\text{Cr}_{0.3}\text{N}$ and $\text{Al}_{0.75}\text{Cr}_{0.25}\text{N}$ coatings have high hardnesses of around 32 GPa when using a bias potential of -40 V and around 38 GPa, when increasing the potential to -80 and -120 V, see Fig. 4.3.5a. Increasing growth density in addition to increased residual stresses with increasing ion bombardment is responsible for this hardness increase [33,96]. The overall wurtzite structured monolithically grown coatings $\text{Al}_{0.85}\text{Cr}_{0.15}\text{N}$ and $\text{Al}_{0.9}\text{Cr}_{0.1}\text{N}$, when applying only a low bias potential U_b of -40 V, exhibit only low hardnesses around 17 and 19 GPa, respectively. However, the hardness can significantly be increased to around 28 GPa, when the applied bias potential is increased up to -120 V. This hardness increase is basically based on the concomitant increased cubic phase fraction, as highlighted by the XRD measurements, Figs. 4.3.3c and d. This is in excellent agreement with previous studies, indicating enhanced mechanical properties when stabilizing the Al-Cr-N coatings in their cubic structure [50,87].

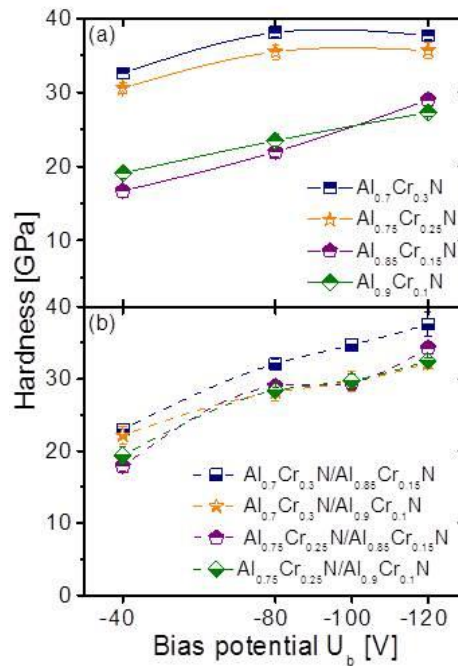


Fig. 4.3.5: (a) Hardness of monolithically grown coatings and (b) multilayer coatings for different bias potentials applied.

The hardness of our multilayerd coatings demonstrate a comparable behavior, as only low hardnesses between 18 and 23 GPa, see Fig. 4.3.5b, are obtained for low bias potentials of -40 V due to their predominant wurtzite structure, see Fig. 4.3.4. However, with increasing bias potential their structure changes to predominant cubic, leading to a pronounced increase in hardness up to 37 GPa. Here, especially the $\text{Al}_{0.7}\text{Cr}_{0.3}\text{N}/\text{Al}_{0.85}\text{Cr}_{0.15}\text{N}$ multilayers, exhibiting a fully cubic stabilized structure for $U_b \geq -100$ V provide hardnesses of 35 GPa and 37 GPa at U_b of -100 and -120 V, respectively.

4.4 Summary and Conclusion

Monolithically grown nitride coatings using $\text{Al}_{0.7}\text{Cr}_{0.3}$ and $\text{Al}_{0.75}\text{Cr}_{0.25}$ targets reveal a single phase cubic structure and increasing hardness from 33 to 38 GPa or 31 to 36 GPa, respectively, with increasing bias potential from -40 to -80 V. Using higher Al containing $\text{Al}_{0.85}\text{Cr}_{0.15}$ and $\text{Al}_{0.9}\text{Cr}_{0.1}$ targets leads to the formation of either single phase wurtzite ($U_b = -40$ V) or mixed-phase cubic-wurtzite ($U_b \geq -80$ V) structured coatings, exhibiting only moderate hardnesses of around 19 or 27 GPa, respectively. Contrary, combining the lower Al-containing $\text{Al}_{0.7}\text{Cr}_{0.3}\text{N}$ and $\text{Al}_{0.75}\text{Cr}_{0.25}\text{N}$ layers with higher Al-containing $\text{Al}_{0.85}\text{Cr}_{0.15}\text{N}$ layers

leads to predominant cubic structured coatings for bias potentials $U_b \geq -100$ V. This is related to the combined effect of coherency strains and suppressed growth of the less dense hexagonal phase at intense ion bombardment. The hardness of these multilayered coatings can thus be increased to 33 and 37 GPa, respectively. Consequently, the study clearly shows that by using cubic structured $\text{Al}_{0.7}\text{Cr}_{0.3}\text{N}$ and $\text{Al}_{0.75}\text{Cr}_{0.25}\text{N}$ layers also higher Al-containing layers such as $\text{Al}_{0.85}\text{Cr}_{0.15}\text{N}$ can be stabilized in their metastable cubic structure when preparing multilayers with bilayer periods of around 30 nm.

CHAPTER 5

Impact of bias potential and layer arrangement on the thermal stability of arc evaporated Al-Cr-N coatings

5.1 Introduction

Chromium nitride coatings are well known for their high hardness, wear and oxidation resistance [40,46,99]. However, these properties can further be improved by the addition of Al substituting for Cr to form a ternary hard $\text{Al}_x\text{Cr}_{1-x}\text{N}$ coating [40,48,50,66,99]. In general, the structure and thus the properties of such coatings are linked with their Al content x . Various studies indicate that by increasing x up to ~ 0.75 , which corresponds to the *ab initio* suggested solubility limit within the cubic (c) NaCl structure, the film properties can be enhanced significantly. Exceeding this Al content leads to the formation of a mixed structure composed of cubic and hexagonal (ZnS wurtzite type, w) phases or even to a single phased wurtzite type structure. Based on the increased mechanical properties, the cubic structure is generally preferred over their wurtzite type counterpart [10,11,48]. Reiter et al. [50] showed that $\text{Al}_x\text{Cr}_{1-x}\text{N}$ coatings, synthesized by cathodic arc evaporation, can be stabilized in the cubic structure up to Al contents of 0.7. With increasing Al content, the thermal stability – especially with respect to N_2 release due to breaking of the Cr–N bonds – and the oxidation resistance increases [49,53,67,108]. The latter is based on the formation of dense and thermally stable Cr_2O_3 - Al_2O_3 oxide scales [51,66]. However, also here it is important to provide a single phased structure of the coatings [49,53,67,108].

In addition to optimizing coatings by their chemical composition, their architecture (e.g., multilayer or even superlattice arrangements, graded composition, and defect or stress design by applying alternating bias potentials [18,56–60,62]) is of utmost importance. For example, the additional interfaces and shear moduli variations of multilayered or superlattice CrN/AlN coatings are the origin of their increased mechanical properties as

compared with monolithically grown coatings of comparable overall chemical composition. Furthermore, coherency strains between alternating CrN and AlN layers allow for stabilizing layers in their metastable cubic structure up to thicknesses of ~3 nm [19,20,61,64,65]. Even though, many properties can be increased by a layered architecture of cubic structured CrN/AlN superlattice coatings, their thermal stability is often reduced compared with their monolithically grown supersaturated $\text{Al}_x\text{Cr}_{1-x}\text{N}$ counterparts [49,67,109]. This is based on the additional interfaces provided and the phase-pure AlN and CrN layers. Aluminum, within single phased $\text{Al}_x\text{Cr}_{1-x}\text{N}$ materials, is responsible for strengthening of the bindings, retarding CrN dissociation towards Cr_2N and nitrogen [49][108]. Furthermore, chromium within $\text{Al}_x\text{Cr}_{1-x}\text{N}$ materials is responsible for their cubic structure stabilization [48,110]. In addition to these modifications of coatings, also variations of the deposition parameters, like increasing the bias potential, will cause changes in the coating properties. By optimizing the deposition conditions, the density, grain size, stress characteristics, preferred crystallographic orientation, or even the crystallization of desired structures can be specifically adjusted and designed [25–33].

Here we investigate the influence of bias potential as well as multilayer arrangement on thermal stability of arc evaporated $\text{Al}_x\text{Cr}_{1-x}\text{N}$ coatings and compare these with homogeneously grown counterparts. The thermal stability is characterized with the help of differential scanning calorimetric measurements, X-ray diffraction and hardness investigations after annealing the samples up to 1300 °C in vacuum.

5.2 Experimental Details

All coatings investigated were synthesized using an industrial scale Balzers INNOVA deposition plant equipped with powder metallurgically produced $\text{Al}_{0.7}\text{Cr}_{0.3}$, $\text{Al}_{0.75}\text{Cr}_{0.25}$, $\text{Al}_{0.85}\text{Cr}_{0.15}$, and $\text{Al}_{0.9}\text{Cr}_{0.1}$ targets (Plansee SE). The substrates (low iron steel foil and sapphire) were mounted on a two-fold rotating carousel, having a minimum distance to the targets of ~25 cm. The multilayered coatings were prepared by equipping two out of the four cathodes used with chemically different targets. We have used the combinations $\text{Al}_{0.7}\text{Cr}_{0.3}/\text{Al}_{0.85}\text{Cr}_{0.15}$, $\text{Al}_{0.7}\text{Cr}_{0.3}/\text{Al}_{0.9}\text{Cr}_{0.1}$, $\text{Al}_{0.75}\text{Cr}_{0.25}/\text{Al}_{0.85}\text{Cr}_{0.15}$, and $\text{Al}_{0.75}\text{Cr}_{0.25}/\text{Al}_{0.9}\text{Cr}_{0.1}$ to prepare four different sets of multilayers. An additional variation of the samples is obtained

by preparing them with -40 V, -80 V, and -120 V bias potentials. For all compositions, a constant temperature of 500 °C and a constant nitrogen partial pressure of 3.5 Pa were used. In addition to ultrasonically cleaning of the substrates in acetone and ethanol, a heating step within the evacuated deposition chamber followed by an Ar ion etching step were implemented prior to the deposition process. This allows removing residuals and oxides from the substrate surfaces. The microstructure and bilayer period was studied using a Phillips CM12 transmission electron microscope (TEM) operated with 120 kV and by energy-dispersive X-ray spectroscopy (EDX, EDAX AMETEK). X-ray diffraction (XRD) analyses were performed using a Bruker-AXS D8 Advanced diffractometer, equipped with a CuK α radiation source, in the Bragg-Brentano mode. The thermal stability of the Al $_x$ Cr $_1-x$ N coatings was investigated by differential scanning calorimetry (DSC) measurements combined with thermo gravimetric analysis (TGA) in a SETSYS Evolution (Setaram instrumentation) calorimeter. The dynamical measurements were carried out with a heating rate of 20 K/min up to 1500 °C in flowing He.

Free standing coating powder (gently grinding the coatings in a porcelain mortar, after chemically removing the used low alloyed steel foil substrate with 10 mol% nitric acid) was annealed in a vacuum furnace (HTM Reetz GmbH, base pressure < 5 x 10⁻⁴ at temperatures T_a ranging from 600 to 1300 °C in steps of 100 °C using a heating rate of 30 K/min, a holding time of 1h, and a cooling rate of 60 K/min. Subsequent to these annealing treatments the coating are again investigated by XRD at room temperature.

The hardness H of our coatings on sapphire substrates in their as deposited state and after annealing at T_a = 600, 700, 800, 900, 1000, 1100 °C for 1 h in vacuum was measured by nanoindentation using a CSIRO ultra-micro indentation system equipped with a Berkovich tip. The indentations were conducted with normal loads ranging from 30 to 10 mN in steps of 0.5 mN and the indentation curves were analyzed according to Oliver and Pharr [28] to obtain H.

5.3 Results and Discussion

5.3.1 As deposited structure and morphology

XRD diffraction patterns, Fig. 5.3.1, of powdered as deposited coating material prepared using four identical $\text{Al}_{0.7}\text{Cr}_{0.3}$ targets, indicate a single phase cubic structure independent of the bias potential applied. On the other hand all multilayers prepared (using the cathode combinations $\text{Al}_{0.7}\text{Cr}_{0.3}\text{N}/\text{Al}_{0.85}\text{Cr}_{0.15}\text{N}$, $\text{Al}_{0.7}\text{Cr}_{0.3}\text{N}/\text{Al}_{0.9}\text{Cr}_{0.1}\text{N}$, $\text{Al}_{0.75}\text{Cr}_{0.25}\text{N}/\text{Al}_{0.85}\text{Cr}_{0.15}\text{N}$, and $\text{Al}_{0.75}\text{Cr}_{0.25}\text{N}/\text{Al}_{0.9}\text{Cr}_{0.1}\text{N}$) exhibit a dual phase mixed cubic wurtzite structure.

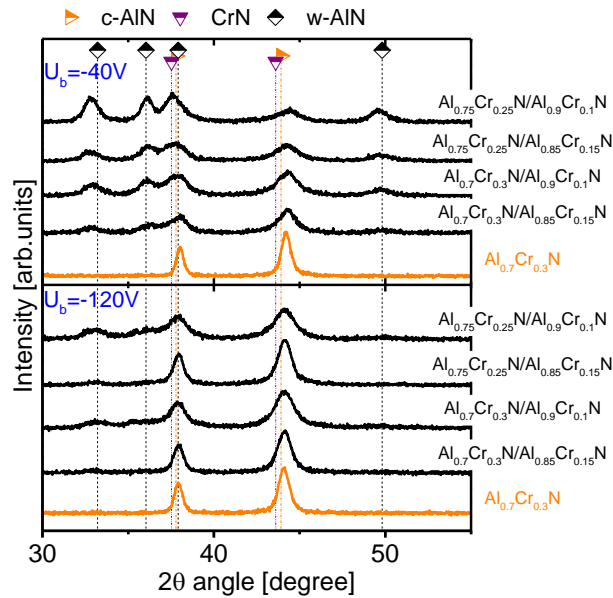


Fig. 5.3.1: XRD patterns for the monolithically grown $\text{Al}_{0.7}\text{Cr}_{0.3}\text{N}$ as well as for the multilayered coatings in the as deposited state when applying bias potentials of -40 and -80 V

More details about the chemical composition, the as deposited structure and properties of these coatings is reported in ref. [111]. For easier reading and clear correlation to the used targets we will use the target composition when referring to the coatings. Hence, $\text{Al}_{0.7}\text{Cr}_{0.3}\text{N}$ when using just $\text{Al}_{0.7}\text{Cr}_{0.3}$ targets, and $\text{Al}_{0.7}\text{Cr}_{0.3}\text{N}/\text{Al}_{0.85}\text{Cr}_{0.15}\text{N}$, $\text{Al}_{0.7}\text{Cr}_{0.3}\text{N}/\text{Al}_{0.9}\text{Cr}_{0.1}\text{N}$, $\text{Al}_{0.75}\text{Cr}_{0.25}\text{N}/\text{Al}_{0.85}\text{Cr}_{0.15}\text{N}$, and $\text{Al}_{0.75}\text{Cr}_{0.25}\text{N}/\text{Al}_{0.9}\text{Cr}_{0.1}\text{N}$ when combining different target compositions. With increasing the bias potential, the phase of the cubic structure increases on the expense of the hexagonal wurtzite phase. With increasing bias the compressive stresses increase, favoring the formation of the denser packed cubic structure. For example,

cubic structured AlN exhibits a $\sim 26\%$ lower specific volume than its hexagonal wurtzite structured counterpart [107]. Additionally, coherency strains between the low Al containing layers ($\text{Al}_{0.7}\text{Cr}_{0.3}\text{N}$ and $\text{Al}_{0.75}\text{Cr}_{0.15}\text{N}$) and the high Al containing layers ($\text{Al}_{0.85}\text{Cr}_{0.15}\text{N}$) support the cubic phase stabilization within these multilayers. Thus, especially for the $\text{Al}_{0.7}\text{Cr}_{0.3}\text{N}/\text{Al}_{0.85}\text{Cr}_{0.15}\text{N}$ and the $\text{Al}_{0.75}\text{Cr}_{0.25}\text{N}/\text{Al}_{0.85}\text{Cr}_{0.15}\text{N}$ multilayers a predominant cubic structure is observed, particularly when applying a high bias potential of -120 V .

Figure 5.3.2a, cross sectional TEM image of $\text{Al}_{0.75}\text{Cr}_{0.25}\text{N}/\text{Al}_{0.9}\text{Cr}_{0.1}\text{N}$, exemplarily shows that the multilayer coating grows very dense with clearly distinguishable layers when using a low bias potential of -40 V . As these multilayered coatings are prepared by rotating the substrate carousel in-between the four simultaneously operated cathodes, which are alternately equipped with two different target compositions, no sharp interfaces between the layers are obtained. The bilayer period of $\sim 38\text{ nm}$ is in good agreement with the calculated value of 42 nm (calculated from the deposition rate), published in our previous paper of the as-deposited properties of these coatings [111]. When using a high bias potential of -120 V , the individual layers are not clearly distinguishable anymore in the bright field TEM cross section, Fig. 5.3.2b. This is based on the higher deposition kinetics and increased ad-atom mobility provided by the high bias potential, leading to an intermixing of the individual layers and blurring of their interfaces [112].

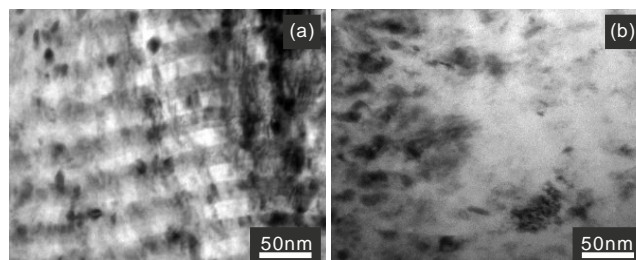


Fig. 5.3.2: Cross sectional TEM images of multilayered $\text{Al}_{0.75}\text{Cr}_{0.25}\text{N}/\text{Al}_{0.9}\text{Cr}_{0.1}\text{N}$ coatings in the as deposited state deposited at bias potentials of (a) -40 V and (b) -120 V .

5.3.2 DSC and TGA investigations

Figure 5.3.3 shows a typical DSC signal and the corresponding mass change as a function of annealing temperature for our $\text{Al}_{0.7}\text{Cr}_{0.3}\text{N}$ coatings, indicating comparable behavior for all bias potentials applied. Detailed studies on the thermal stability of $\text{Al}_x\text{Cr}_{1-x}\text{N}$ coatings have

shown that the exothermic feature in the temperature range 500-800 °C originates from recovery and relaxation processes of structural built-in defects. The exothermic features in the temperature range 800-1000 °C are due to nucleation and growth processes of w-AlN, superimposed by the strong endothermic dissociation process of Cr-N bonds [42,49]. Consequently, the material starts to release nitrogen and a transformation of the N-depleted matrix into h-Cr₂N occurs. This decomposition results in an increased mass loss with temperature, as detected by TGA at a temperature starting at around 1100 °C. The change in the slope of the TGA curve at ~1200 °C, where also the DSC feature shows a discontinuity, is based on the transformation of the majority of CrN phases to h-Cr₂N. Consequently, with increasing temperature now h-Cr₂N dissociates towards c-Cr under nitrogen release. As nitrogen is differently bonded within the cubic CrN phase than within the hexagonal Cr₂N phase the nitrogen release rate and consequently the mass loss is different. The nitrogen release is nearly finalized at ~1350 °C, where no further DSC features or mass loss can be detected.

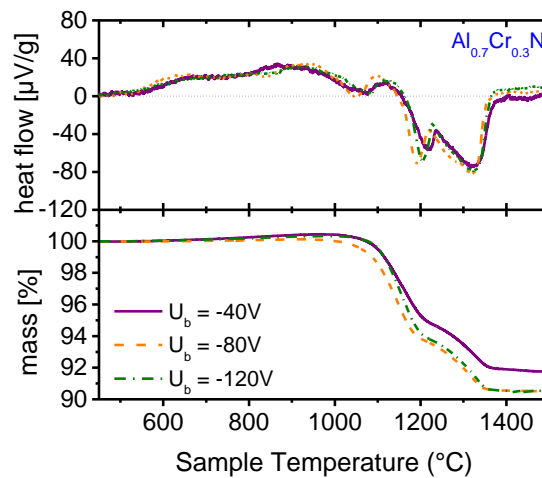


Fig. 5.3.3: DSC and TGA signals for monolithically grown Al_{0.7}Cr_{0.3}N coatings using different bias potentials.

The DSC spectra and mass loss of Al_{0.7}Cr_{0.3}N/Al_{0.85}Cr_{0.15}N multilayered coatings, Fig. 5.3.4 show that the first huge endothermic feature and onset of mass loss is shifted to lower temperatures as compared with Al_{0.7}Cr_{0.3}N coatings, compare Fig. 5.3.3. With increasing bias potential, a moderate shift (to higher temperatures) of these features can be detected, which can especially be seen in the TGA signal. The pronounced layered structure of the

coatings, especially when prepared with low bias potential, see Fig. 5.3.2a, in addition to the mixed-phased composition provides many-diffusion pathways promoting the dissociation of Cr-N binds. As with increasing bias potential the individual layers are more intermixed and also the cubic phase fraction dominates – leading to a reduced fraction of phase boundaries which typically provide faster diffusion than grain boundaries – the fraction of high diffusion pathways is slightly reduced. This may in part explain the shift of the onset temperature for the endothermic features and mass to higher temperatures, when increasing the bias potential. However, the intensity of the endothermic features and the mass loss with temperature also strongly depends on the bias potential used, see Fig. 5.3.4.

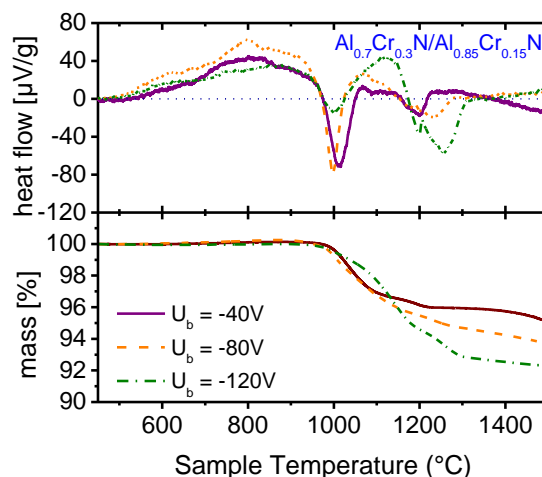


Fig. 5.3.4: DSC and TGA signals for $\text{Al}_{0.7}\text{Cr}_{0.3}\text{N}/\text{Al}_{0.85}\text{Cr}_{0.15}\text{N}$ multilayer coatings using different bias potentials.

With higher potential, for example with -120 V, the first endothermic feature (temperature range 900 - 1000 °C) is smaller, but the second one (1100 - 1300 °C) is way more pronounced as when using a lower bias potential, for example -40 V. Furthermore, the total mass loss up to around 1400 °C, is only 4% for the coatings prepared with -40 V, but nearly doubled (~8%) for the coatings prepared with -120 V. The intermixing of the layers with increasing bias potential, see Fig. 5.3.2b, can also explain the higher mass loss, as thereby the higher Al-containing layers are less effective to act as diffusion barriers. When the multilayer coatings are prepared with low bias potential, the individual high and low Al-containing layers are clearly separated, see Fig. 5.3.2a. Dissociation of Cr-N towards Cr

under release of nitrogen, will start in the Cr-rich layers. This process is retarded, if nitrogen is hindered to leave the material, which is the case when one type of the layers has a higher thermal stability, like in $\text{Al}_{0.75}\text{Cr}_{0.25}\text{N}/\text{Al}_{0.85}\text{Cr}_{0.15}\text{N}$.

These effects are even more pronounced for $\text{Al}_{0.75}\text{Cr}_{0.25}\text{N}/\text{Al}_{0.9}\text{Cr}_{0.1}\text{N}$ coatings, where higher Al containing layers are used. These multilayers show basically only one pronounced endothermic DSC feature, in the temperature range 900 to 1100 °C, see Fig. 5.3.5. Correspondingly, also the TGA data suggest only for one major nitrogen-release process, rather than two as obtained for the previously discussed samples. Especially, when the $\text{Al}_{0.75}\text{Cr}_{0.25}\text{N}/\text{Al}_{0.9}\text{Cr}_{0.1}\text{N}$ coatings are prepared with low bias potential, -40 V, the endothermic reaction is rather small and the mass-loss is nearly not detectable. Only at the highest temperatures, the decline in the DSC feature and TGA signal suggest for ongoing endothermic processes and nitrogen release. Corresponding to the discussion above, also here, the high Al-containing layer, $\text{Al}_{0.9}\text{Cr}_{0.1}\text{N}$, act as diffusion barriers and thereby suppress the dissociation of the lower Al-containing layers $\text{Al}_{0.75}\text{Cr}_{0.25}\text{N}$. Our DSC and TGA results, in combination with the cross-sectional TEM studies, suggest that the increased intermixing of the layers and increased defect density with increasing bias potential during preparation of the multilayers, reduce the diffusion barrier abilities of the high Al-containing layers. Consequently, the endothermic dissociation processes and mass loss are more pronounced for the coatings prepared with high bias potential as compared with the coating prepared with -40 V, see Fig. 5.3.5. The results obtained for the other multilayers, $\text{Al}_{0.7}\text{Cr}_{0.3}\text{N}/\text{Al}_{0.9}\text{Cr}_{0.1}\text{N}$ and $\text{Al}_{0.75}\text{Cr}_{0.25}\text{N}/\text{Al}_{0.85}\text{Cr}_{0.15}\text{N}$, are very similar to those obtained for $\text{Al}_{0.75}\text{Cr}_{0.25}\text{N}/\text{Al}_{0.9}\text{Cr}_{0.1}\text{N}$, only that the onset of the endothermic reaction shifts to slightly lower temperatures with decreasing overall Al content.

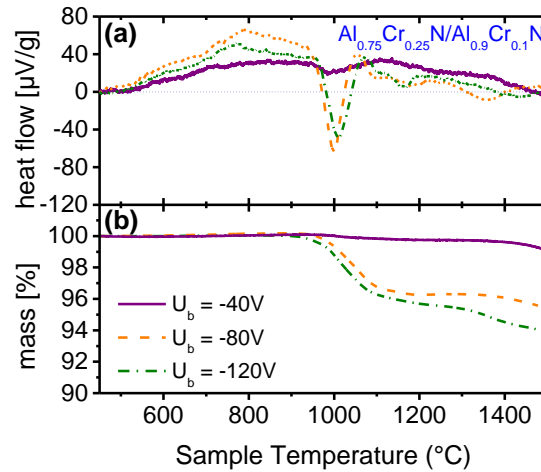


Fig. 5.3.5: DSC and TGA signals for $\text{Al}_{0.75}\text{Cr}_{0.25}\text{N}/\text{Al}_{0.9}\text{Cr}_{0.1}\text{N}$ multilayer coatings using different bias potentials.

XRD studies of the coatings after DSC measurements to 1500 °C, Fig. 5.3.6, clearly shows that with increasing overall Al content, the phase fraction of remaining h- Cr_2N and c- CrN increases. This is especially valid for the multilayers $\text{Al}_{0.7}\text{Cr}_{0.3}\text{N}/\text{Al}_{0.85}\text{Cr}_{0.15}\text{N}$, $\text{Al}_{0.7}\text{Cr}_{0.3}\text{N}/\text{Al}_{0.9}\text{Cr}_{0.1}\text{N}$, $\text{Al}_{0.75}\text{Cr}_{0.25}\text{N}/\text{Al}_{0.85}\text{Cr}_{0.15}\text{N}$, and $\text{Al}_{0.75}\text{Cr}_{0.25}\text{N}/\text{Al}_{0.9}\text{Cr}_{0.1}\text{N}$, prepared with low bias potential of -40 V, Fig. 5.3.6a. Whereas $\text{Al}_{0.7}\text{Cr}_{0.3}\text{N}$ fully decomposes into the stable phases w-AlN and c-Cr during the annealing treatment to 1500 °C, h- Cr_2N and c- CrN phases can additionally be detected for the multilayers. This clearly shows, that the as deposited supersaturated cubic and wurtzite $\text{Al}_x\text{Cr}_{1-x}\text{N}$ phases decompose, but Cr-N not fully dissociates to c-Cr and nitrogen, as suggested by the DSC and especially TGA data. Corresponding results are also reported for single phased hexagonal wurtzite structured $\text{Al}_{0.83}\text{Cr}_{0.17}\text{N}$ coatings upon annealing to 1450 °C [70], where c- CrN phases are encapsulated by thermally stable w-AlN and hence, their complete dissociation is shifted to higher temperatures.

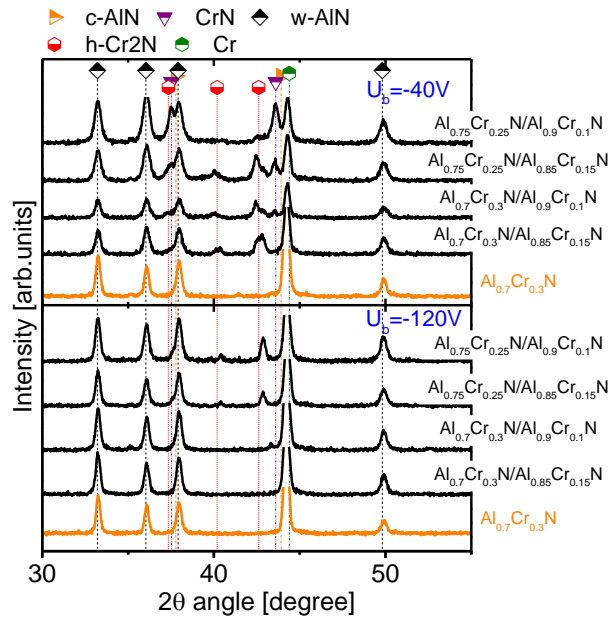


Fig. 5.3.6: XRD scans from the monolithically grown $Al_{0.7}Cr_{0.3}N$ as well as of the multilayered $Al_{0.7}Cr_{0.3}N/Al_{0.85}Cr_{0.15}N$, $Al_{0.7}Cr_{0.3}N/Al_{0.9}Cr_{0.1}N$, $Al_{0.75}Cr_{0.25}N/Al_{0.85}Cr_{0.15}N$, and $Al_{0.75}Cr_{0.25}N/Al_{0.9}Cr_{0.1}N$ coatings deposited at $U_b = -40$ V and -120 V, respectively after DSC to 1500 °C.

When prepared with higher bias potential, -120 V, the $Al_{0.7}Cr_{0.3}N/Al_{0.85}Cr_{0.15}N$ and $Al_{0.7}Cr_{0.3}N/Al_{0.9}Cr_{0.1}N$ coatings also show a completed decomposition to w-AlN and c-AlN after the DSC measurements to 1500 °C as the $Al_{0.7}Cr_{0.3}N$ coatings, see Fig. 5.3.6. Contrary, for the multilayers composed of higher Al-containing layers, $Al_{0.75}Cr_{0.25}N/Al_{0.85}Cr_{0.15}N$ and $Al_{0.75}Cr_{0.25}N/Al_{0.9}Cr_{0.1}N$, still h-Cr₂N phases can be detected. These results are in excellent agreement with the DSC and TGA data, showing retarded Cr-N dissociation processes and hence mass loss (i.e., nitrogen loss) for multilayers composed of high Al-containing layers when prepared with low bias potential. To further study and explain the ongoing processes during annealing of the coatings and the role of the individual layers, XRD investigations are conducted after isothermal vacuum annealing for 1 h at 700 °C up to 1300 °C, in steps of 100 °C.

5.3.3 Development of Structure with Annealing Temperature

The $Al_{0.7}Cr_{0.3}N$ coatings exhibit a single phase cubic structure up to $T_a = 700$ °C, for all three bias potentials studied, -40 , -80 , and -120 V, see Fig. 7a, b, and c, respectively. After annealing at $T_a = 800$ °C however, already small XRD peaks at $2\theta \sim 33.2$ and 36.1 deg –

indicative for w-AlN formation – can be detected. For $T_a = 900\text{ }^{\circ}\text{C}$, small XRD peaks at $2\theta \sim 40.3\text{ deg}$ and especially 42.8 deg suggest the formation of h-Cr₂N phases. This clearly indicates that the dissociation of Cr-N bonds towards the formation of h-Cr₂N under nitrogen release is preceded by the decomposition of the supersaturated Al_xCr_{1-x}N phases to precipitate w-AlN. This is in agreement with DSC, showing that the exothermic features lead over to the endothermic features, which are connected with a mass loss. For our materials, typical exothermic features are due to recovery of built-in structural defects (such as point defects and dislocations) leading to stress-relaxations, decomposition of supersaturated Al_xCr_{1-x}N towards x·AlN and (1-x)·CrN (i.e., precipitation of AlN), and recrystallization and grain growth processes. Typical endothermic features are due to the dissociation of CrN towards Cr₂N and finally Cr under nitrogen release. Here, we also need to mention that the XRD studies presented in Fig. 5.3.7, 5.3.8, and 5.3.9 are obtained after isothermal annealing for 1 h at T_a , whereas the DSC and TGA data present a dynamic treatment with 20 K/min up to 1500 °C.

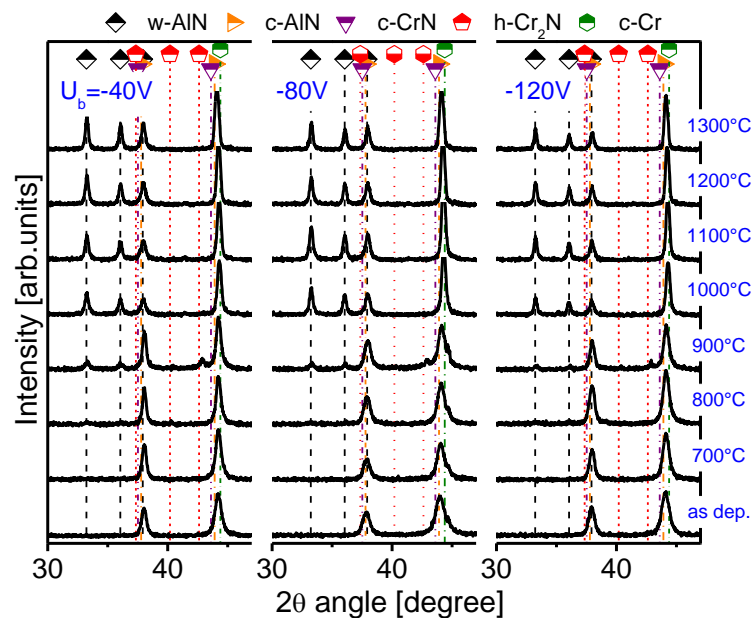


Fig. 5.3.7: XRD patterns of the monolithically grown Al_{0.7}Cr_{0.3}N powdered coatings at different bias potentials and after post deposition annealing at temperatures up to 1300 °C.

Consequently, distinct features during DSC and TGA are shifted to higher temperatures than their corresponding structural changes obtained by XRD after annealing at T_a . However, XRD patterns already indicate a completed transformation from c-Al_{0.7}Cr_{0.3}N into w-AlN and c-Cr

for $T_a = 1000\text{ }^{\circ}\text{C}$, Fig. 5.3.7. When further increasing T_a , the intensities of the XRD peaks increases and their width decreases, indicating grain growth [113]. In agreement with the DSC and TGA investigations no distinct different behavior can be identified for the $\text{Al}_{0.7}\text{Cr}_{0.3}\text{N}$ coatings when prepared with different bias potentials, compare Figs. 5.3.7a, b, and c.

For the multilayer coatings a different behavior is obtained as already suggested by the DSC and TGA investigations. As already mentioned above, during discussing the as deposited structure, the cubic phase fraction of these multilayers increases with increasing bias potential, compare Figs. 5.3.8a, b, and c. When the coatings are prepared with -120 V their majority phase is cubic structured with only small traces of hexagonal wurtzite phases, indicated by the very small XRD peaks, see Fig. 5.3.8c. For $T_a = 900\text{ }^{\circ}\text{C}$, the formation of h- Cr_2N can already be detected by XRD (see the peaks at $2\theta \sim 40.4$ and 42.8 deg), independent of the bias potential used. More important is, that for $T_a = 1000\text{ }^{\circ}\text{C}$, almost no Cr_2N can be detected anymore for the multilayer prepared with -120 V (similar to the results obtained for $\text{Al}_{0.7}\text{Cr}_{0.3}\text{N}$). The XRD pattern indicates, that the coating is already completely decomposed into the stable phases w-AlN and c-Cr. Contrary, the coatings prepared with lower bias potential, and especially that prepared with -40 V, exhibit h- Cr_2N phases even after annealing at $1300\text{ }^{\circ}\text{C}$. These results are in excellent agreement with DSC and TGA investigations, Fig. 5.3.4, showing that the multilayers prepared with lower bias potential (and especially that prepared with -40 V) exhibit lower exothermic features and lower mass loss.

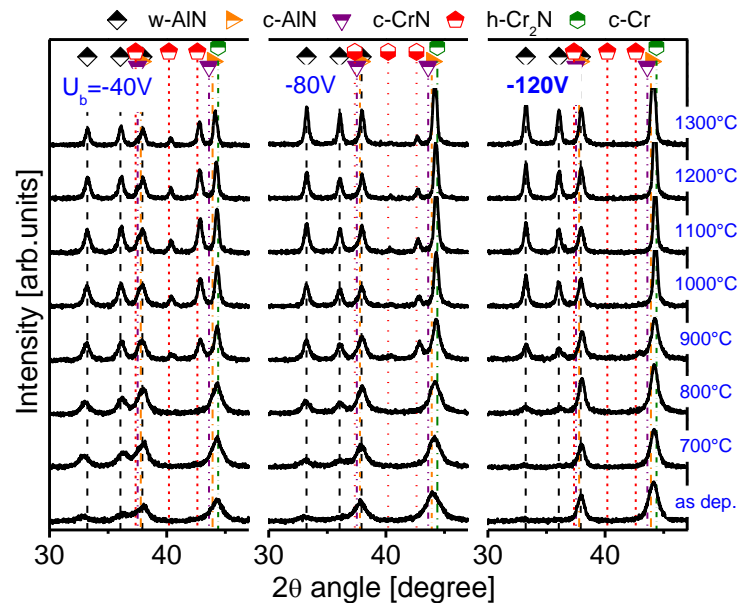


Fig. 5.3.8: XRD scans from the multilayered $Al_{0.7}Cr_{0.3}N/Al_{0.85}Cr_{0.15}N$ powdered coatings using different bias potentials and after annealing at temperatures up to 1300 °C.

Also for the higher Al-containing multilayers, $Al_{0.7}Cr_{0.3}N/Al_{0.9}Cr_{0.1}N$, h-Cr₂N can already be detected for $T_a = 900$ °C, see Fig. 5.3.9. But here, even for the coatings prepared with -120 V bias, h-Cr₂N phases can still be detected for $T_a = 1300$ °C. The structural development with T_a suggests a comparable behavior for the coatings prepared with -80 and -120 V. Contrary, the coating prepared with -40 V exhibits only small XRD peaks for h-Cr₂N formation, but besides that also the formation of c-CrN, see the XRD peak formation at $2\theta \sim 43.6$ deg for $T_a = 1000$ °C. After annealing at $T_a = 1300$ °C, this coating is clearly decomposed into w-AlN and c-CrN, with a small fraction of h-Cr₂N. Again, these results are in excellent agreement with DSC and TGA investigations showing almost no endothermic features and mass loss for the $Al_{0.75}Cr_{0.25}N/Al_{0.9}Cr_{0.1}N$ multilayers prepared with -40 V.

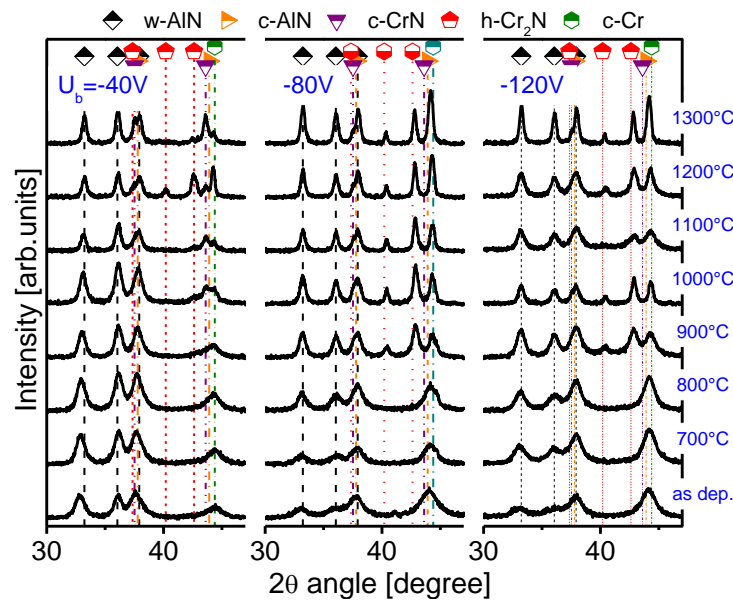


Fig. 5.3.9: XRD diffraction pattern of the $\text{Al}_{0.75}\text{Cr}_{0.25}\text{N}/\text{Al}_{0.9}\text{Cr}_{0.1}\text{N}$ Multilayer at $U_b = -40, -80$ and -120 V.

5.3.4 Development of Mechanical Properties with Annealing Temperature

Our monolithically grown $\text{Al}_{0.7}\text{Cr}_{0.3}\text{N}$ coating exhibit a hardness of about 32.6 GPa in the as deposited state prepared with a bias potential of -40 V, which increases to a maximum of ~ 34.6 GPa with increasing T_a to 700°C , Fig. 5.3.10a. Previous studies show, that this hardness-increase is based on a fine and even precipitation of w-AlN [53]. With further increasing T_a to 1100°C the hardness decreases to ~ 23 GPa, due to further $\text{Al}_x\text{Cr}_{1-x}\text{N}$ decomposition and growth of the w-AlN precipitates. Even after annealing at $T_a \geq 1200^\circ\text{C}$, the hardness is with ~ 23 GPa unchanged to the previous temperature, indicating that the decomposition of our $\text{Al}_{0.7}\text{Cr}_{0.3}\text{N}$ coating into w-AlN and c-Cr is completed. This is in agreement to the XRD studies, Fig. 5.3.7, showing only w-AlN and c-Cr phases and nearly no changes in intensity and width of their XRD peaks for $T_a \geq 1200^\circ\text{C}$. (However, our single phase wurtzite structured $\text{Al}_{0.9}\text{Cr}_{0.1}\text{N}$ coatings show hardnesses of ~ 20 and 25 GPa over the entire annealing temperature range using a bias potential of -40 V and -120 V, respectively). The multilayered coatings, $\text{Al}_{0.7}\text{Cr}_{0.3}\text{N}/\text{Al}_{0.85}\text{Cr}_{0.15}\text{N}$ and $\text{Al}_{0.75}\text{Cr}_{0.25}\text{N}/\text{Al}_{0.9}\text{Cr}_{0.1}\text{N}$, exhibit low hardnesses between 15 and 17 GPa in their as deposited state, when prepared with low bias potential of -40 V, see Fig. 5.3.10a, due to their low degree in crystallinity, highlighted by broad XRD peaks around the cubic and wurtzite phases. The $\text{Al}_{0.7}\text{Cr}_{0.3}\text{N}/\text{Al}_{0.85}\text{Cr}_{0.15}\text{N}$

coating exhibits a hardness increase to ~ 21 GPa for $T_a \geq 900$ °C. Here, the XRD peaks become more pronounced, see Fig. 5.3.8, and the clear w-AlN and h-Cr₂N phase formation indicate ongoing decomposition and dissociation reactions. However, our highest Al containing multilayer Al_{0.75}Cr_{0.25}N/Al_{0.9}Cr_{0.1}N prepared with low bias of -40 V, shows this hardness increase to ~ 23 GPa only for $T_a \geq 1000$ °C, see Fig. 5.3.10a. Again, this is in agreement with the structural evolution of this multilayer, showing decomposition processes for $T_a \geq 1000$ °C, see the XRD patterns ins Fig. 5.3.8.

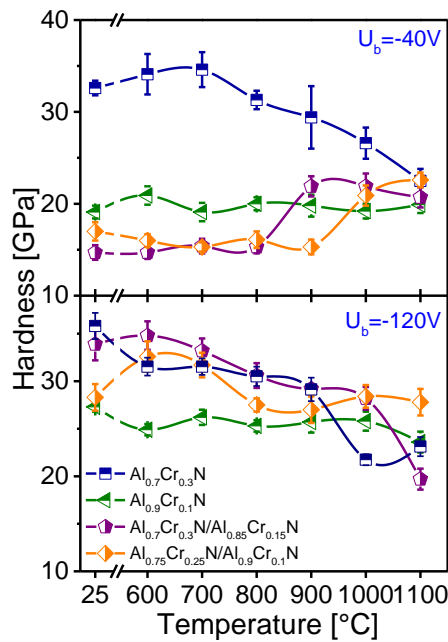


Fig. 5.3.10: Hardness of monolithically grown Al_{0.7}Cr_{0.3}N and Al_{0.9}Cr_{0.1}N as well as the multilayered Al_{0.7}Cr_{0.3}N/Al_{0.85}Cr_{0.15}N and Al_{0.75}Cr_{0.25}N/Al_{0.9}Cr_{0.1}N coatings after annealing temperatures up to 1100 °C.

Interestingly, the hardness of these three coatings, Al_{0.7}Cr_{0.3}N, Al_{0.7}Cr_{0.3}N/Al_{0.85}Cr_{0.15}N and Al_{0.75}Cr_{0.25}N/Al_{0.9}Cr_{0.1}N, prepared with -40 V bias potential, is similar for $T_a = 1100$ °C, although the structure is different. Please remember, Al_{0.7}Cr_{0.3}N is composed of w-AlN and c-Cr phases, Al_{0.7}Cr_{0.3}N/Al_{0.85}Cr_{0.15}N is composed of w-AlN and h-Cr₂N, and c-CrN phases, and Al_{0.75}Cr_{0.25}N/Al_{0.9}Cr_{0.1}N is composed of w-AlN and c-CrN phases, for $T_a = 1100$ °C. This clearly shows, that the hardness is mainly determined by the dominating w-AlN phase after this annealing treatment to 1100 °C. Hardnesses of ~ 20 GPa for arc evaporated single phase AlN coatings after annealing to 1100 °C were found by Reiter et al. [50].

Our $\text{Al}_{0.7}\text{Cr}_{0.3}\text{N}/\text{Al}_{0.85}\text{Cr}_{0.15}\text{N}$ and $\text{Al}_{0.75}\text{Cr}_{0.25}\text{N}/\text{Al}_{0.9}\text{Cr}_{0.1}\text{N}$ multilayer coatings deposited at a bias potential of -120 V demonstrate high hardnesses of ~ 34 GPa and ~ 28 GPa, respectively – similar to the cubic structured $\text{Al}_{0.7}\text{Cr}_{0.3}\text{N}$ coating – in the as deposited state, see Fig. 5.3.10b. Up to an annealing temperature of 700 °C hardnesses between 33 and 35 GPa are measured for the $\text{Al}_{0.7}\text{Cr}_{0.3}\text{N}/\text{Al}_{0.85}\text{Cr}_{0.15}\text{N}$ coatings. This correlates well with XRD investigations, where a pronounced cubic structure is detected and no structural changes are observed up to 700 °C. For annealing temperatures between 800 °C to 1000 °C hardness is decreased to about 20 GPa, related to the precipitation and growth of the w-AlN phase. The $\text{Al}_{0.75}\text{Cr}_{0.25}\text{N}/\text{Al}_{0.9}\text{Cr}_{0.1}\text{N}$ coatings deposited at - 120 V shows a hardness increase to 32-33 GPa when increasing the annealing temperature to 700 °C. However, for $T_a = 800$ °C hardness is decreased to ~ 27 GPa due to further formation and growth of w-AlN. As mentioned above, a hardness increase is only obtained when w-AlN precipitates are small in size and evenly distributed. Although, according to XRD, a further increase of the annealing temperature results in the formation of Cr_2N , (see Fig. 5.3.9), the hardness of our $\text{Al}_{0.75}\text{Cr}_{0.25}\text{N}/\text{Al}_{0.9}\text{Cr}_{0.1}\text{N}$ remains nearly constant between 27 and 28.4 GPa. For annealing temperatures above 900 °C this can be related to the unchanged w-AlN, c-Cr, and h- Cr_2N containing multiphase structure.

5.4 Discussion

Cathodic arc evaporation of powder metallurgically prepared $\text{Al}_{0.7}\text{Cr}_{0.3}$ targets result in the formation of single-phase cubic structured $\text{Al}_{0.7}\text{Cr}_{0.3}\text{N}$ coatings with an as deposited hardness of ~ 33 GPa when prepared with -40 V bias potential. The hardness increases to ~ 36 GPa by increasing the bias potential to -120 V, due to an increased fraction of structural built-in defects and densification of the growth morphology. However, the hardness rapidly decreases to ~ 31 GPa upon annealing to 600 °C. After annealing at $T_a \geq 1000$ °C, the hardness is only ~ 22 GPa, as here the supersaturated $\text{Al}_{0.7}\text{Cr}_{0.3}\text{N}$ phase fully decomposes to w-AlN and c-Cr phases. The cubic Cr phases are the result of the Cr–N dissociation towards Cr under N_2 -release. The $\text{Al}_{0.7}\text{Cr}_{0.3}\text{N}$ prepared with lower bias potential still exhibit hardnesses of ~ 27 GPa for $T_a = 1000$ °C suggesting for reduced Cr–N dissociation processes, as indicated by DSC-TGA investigations. The slightly increased thermal stability of the

coatings prepared with lower bias potential is due to their lower density of structural built-in defects, leading to less pronounced diffusion pathways.

The behavior of the multilayer arrangements as a function of the bias potential used is mainly based on two counteractive effects. Especially when layers are combined that favor the cubic and the hexagonal wurtzite type structure, as relevant for our systems $\text{Al}_{0.7}\text{Cr}_{0.3}\text{N}/\text{Al}_{0.85}\text{Cr}_{0.15}\text{N}$, $\text{Al}_{0.7}\text{Cr}_{0.3}\text{N}/\text{Al}_{0.9}\text{Cr}_{0.1}\text{N}$, $\text{Al}_{0.75}\text{Cr}_{0.25}\text{N}/\text{Al}_{0.85}\text{Cr}_{0.15}\text{N}$, and $\text{Al}_{0.75}\text{Cr}_{0.25}\text{N}/\text{Al}_{0.9}\text{Cr}_{0.1}\text{N}$, their competitive growth will typically result in a very fine grained microstructure with a huge fraction of grain and especially phase boundaries. Increasing the bias potential, which promotes the growth of the cubic phases of arc-evaporated coatings, leads to the formation of nearly single-phase cubic structured $\text{Al}_{0.7}\text{Cr}_{0.3}\text{N}/\text{Al}_{0.85}\text{Cr}_{0.15}\text{N}$ multilayers. Hence, their fraction of phase boundaries decreases. But the highest Al-containing multilayers, $\text{Al}_{0.75}\text{Cr}_{0.25}\text{N}/\text{Al}_{0.9}\text{Cr}_{0.1}\text{N}$, change from nearly single-phased hexagonal wurtzite type structured towards fine-grained cubic and hexagonal structured coatings with increasing bias potential. Hence, their fraction of phase boundaries increases with increasing bias potential.

Consequently, with increasing bias potential not just the structural built-in defects (like point and line defects) increases, but the fraction of the phase boundaries can either decrease or increase. This has a tremendous effect on the thermal stability of such coatings and can explain the different dependence on bias potential and layer arrangement.

Increasing the bias potential during growth of our $\text{Al}_{0.7}\text{Cr}_{0.3}\text{N}/\text{Al}_{0.85}\text{Cr}_{0.15}\text{N}$ multilayers increases the onset for decomposition and especially Cr–N dissociation processes. This is based on the decreased fraction of phase boundaries and the densification of the growth morphology in general. Nevertheless, the rate of decomposition and dissociation processes is lower when the multilayers are prepared with low bias potential, in agreement with the results obtained for homogenously grown coatings. However, the $\text{Al}_{0.75}\text{Cr}_{0.25}\text{N}/\text{Al}_{0.9}\text{Cr}_{0.1}\text{N}$ multilayers exhibit the highest onset temperature as well as lowest rate for decomposition and dissociation processes when prepared with low bias potential. Actually, when prepared with -40 V bias potential, they exhibit nearly no mass-loss even up to annealing temperatures of 1500 °C. With increasing bias potential, the mass-loss increases, which is a clear indication for N_2 -release due to dissociation of the Cr–N bonds. This behavior is because $\text{Al}_{0.75}\text{Cr}_{0.25}\text{N}/\text{Al}_{0.9}\text{Cr}_{0.1}\text{N}$ multilayers are nearly single-phase hexagonal structured in

the as deposited state when prepared with -40 V bias. With increasing bias potential, which promotes the formation of cubic phases in these material systems, the fraction of phase boundaries increases and thereby also the fraction of fast diffusion pathways.

The hardness evolution with annealing temperature of our coatings, agrees with their structural changes. The as deposited single-phase cubic structured coatings, $\text{Al}_{0.7}\text{Cr}_{0.3}\text{N}$, experience an earlier hardness reduction when prepared with high bias potential. Therefore, the hardness after annealing at 900 °C is only 24 GPa for the coating prepared with -120 V but still 28 GPa for the coating prepared with -40 V. Here, the hardness reduction due to the annealing treatment more than counteracts the hardness increase due to increased bias. This is different for the multilayer coatings, although they also show in general a higher thermal stability for the coatings prepared with low bias potential. But the hardness reduction with $T_a \leq 1000$ °C, of the coatings prepared using -120 V bias, is less than the hardness increase in the as deposited state when increasing the bias potential from -40 to -120 V. Hence, the multilayers prepared with -120 V bias potential outperform their lower bias potential counterparts with respect to hardness for annealing temperatures up to 1000 °C.

5.5 Summary and Conclusion

Various $\text{Al}_x\text{Cr}_{1-x}\text{N}$ multilayer arrangements, obtained by using two different chemical compositions for the four target cathodes, are prepared by arc evaporation in N_2 atmosphere at 500 °C. Based on previous as deposited studies, the multilayers $\text{Al}_{0.7}\text{Cr}_{0.3}\text{N}/\text{Al}_{0.85}\text{Cr}_{0.15}\text{N}$, $\text{Al}_{0.7}\text{Cr}_{0.3}\text{N}/\text{Al}_{0.9}\text{Cr}_{0.1}\text{N}$, $\text{Al}_{0.75}\text{Cr}_{0.25}\text{N}/\text{Al}_{0.85}\text{Cr}_{0.15}\text{N}$, and $\text{Al}_{0.75}\text{Cr}_{0.25}\text{N}/\text{Al}_{0.9}\text{Cr}_{0.1}\text{N}$ are studied in detail for their thermal stability and compared with coatings prepared with $\text{Al}_{0.7}\text{Cr}_{0.3}$ targets.

Based on our results we can conclude, that among the $\text{Al}_x\text{Cr}_{1-x}\text{N}$ coatings studied, especially the $\text{Al}_{0.75}\text{Cr}_{0.25}\text{N}/\text{Al}_{0.9}\text{Cr}_{0.1}\text{N}$ multilayers prepared with -120 V, exhibiting around 30 ± 3 GPa over the entire temperature range up to 1100 °C, show superior thermal stability combined with excellent mechanical properties. This is based on the beneficial effect of the bias potential to prepare dense coatings, especially when they are composed of multiple phases,

and the specific arrangement of $\text{Al}_{0.75}\text{Cr}_{0.25}\text{N}$ and $\text{Al}_{0.9}\text{Cr}_{0.1}\text{N}$ layers with a bilayer period of ~38 nm.

CHAPTER 6

Diffusion behavior of C, Cr, and Fe in arc evaporated TiN- and CrN-based coatings and their influence on thermal stability and hardness

6.1 Introduction

Transition metal based nitrides like TiN, $Ti_{1-x}Al_xN$, CrN, and $Cr_{1-x}Al_xN$ are highly valued as protective coatings on tools for numerous machining and forming applications such as cutting inserts, dies, or molds due to their outstanding properties [46,50,106,114–116]. In general, the properties – e.g. hardness, oxidation resistance, and thermal stability – of the binary transition metal nitrides can significantly be increased by the addition of Al [6,117]. $Ti_{1-x}Al_xN$ and $Al_xCr_{1-x}N$ coatings crystallize in the single phase cubic (NaCl type, c) structure for AlN contents (x) up to ~ 0.67 and 0.7, respectively [9,50]. For higher AlN contents a dual phase structure composed of cubic and hexagonal (ZnS wurtzite-type, w) phases, or even the formation of a single phase w-structure is promoted. These typically exhibit decreased mechanical properties and decreased coating performance as their single-phase cubic structured counterparts [9,50].

Ternary transition metal nitrides exceed their binary counterparts in numerous properties. Nevertheless, Ávila et al. [118] showed that during machining operations the wear performance of TiN coatings can be better than their ternary $Ti_{1-x}Al_xN$ counterparts. Depending on physical and chemical properties of the work-piece and cutting tool material temperatures of more than 1000 °C are obtained at the cutting edge. This of course depends also on the cutting parameters and cutting tool geometry [22]. However, due to these high temperatures, diffusion processes and material transfer between cutting tool, coating, and work-piece are promoted. This is detrimental for the coating performance, as especially diffusion driven wear can be severe. Even though the thermal stability and oxidation behavior of such CrN and TiN based coatings is well investigated, there are only limited reports about the diffusion of C, Cr, or Fe in such nitride coatings. Most of the data

published focus on nitride coatings like TiN, TaN, and WN to be used as copper diffusion barriers [76,78,119]. Grigorov et al. [120] reported that the diffusion coefficient of Fe in TiN is in the range of $3 \cdot 10^{-14}$ to $5 \cdot 10^{-14}$ cm²/s. All of them propose that the diffusion mainly occurs along high diffusion pathways such as grain and especially column boundaries, and therefore strongly depends on the microstructure and thus on the deposition parameters used.

Here we study the diffusion of C, Cr, and Fe in arc evaporated TiN, Ti_{0.5}Al_{0.5}N, CrN, and Cr_{0.3}Al_{0.7}N coatings, for a better understanding of the complex interactions and wear behavior during machining operations between work-piece, cutting tool, and its coating.

6.2 Experimental

All coatings were synthesized in a Balzers INNOVA industrial scaled deposition plant using powder metallurgically prepared Ti, Ti_{0.5}Al_{0.5}, Cr, and Al_{0.7}Cr_{0.3}, targets (Plansee SE). Prior to the depositions, the substrates used were ultrasonically cleaned in acetone and ethanol, respectively. Afterwards, they were mounted on a two-fold rotating carousel with a minimum target to substrate distance of ~25 cm and thermally cleaned for 30 min at 500 °C and Ar ion etched within the chamber. In order to provide equal good adhesion for all coatings, a TiN interlayer was deposited using a bias potential (U_b) of -40 V, an arc current of 160 A, and a temperature of 500 °C. Arc currents of 160 and 200 A were used for the deposition of TiN and Ti_{0.5}Al_{0.5}N, respectively, and 150 A for CrN and Cr_{0.3}Al_{0.7}N. Further on, the temperature during deposition was kept constant at 500 °C and a bias potential of -80 V was applied. Ball-crater technique and cross-sectional scanning electron microscopy (SEM) show an interlayer thickness of 0.5 µm and coating thicknesses between 3.1 and 3.2 µm for the TiN, Ti_{0.5}Al_{0.5}N, CrN, and Cr_{0.3}Al_{0.7}N coatings. On top of these coatings either a C, Cr, or Fe layer (around 300 nm thin) was deposited using an AGAR SEM Carbon Coater, a Quorum “Q150T S” sputter coater, and an AJA “Orion 5” DC magnetron sputtering system, respectively. Subsequently, the samples were annealed in a vacuum furnace (CENTORR Vacuum Industries “LF-Series”, base pressure < $2 \cdot 10^{-5}$ mbar) at temperatures of 600, 800, and 1000 °C with a heating rate of 20 K/min and a holding time of 30 min. Additionally,

annealing times of 10, 100, and 1000 min were chosen for an annealing temperature of 600 °C.

The film morphology was studied with a Hitachi SU 8030 scanning electron microscope. A PANalytical “Empyrean” diffractometer, equipped with CuK α radiation source, in Bragg Brentano configuration was used for X-ray diffraction (XRD) analyses. Hardness (H) measurements were conducted with a CSIRO ultra micro indentation system equipped with a Berkovich indenter. Normal loads ranging from 30 to 10 mN in steps of 0.5 mN were applied and the results were calculated from the loading and unloading segments according to Oliver and Pharr [34]. Prior to the XRD and hardness measurements, the annealed samples were polished to avoid or at least minimize the interference with the C, Cr, and Fe top layers. Line scans on annealed and polished cross sectional samples – by energy-dispersive X-ray (EDX) measurements with an Oxford Instruments device attached to the SEM (acceleration voltage of 20 keV) – were conducted to derive the medium diffusion lengths of the elements C, Cr, and Fe. Further on, EDX line scanning was conducted in a FEI TECNAI F20 transition electron microscope (TEM) equipped with an EDAX EDX detector in order to verify the results revealed within the SEM.

6.3 Results and discussion

6.3.1 Morphology and structure

SEM fracture cross sections of our TiN, Ti_{0.5}Al_{0.5}N, CrN, and Cr_{0.3}Al_{0.7}N coatings demonstrate a dense and columnar microstructure as well as comparable coating thicknesses between 3.1 and 3.2 μ m in their as deposited state, please see for example the TiN coating with a C top layer in Fig. 6.3.1a. After vacuum annealing to 600, 800, and even 1000 °C the TiN coating still exhibits a dense, columnar microstructure, suggesting for a high thermal stability [121], see Figs. 6.3.1b, c, and d, respectively.

Also for the other coatings Ti_{0.5}Al_{0.5}N, CrN, and Cr_{0.3}Al_{0.7}N, the top layers (C, Cr, and Fe) are still present after the annealing treatments (even for T_a = 1000 °C), see their cross sections for T_a = 800 °C in Figs. 6.3.2a, b, and c, respectively. Hence an infinite diffusion source is relevant for our diffusion studies. After annealing at 800 °C, all coatings still have a

columnar microstructure. The binary coatings, TiN and especially CrN, exhibit a coarser microstructure than their Al-containing counterparts, see Figs. 6.3.1 and 6.3.2.

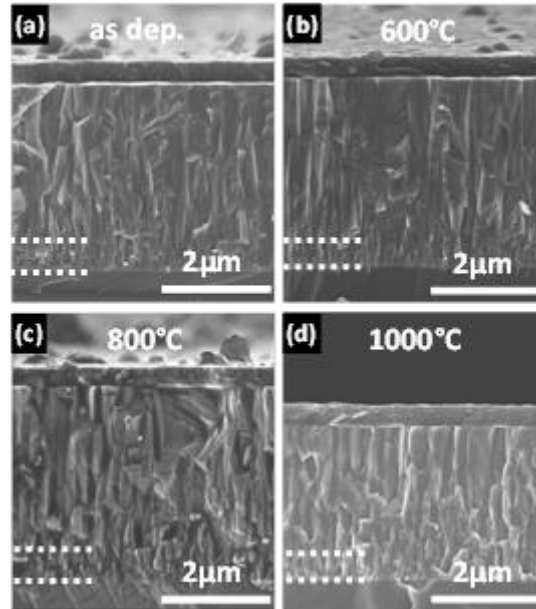


Fig. 6.3.1: SEM fracture cross sections of TiN coatings with a C top layer in the (a) as deposited state as well as after annealing to (b) 600 °C, (c) 800 °C, and (d) 1000 °C. The horizontal dashed lines indicate the TiN interlayer between the substrate and the TiN coating.

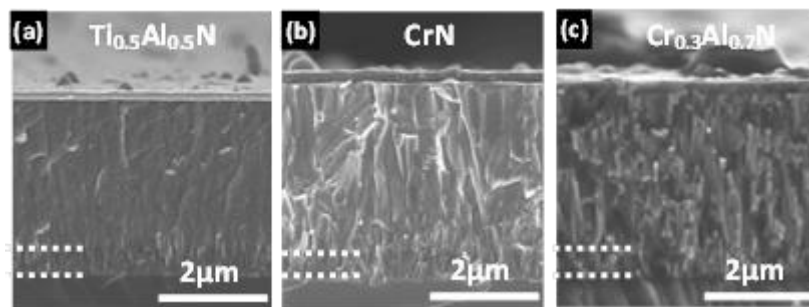


Fig. 6.3.2: SEM fracture cross sections of (a) $\text{Ti}_{0.5}\text{Al}_{0.5}\text{N}$, (b) CrN, and (c) $\text{Cr}_{0.3}\text{Al}_{0.7}\text{N}$ coatings after annealing to 800 °C. The horizontal dashed lines indicate the TiN interlayer between the substrate and the individual coatings.

Figures 6.3.3a, b, and c show XRD patterns of TiN with C, Cr, and Fe top layers in the as deposited state and after 30 min annealing at 600, 800, and 1000 °C, respectively. All coatings exhibit a single phase cubic structure with a preferred (111) orientation in the as

deposited and annealed state. The width of the XRD peaks decreases with increasing annealing temperature, suggesting for temperature induced grain growth and relaxation processes. Further on, C and Fe have no significant effect on the structure of TiN as no additional phases can be detected by XRD, see Figs. 6.3.3a and c, respectively. However, when a Cr top layer was present, the formation of hexagonal (h) Cr_2N phases can be detect already after 10 min annealing at 600 °C, see Fig. 6.3.3b.

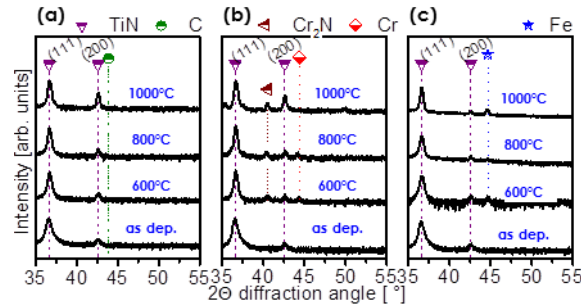


Fig. 6.3.3: XRD patterns of TiN coatings with (a) C, (b) Cr, and (c) Fe top layers in the as deposited state as well as after annealing to 600, 800, and 1000 °C.

$\text{Ti}_{0.5}\text{Al}_{0.5}\text{N}$ coatings exhibit a preferred (200) orientation in the as deposited state, see Figs. 4a, b, and c. Increasing the annealing temperature to 600 °C leads to the development of broader and asymmetric c- $\text{Ti}_{1-x}\text{Al}_x\text{N}$ matrix peaks. This suggests for ongoing decomposition of the supersaturated c- $\text{Ti}_{1-x}\text{Al}_x\text{N}$ to form Al-enriched and –depleted cubic domains and is in agreement to many previous studies [30,79,115].

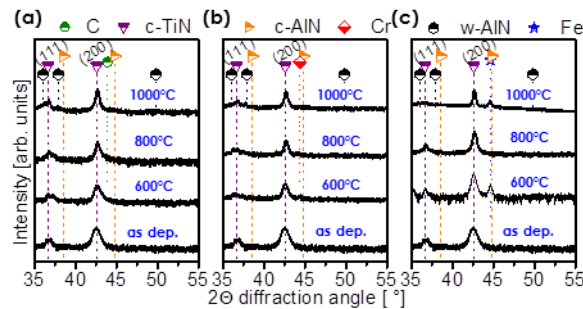


Fig. 6.3.4: XRD patterns of $\text{Ti}_{0.5}\text{Al}_{0.5}\text{N}$ coatings with (a) C, (b) Cr, and (c) Fe top layers in the as deposited state as well as after annealing to 600, 800, and 1000 °C.

Further increasing the annealing temperature to 800 °C leads to clearly detectable c-AlN XRD peaks, which verify spinodal decomposition. A corresponding effect is observed when increasing the holding time to 100 min and longer during isothermal annealing at 600 °C. However, even after 1000 min annealing at 600 °C the spinodal decomposition is not completed, as the XRD peaks from the c-Ti_{1-x}Al_xN matrix are still very pronounced. After annealing at 1000 °C, the formation of hexagonal wurtzite type AlN can clearly be detected. The decomposition process towards the stable constituents c-TiN and w-AlN will result in the transformation of the columnar structure towards a more equiaxed structure upon annealing, as shown by transmission electron microscopy [30]. No significant difference in structural development of our Ti_{0.5}Al_{0.5}N coatings can be detected by XRD if no top layer is present or the top layer consists of C, Cr, or Fe.

Figures 6.3.5a, b, and c show XRD patterns of our CrN coatings in the as deposited state and after 30 min annealing at 600, 800, and 1000 °C for the used C, Cr, and Fe top layers, respectively. In addition to the Cr–N phases, we have also indicated the position for TiN, which is used as an interlayer between substrate and coating. The XRD results show, that the annealing temperature, after which hexagonal h-Cr₂N can already be detected, strongly depends on the used top layer. The formation of h-Cr₂N indicates dissociation processes of the CrN phase towards cubic Cr under nitrogen release [42]. When C and Fe diffuses into the coating from the top layers, the formation of h-Cr₂N can only be detected for T_a = 800 and 1000 °C, see Figs. 6.3.5a and 6.3.5c, respectively. The shift of the Fe XRD peak to lower 2 θ diffraction angles, Fig. 6.3.5c, as compared to the standard JCPDF position with increasing annealing temperature suggests that nitrogen is dissolved within Fe. Here we need to mention again, that although we removed the top layers prior to the XRD investigations, remaining top layer particles can still be present and contribute to the XRD peaks of C, Cr, and Fe in our studies.

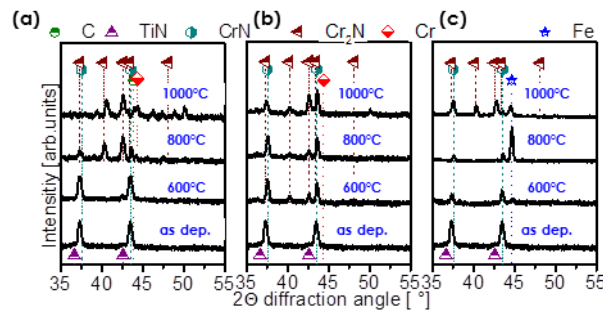


Fig. 6.3.5: XRD patterns of CrN coatings with (a) C, (b) Cr, and (c) Fe top layers in the as deposited state as well as after annealing to 600, 800, and 1000 °C.

When Cr diffuses into the coating from the Cr top layer, h-Cr₂N XRD peaks can already be detected after annealing at 600 °C. These results correspond to the observations made for the diffusion studies of Cr into TiN coatings, compare Fig. 6.3.3c, and suggest for an interaction of the Cr top layer with the nitride coating underneath. Furthermore, our XRD studies show that the decomposition strongly depends on the annealing time. Already after 10 min annealing at 600 °C a Cr₂N phase can be detected for the CrN coating with a Cr top layer. Contrary, when a C or Fe top layer is present during annealing at 600 °C, the formation of h-Cr₂N can only be detected after 100 and 1000 min, respectively.

The c-Al_xCr_{1-x}N coatings do not exhibit any significant structural changes, detectable by XRD, upon annealing to 800 °C, when using C or Fe top layers. Only for T_a = 1000 °C, the formation of w-AlN and c-Cr phases, via the formation of h-Cr₂N under nitrogen release [49], can be detected. However, when using a Cr top layer, the formation of w-AlN and h-Cr₂N phases can already be detected after annealing at 800 °C (results are not shown).

Due to various annealing treatments and the occurring phase decomposition and dissociation processes, the average crystallite size, obtained by Warren Averbach analyzes of the individual XRD patterns, changes significantly with T_a, see Fig. 6.3.6.

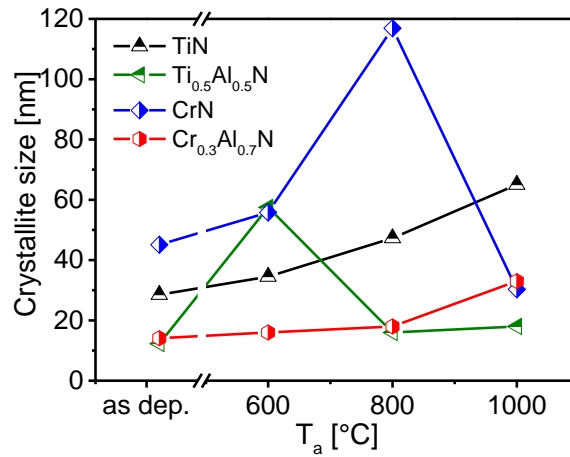


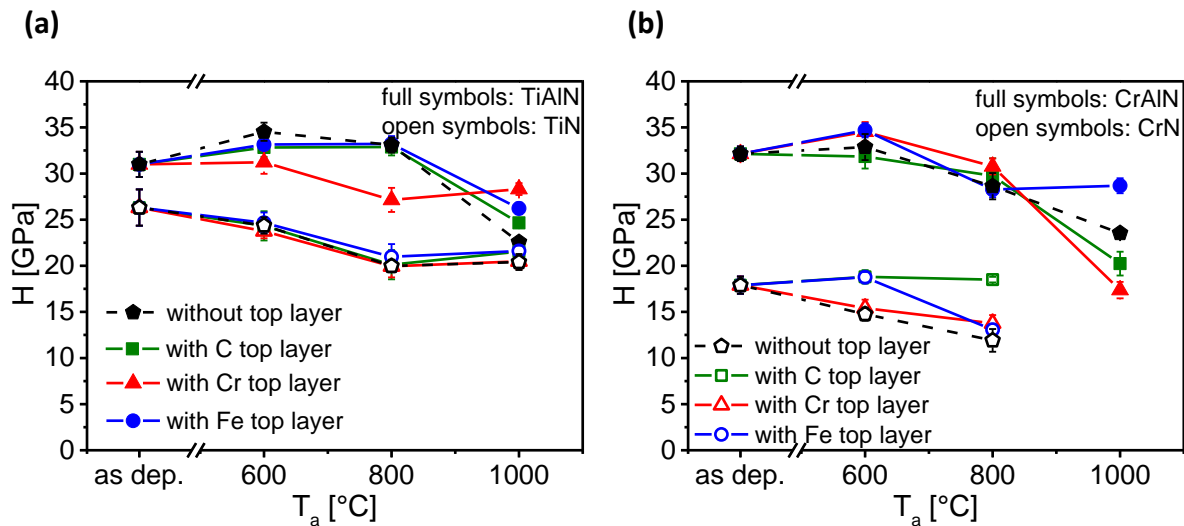
Fig. 6.3.6: Crystallite size evolution with increasing annealing temperature, T_a , of TiN, $\text{Ti}_{0.5}\text{Al}_{0.5}\text{N}$, CrN, and $\text{Cr}_{0.3}\text{Al}_{0.7}\text{N}$ coatings without top layer.

The crystallite size of TiN continuously increases from around 28 to 65 nm with increasing T_a to 1000 °C. The $\text{Ti}_{0.5}\text{Al}_{0.5}\text{N}$ coating on the other hand, exhibits a pronounced increase in crystallite size from around 12 to ~58 nm with increasing T_a to 600 °C, but then significantly decreases to 18 nm for $T_a = 800$ and 1000 °C. The increasing crystallite size for increasing T_a to 600 °C is based on recovery effects and was also observed by transmission electron microscopy studies by Hörling et al. [30]. For higher temperatures, the proceeding spinodal decomposition leads to a pronounced reduction in crystallite size, but also significant increase in microstrains [71]. For CrN, which exhibits the largest as deposited crystallite size of around 45 nm among the coatings studied, the grain size is already above 110 nm for $T_a = 800$ °C. The significant reduction in crystallite size to ~30 nm upon further increasing T_a to 1000 °C is mainly based on the massive dissociation of Cr–N bonds to transform to Cr under N_2 -release and the thereby connected phase formation of h- Cr_2N and c-Cr. Contrary, the $\text{Cr}_{0.3}\text{Al}_{0.7}\text{N}$ coatings still show very small crystallite sizes of around 18 nm even after annealing at 800 °C. With increasing T_a to 1000 °C, the crystallite size increases to 33 nm and the formation of w-AlN phases and the dissociation of Cr–N towards c-Cr under N_2 -release can already be detected. Here we need to mention, that in general, the crystallite size would increase with increasing temperature. Thereby, the overall fraction of crystal and grain boundaries decreases and hence also the energy stored by the boundaries. A pronounced increase in crystallite size with T_a is thus an indication of a small resistance against diffusion processes, which are essential for crystal growth. Any reduction in

crystallite size upon annealing indicates changes in the constitution of the phases, like decomposition and dissociation processes, leading to the precipitation of new phases. Consequently, simply comparing grain sizes with diffusion data will lead to wrong conclusions, if the grain size development and ongoing processes of microstructure and phase changes with temperature are not considered.

6.3.2 Hardness

In addition to the structural investigations, also the hardness development of our coatings upon annealing treatments without and with the individual top layers, C, Cr, and Fe, is studied. TiN coatings exhibit the highest hardness of 26.3 GPa in the as deposited state, see Fig. 6.3.7a. Due to relaxation of deposition induced defects and grain growth, as suggested by XRD, see Figs. 6.3.3 and 6.3.6, respectively, the hardness decreases to about 20 GPa with increasing annealing temperature. These relaxation effects are also responsible for the slightly reduced hardness at $T_a = 600$ °C with increasing annealing time to 1000 min. The small hardness increase for the TiN coatings with a C top layer when increasing T_a from 800 to 1000 °C, see Fig. 6.3.7a, suggests for solid solution hardening effects. This cannot be



observed for the TiN coating without a top layer or with Fe or Cr top layers.

Fig. 6.3.7: Hardness, H , evolution with increasing annealing temperature, T_a of (a) TiN and Ti_{0.5}Al_{0.5}N coatings and (b) CrN and Cr_{0.3}Al_{0.7}N coatings with C, Cr, and Fe top layers.

The $\text{Ti}_{0.5}\text{Al}_{0.5}\text{N}$ coatings show an as deposited hardness of ~ 31 GPa, which increases to about 34.5 GPa with increasing the annealing temperature to 600 °C due to the well-studied age hardening effect [79,115]. This is less pronounced (maximum hardness at ~ 33 GPa) and also retarded for the coating with a C or Fe top layer. The hardness even decreases to 27.3 GPa upon annealing to 800 °C, when using a Cr top layer, see Fig. 6.3.7a. However, for this coating with the Cr top layer, the hardness stays at a very high level of 28 GPa even upon annealing to 1000 °C, which is in contrast to the other top layer combinations or the native $\text{Ti}_{0.5}\text{Al}_{0.5}\text{N}$, where the hardness decreases with increasing T_a from 800 to 1000 °C. These data suggest that by the indiffusion of Cr to $\text{Ti}_{0.5}\text{Al}_{0.5}\text{N}$ the age hardening effect is less pronounced in hardness values, but the hardness can be stabilized at a high level for high annealing temperatures. A similar effect was observed by Forsen et al. [122], studying the thermal behavior of TiAlCrN arc evaporated coatings, which is based on the reduced coherency strains due to the incorporation of Cr.

CrN coatings exhibit an as deposited hardness of about 18 GPa which decreases to ~ 12 GPa with increasing the annealing temperature to 800 °C, see Fig. 6.3.7b. Corresponding to the studies of TiN coatings, this hardness reduction is based on relaxation of deposition-induced defects and grain growth processes, see Figs. 6.3.5 and 6.3.6, respectively. Unfortunately, the coatings partially delaminated upon annealing treatments upon 1000 °C, hence no reliable values could be obtained. This is valid also for CrN coatings with C, Cr, and Fe top layers. However, when using these top layers, the hardness slightly increases upon annealing to 600 and 800 °C. As this is against the trend observed for CrN coatings without top layers, solid solution hardening effects due to the additional indiffusion of elements need to be responsible. The highest hardness is obtained for the CrN coatings with C top layers and remains nearly constant at ~ 18 GPa over the entire temperature range. This might be related to the formation of Cr-C phases, as XRD peaks at $\sim 39.41^\circ$ and 44.16° can be associated to Cr_3C_2 and/or Cr_7C_3 phases, see Fig. 6.3.5a. For CrN coatings with Fe top layers, the hardness is still ~ 18 GPa even after annealing to 600 °C. In agreement with the studies with a C top layer, no phase change can be detected for this annealing temperature. Upon further annealing the hardness decreases to about 13 GPa. The coating with a Cr top layer exhibits a continuously decreasing hardness from ~ 18 to ~ 13 GPa with increasing T_a , which is very similar to the studies of CrN coatings without a top layer.

For $\text{Cr}_{0.3}\text{Al}_{0.7}\text{N}$ coatings a hardness of about 32 GPa is obtained in the as deposited state that slightly increases to 33 GPa due to annealing to 600 and 800 °C, see Fig. 7b. XRD investigations show the formation of w-AlN at these temperatures in agreement with earlier studies, which highlight that w-AlN precipitates are small and evenly distributed within the coating [53]. Further increasing the annealing temperatures causes the hardness to decrease to about 23.5 GPa. This is caused by the growth of the w-AlN precipitates and ongoing dissociation of Cr-N bonds to form Cr_2N under nitrogen loss. The hardness evolution with T_a of the $\text{Cr}_{0.3}\text{Al}_{0.7}\text{N}$ with a C top layer is very similar to the coating without a top layer, only that after annealing at 1000 °C, the hardness is even reduced to 20 GPa. The coatings with Cr or Fe top layers even experience a hardness increase to ~35 GPa upon annealing to 600 °C. But in contrast to the coating with a Cr top layer, which exhibits a pronounced hardness reduction upon further increasing T_a , the coating with an Fe top layer shows a very high hardness of ~29 GPa even after annealing at 1000 °C.

6.3.3 Diffusion coefficients

In order to determine the diffusion coefficients of the individual elements C, Cr, and Fe, EDX line-scans of the annealed and polished cross sections were performed. Basically, the diffusion length of the elements C, Cr, or Fe into the coating are obtained from the distance between the intersection of the Ti or Cr signal (from the coating) with the top layer signal and the point where the signal from the top layer (i.e. C, Cr, or Fe) reaches the background signal of the detector. To consider the excitation volume of the electron beam, this distance is measured in the as deposited state of the coatings with the individual top layers and used as reference x_r , see Fig. 6.3.8a. The corresponding distance of the annealed coatings is thus abbreviated by x_a , see Figs. 6.3.8b-d. Consequently, the effective diffusion length x is then derived by:

$$x = x_a - x_r. \quad (6.1)$$

From Fick's second law of diffusion, one possible solution of the medium diffusion distance within the time t relevant for the diffusion of an infinite source (not depleting) into a

material – with the boundary condition that the surface concentration of the diffusing element is way above the bulk concentration [119]– is:

$$x = 2\sqrt{Dt}, \quad (6.2)$$

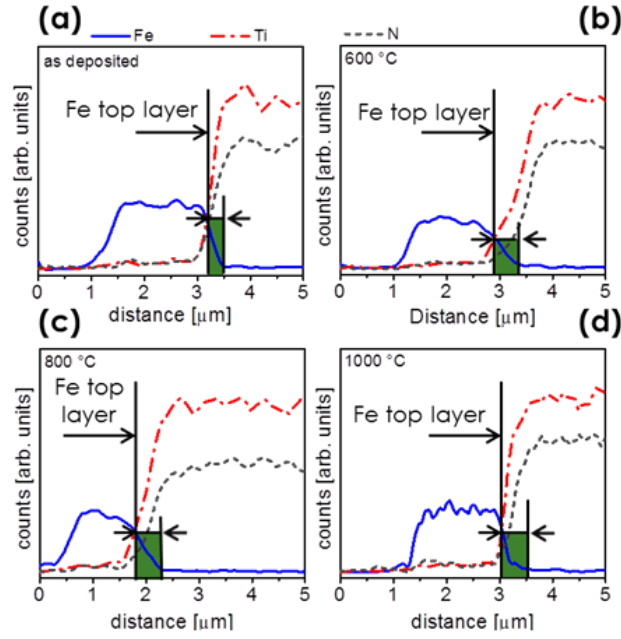


Fig. 6.3.8: EDX cross sectional line scans of TiN coatings with Fe top layers in the (a) as deposited state as well as after annealing to (b) 600, (c) 800, and (d) 1000 °C.

Thereby, the diffusion coefficients D of the individual elements into the individual coatings were calculated for the selected temperatures. In order to verify the results obtained from EDX line scans during SEM studies, selected samples were also investigated with EDX line scans during cross sectional TEM studies. The results obtained by SEM and TEM are in excellent agreement, hence we just present SEM EDX line scans. Representatively for the individual samples, SEM EDX line scans of TiN cross sections with Fe top layers are shown in the as deposited state in Fig. 6.3.8a, and after annealing at 600, 800, and 1000 °C in Figs. 6.3.8b, c, and d, respectively. With increasing annealing temperature, a clear increase of the diffusion length ($x = x_a - x_r$) is obtained. The thereby derived diffusion coefficients D – using Eq. 6.2 – are used to prepare Arrhenius plots for the individual elements and coatings. Figures 9a and b show the Arrhenius plots for C, Cr, and Fe diffusion into TiN and $\text{Ti}_{0.5}\text{Al}_{0.5}\text{N}$, respectively. From the intersection of the linear fits with the ordinate, the pre exponential

factors D_0 are obtained and the activation energies Q are derived from their slope, using the Arrhenius equation for the diffusion coefficient D [123]:

$$D = D_0 \exp^{-\frac{Q}{RT}}. \quad (6.3)$$

The Arrhenius plots for C and Fe diffusion into CrN and $\text{Cr}_{0.3}\text{Al}_{0.7}\text{N}$ coatings are given in Figs. 6.3.10a and b, respectively.

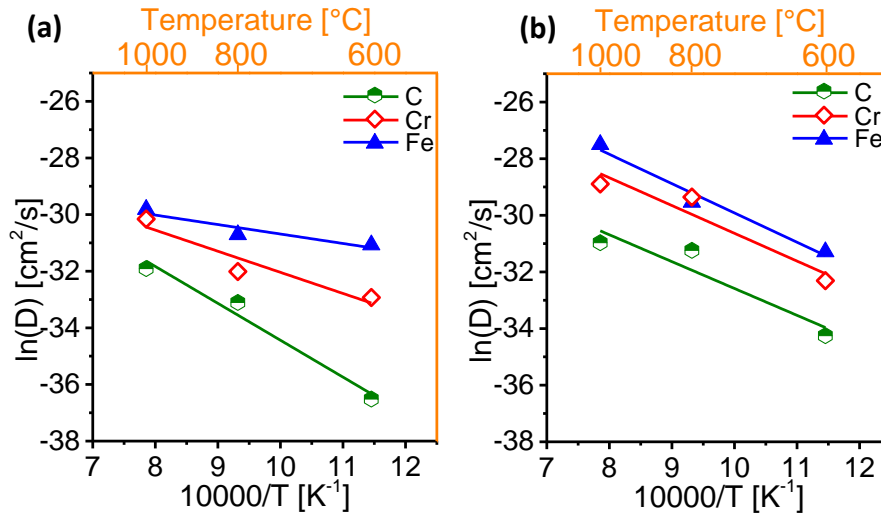


Fig. 6.3.9: Arrhenius plots for C, Cr, and Fe diffusion into (a) TiN and (b) $\text{Ti}_{0.5}\text{Al}_{0.5}\text{N}$ coatings.

The activation energies for the diffusion of C, Cr, and Fe, derived from the Arrhenius plots in Fig. 6.3.9, follow the order $Q_C > Q_{Cr} > Q_{Fe}$ and $Q_C \approx Q_{Cr} > Q_{Fe}$ within the coatings TiN and $\text{Ti}_{0.5}\text{Al}_{0.5}\text{N}$, respectively, see Table 1. Contrary, in CrN and $\text{Cr}_{0.3}\text{Al}_{0.7}\text{N}$ coatings the activation energy, derived from Fig. 6.3.10, for diffusion of Fe is higher as that of C. We envision that this is partly due to the weak Cr-N bonds, allowing for more Fe and N interactions. This is based on our observations that the Fe XRD peaks are slightly shifted towards lower 2θ diffraction angles with increasing annealing temperature suggesting for dissolved nitrogen within the Fe lattice. Table 1 also provides the pre exponential factor D_0 for diffusion of the individual elements and their medium diffusion distances x_{600} , x_{800} , and x_{1000} at 600, 800, and 1000 °C, respectively.

Especially the medium diffusion distances, which scale with the diffusion coefficients D according to Eq. 6.2, nicely show that TiN outperforms the other coatings as a “diffusion

barrier” against C and Cr for all temperatures studied. Against Fe diffusion, CrN provides only at 600 °C a better resistance and $\text{Cr}_{0.3}\text{Al}_{0.7}\text{N}$ even at 800 °C than TiN. However, already at 800 °C, the medium diffusion distance for Fe in TiN is nearly only half the distance in $\text{Ti}_{0.5}\text{Al}_{0.5}\text{N}$, and at 1000 °C, again TiN outperforms all other coatings studied.

The diffusion coefficients at 800 °C for C, Cr, and Fe into TiN are $0.42 \cdot 10^{-14}$, $1.3 \cdot 10^{-14}$, and $4.6 \cdot 10^{-14} \text{ cm}^2/\text{s}$. Thus, Fe shows highest diffusion coefficients and lowest activation energies, to be followed by Cr. Diffusion of Cr and Fe occurs mainly along grain boundaries, as reported in literature [45,76,119,120]. The lower diffusion coefficients for Cr as compared to Fe can be explained by the higher interaction of Cr with N, leading also to detectable formation of Cr_2N during annealing treatments, see for example the XRD pattern in Fig. 6.3.3. Although, the atomic radius of C is much smaller than Fe and Cr, C shows the lowest coefficient as well as the highest activation energy for diffusion among these three elements within our coatings. This can be understood by the even higher interaction of C with the coatings than observed for Cr.

The diffusion coefficients of Fe in TiN coatings at 600 °C is around $3.2 \cdot 10^{-14} \text{ cm}^2/\text{s}$ and is in good agreement with literature values of $3.0 \cdot 10^{-14}$ to $5.0 \cdot 10^{-14} \text{ cm}^2/\text{s}$, reported by Grigorov et al. [120]. The diffusion coefficients within $\text{Ti}_{0.5}\text{Al}_{0.5}\text{N}$ are 10 to 15 times larger as within TiN, especially above 600 °C. This can basically be explained by the different microstructure of the coatings. $\text{Ti}_{0.5}\text{Al}_{0.5}\text{N}$ coatings undergo decomposition processes upon annealing and thereby new interfaces are generated providing more diffusion pathways. TiN coatings do not undergo decomposition or phase changes in the temperature range studied. As the increase in diffusion coefficients, especially for Cr and Fe, with increasing temperature is way more pronounced in $\text{Ti}_{0.5}\text{Al}_{0.5}\text{N}$ than in TiN, not just the increased temperature is responsible, but the pronounced microstructural change within $\text{Ti}_{0.5}\text{Al}_{0.5}\text{N}$. This is also supported by XRD investigations, Fig. 6.3.4, and represented by the dependence of the crystal size with annealing temperature, see Fig. 6.3.6. When further increasing the annealing temperature from 800 to 1000 °C, significantly less structural changes occur, and hence also the increase in diffusion coefficient is less pronounced, see Fig. 6.3.9b and Table 1.

A corresponding behavior is obtained also for CrN, where the diffusion coefficient of Fe significantly changes when increasing the annealing temperature from 600 to 800 °C. This is based on the pronounced microstructural change of CrN to transform towards Cr₂N under nitrogen release [42]. Hence, more interfaces and diffusion pathways are provided. Contrary, the diffusion coefficient of C exhibits the pronounced increase at higher temperatures, when increasing T_a from 800 to 1000 °C, suggesting that the interaction of C with the coating material is higher as that of Fe. Due to the massive microstructural changes, the diffusion data points for C and Fe within CrN coatings deviate from the linear interpolation, see Fig. 6.3.10a.

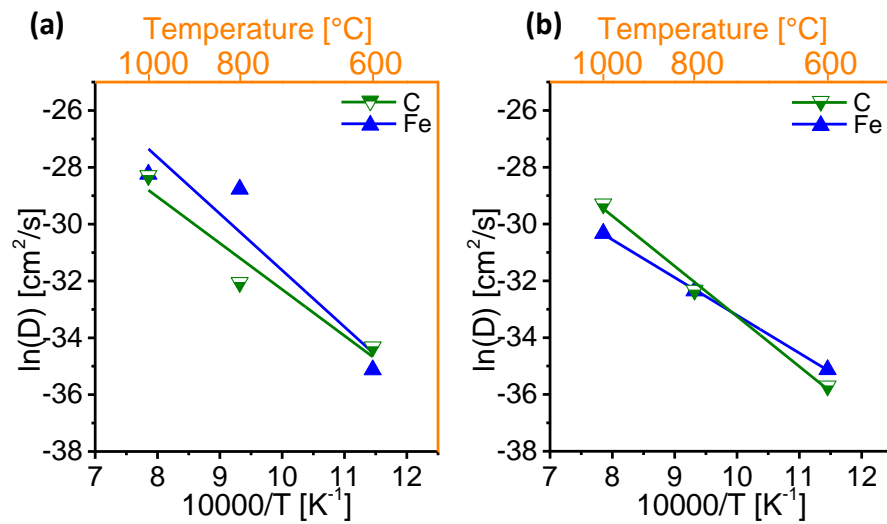


Fig. 6.3.10: Arrhenius plots for C, Cr, and Fe diffusion into (a) CrN and (b) Cr_{0.3}Al_{0.7}N coatings.

Consequently, diffusion coefficients for C, Cr, and Fe are higher in Ti_{0.5}Al_{0.5}N than in TiN coatings, which do not undergo decomposition or phase changes in the temperature range studied. Therefore, the diffusion coefficients of C, Cr, and Fe in Ti_{0.5}Al_{0.5}N coatings show a pronounced increase when increasing the temperature from 600 to 800 °C. As this increase is way more pronounced in Ti_{0.5}Al_{0.5}N than in TiN, not just the increased temperature is responsible, but a microstructural change within Ti_{0.5}Al_{0.5}N. This is also supported by XRD investigations, see Fig. 6.3.3. When further increasing the annealing temperature significantly less structural changes occur, and hence also the increase in diffusion coefficient is less pronounced, see Fig. 6.3.7b. Based on these results we suggest that the

more pronounced diffusion of C, Cr, and Fe into $\text{Ti}_{0.5}\text{Al}_{0.5}\text{N}$ will lead to an increased diffusion driven wear. This may in part explain the observations made by Ávila et al. [118] that TiN outperform $\text{Ti}_{1-x}\text{Al}_x\text{N}$ coatings with respect to a specific wear during machining.

The diffusion coefficients of C and Fe in CrN are $1.2 \cdot 10^{-14}$ and $32 \cdot 10^{-14} \text{ cm}^2/\text{s}$ at 800 °C. Consequently, also here the diffusion coefficient of Fe is higher, see Fig. 6.3.8a. Especially in CrN coatings the diffusion coefficient of Fe significantly changes when increasing the annealing temperature from 600 to 800 °C. This is based on the pronounced microstructural change of CrN to transform towards Cr_2N under nitrogen release [42]. Hence, more interfaces and diffusion pathways are provided. The diffusion coefficient of C increases nearly linear with temperature suggesting that the microstructural changes are less dominant than the temperature effect. This again supports our conclusion that the interaction of C with the coating materials is higher as that of Fe.

The diffusion coefficient of C in $\text{Cr}_{0.3}\text{Al}_{0.7}\text{N}$ at 600 °C is with $3.1 \cdot 10^{-16} \text{ cm}^2/\text{s}$ lower as that of Fe with $5.6 \cdot 10^{-16} \text{ cm}^2/\text{s}$, respectively. However, at 800 °C and especially at 1000 °C the diffusion coefficient of C is higher as that of Fe in $\text{Cr}_{0.3}\text{Al}_{0.7}\text{N}$. This may be explained by the increasing interaction of Fe with nitrogen, which is weakly bonded to Cr and therefore released at higher temperatures [42].

The activation energies for the diffusion of C, Cr, and Fe, derived from the Arrhenius plots follow the order $Q_C \geq Q_{\text{Cr}} > Q_{\text{Fe}}$ for diffusion in TiN, $\text{Ti}_{0.5}\text{Al}_{0.5}\text{N}$, and $\text{Cr}_{0.3}\text{Al}_{0.7}\text{N}$, respectively, see Table 1. Contrary, in CrN the activation energy for diffusion of Fe is higher as that of C. We envision that this is partly due to the weak Cr-N bonds, allowing for more Fe and N interactions. This is based on our observations that the Fe XRD peaks are slightly shifted towards lower 2θ diffraction angles with increasing annealing temperature suggesting for dissolved nitrogen within the Fe lattice. Table 1 also provides the pre exponential factor D_0 for diffusion of the individual elements and their medium diffusion distance x_{800} at 800 °C. As $\text{Cr}_{0.3}\text{Al}_{0.7}\text{N}$ is more stable against N_2 release than CrN, also the diffusion coefficients (or diffusion distances) within $\text{Cr}_{0.3}\text{Al}_{0.7}\text{N}$ do not increase that significantly with temperature as within CrN, see Fig. 6.3.10 and Table 1.

Table 1: Diffusion lengths at 600, 800, and 1000 °C x_{600} , x_{800} , and x_{1000} , respectively, and D_0 and Q values for C, Cr, and Fe diffusion in TiN, $Ti_{0.5}Al_{0.5}N$, CrN and $Cr_{0.3}Al_{0.7}N$ coatings.

	TiN			$Ti_{0.5}Al_{0.5}N$			CrN		$Cr_{0.3}Al_{0.7}N$	
	top layer			top layer			top layer		top layer	
	C	Cr	Fe	C	Cr	Fe	C	Fe	C	Fe
x_{600} [nm]	10	60	152	31	82	136	30	20	15	20
x_{800} [nm]	55	95	182	140	358	327	93	480	81	80
x_{1000} [nm]	100	240	200	160	451	450	610	625	370	220
D_0 [cm ² /s]	505	21	0.19	93.2	903	64.1	1.13	82	1.73	0.02
	$\cdot 10^{-12}$	$\cdot 10^{-12}$	$\cdot 10^{-12}$	$\cdot 10^{-12}$	$\cdot 10^{-12}$	$\cdot 10^{-12}$	$\cdot 10^{-7}$	$\cdot 10^{-7}$	$\cdot 10^{-7}$	$\cdot 10^{-7}$
Q [kJ/mol]	108.4	62	12.8	78.9	81.6	56.1	135.5	165	110	147

6.4 Summary and Conclusion

We use C, Cr, and Fe top layers on arc evaporated TiN, $Ti_{0.5}Al_{0.5}N$, CrN, and $Cr_{0.3}Al_{0.7}N$ hard coatings to study their diffusion behavior during vacuum annealing up to 1000 °C. Our results clearly show that the hardness evolution with annealing temperature and time of TiN coatings is nearly unaffected by the diffusion of C, Cr, and Fe. Independent of the top layer the hardness decreases from 26.3 GPa in the as deposited state to about 21 GPa after annealing to 1000 °C, due to grain growth processes and recovery of deposition induced structural defects. For $Ti_{0.5}Al_{0.5}N$ coatings the hardness increase – originating from age hardening effects – is not significantly influenced when a C or Fe top layer is present during our annealing treatments. Contrary, as soon as Cr diffuses into $Ti_{0.5}Al_{0.5}N$, the generally observed hardness increase is reduced. After annealing at 800 °C, the hardness is with ~27.5 GPa even lower as in the as deposited state with 31 GPa. Nevertheless, when Cr is present, the hardness remains at around 27.5 GPa even when annealed to 1000 °C. This is in contrast

to the $\text{Ti}_{0.5}\text{Al}_{0.5}\text{N}$ coating without a top layer or with C and Fe top layers where the hardness is between 22 and 26 GPa for $T_a = 1000^\circ\text{C}$. Consequently, Cr can effectively retard the decomposition process of $\text{Ti}_{0.5}\text{Al}_{0.5}\text{N}$, allowing also for high hardness values at high temperatures.

The hardness of CrN coatings without a top layer as well as with Cr and Fe top layers continuously decreases with increasing annealing temperature, due to ongoing CrN dissociation towards c-Cr and N_2 . However, with a C top layer the hardness stays at the very high level of 18 GPa even for $T_a = 800^\circ\text{C}$. Our data suggest that the formation of Cr-C bonds is responsible for this behavior. For $\text{Cr}_{0.3}\text{Al}_{0.7}\text{N}$ coatings a slight increase in hardness from the as deposited value of ~ 32 GPa is observed when increasing the annealing temperature to 600°C . However, upon further increasing the annealing temperature, the hardness decreases independent of the top layer. Especially the coatings without a top layer and with a C or Cr top layer exhibit a comparable behavior. But the $\text{Cr}_{0.3}\text{Al}_{0.7}\text{N}$ coating with an Fe top layer exhibits still a high hardness of 29 GPa even after annealing at 1000°C .

The diffusion of C, Cr, and Fe is significantly different in TiN, $\text{Ti}_{0.5}\text{Al}_{0.5}\text{N}$, CrN, and $\text{Cr}_{0.3}\text{Al}_{0.7}\text{N}$ coatings. For example, their diffusion coefficients are 5 to 15 times higher within $\text{Ti}_{0.5}\text{Al}_{0.5}\text{N}$ than in TiN coatings but up to 30 times higher in CrN than in $\text{Cr}_{0.3}\text{Al}_{0.7}\text{N}$ coatings. These differences are especially valid for temperatures above 600°C , where $\text{Ti}_{1-x}\text{Al}_x\text{N}$ and CrN coatings undergo pronounced microstructural changes. We envision that the different diffusion activities have not only a significant influence on microstructure and mechanical properties, but also on the wear behavior of such protective coatings. Consequently, especially diffusion driven wear can be higher for $\text{Ti}_{0.5}\text{Al}_{0.5}\text{N}$ than for TiN coatings and higher for CrN than for $\text{Cr}_{0.3}\text{Al}_{0.7}\text{N}$ coatings.

Summary and Contribution to the field

This extensive study of $\text{Al}_x\text{Cr}_{1-x}\text{N}$ coatings provides a deep insight of how the target material, deposition process, deposition parameters, and coating architecture influence properties of the synthesized coatings. Moreover, it shows how properties of CrN- and TiN based coatings are affected by diffusion of C, Cr, and Fe and gives a comprehensive collection of the related diffusion data.

Usually, $\text{Al}_x\text{Cr}_{1-x}\text{N}$ coatings are deposited by reactive physical vapor deposition processes, where targets prepared from Al and Cr powder are used. However, there is also the possibility of using intermetallic, here Al_8Cr_5 , or even ceramic AlN/CrN_x target materials, where a significant amount of the energy is also transferred to the N atoms. Hence, we studied reactively sputtered coatings from powder metallurgically prepared metallic $\text{Al}_{0.7}\text{Cr}_{0.3}$, intermetallic Al_8Cr_5 , and ceramic AlN/CrN_x targets. The ceramic target was also subject to non-reactive sputtering in pure Ar atmosphere. The coatings reactively sputtered from the metallic and intermetallic target show a similar pronounced columnar structure and hardness values of ~ 12 and 13 GPa. Using the ceramic target, however results in a denser, fine fibrous coating morphology and therefore also in a higher hardness of ~ 16.5 GPa. The non-reactively sputtered coatings using the ceramic target are of an extremely nano-crystalline nature and thus, even a hardness of ~ 25 GPa is obtained. Further on, thermal analyses of the $\text{Al}_x\text{Cr}_{1-x}\text{N}$ coatings clearly show that the endothermic reactions due to Cr-N dissociations are shifted to higher temperatures when using the ceramic target. Based on these results we can conclude that by varying the target design for a given chemical composition, coatings (e.g., denser morphology, higher hardness) and deposition (e.g., higher deposition rate) can further be improved.

However, also the AlN content within $\text{Al}_x\text{Cr}_{1-x}\text{N}$ coatings significantly influences the coating properties. Further on, the film properties can be improved by multilayer architectures and additionally, can be modified by varying the bias potential applied to the substrate materials. Therefore, we increased the AlN content by depositing multilayered coatings composed of

alternating high Al containing layers ($\text{Al}_{0.85}\text{Cr}_{0.15}\text{N}$ or $\text{Al}_{0.9}\text{Cr}_{0.1}\text{N}$) and low Al containing layers ($\text{Al}_{0.7}\text{Cr}_{0.3}\text{N}$ or $\text{Al}_{0.75}\text{Cr}_{0.25}\text{N}$). The impact of bias potential as well as multilayer arrangement on structure, mechanical properties, and thermal stability of $\text{Al}_x\text{Cr}_{1-x}\text{N}$ coatings is studied. The monolithically grown $\text{Al}_{0.7}\text{Cr}_{0.3}\text{N}$ and $\text{Al}_{0.75}\text{Cr}_{0.25}\text{N}$ coatings exhibit a single phase cubic structure and increasing hardness from 33 to 38 GPa or 31 to 36 GPa, respectively, with increasing bias potential from -40 to -80 V. Higher Al containing $\text{Al}_{0.85}\text{Cr}_{0.15}\text{N}$ and $\text{Al}_{0.9}\text{Cr}_{0.1}\text{N}$ coatings show either a single phase wurtzite ($U_b = -40$ V) or mixed-phase cubic-wurtzite ($U_b \geq -80$ V) structure with hardnesses of around 19 or 27 GPa, respectively. Combining the lower Al-containing $\text{Al}_{0.7}\text{Cr}_{0.3}\text{N}$ and $\text{Al}_{0.75}\text{Cr}_{0.25}\text{N}$ layers with higher Al-containing $\text{Al}_{0.85}\text{Cr}_{0.15}\text{N}$ layers however, leads to predominant cubic structured coatings for bias potentials $U_b \geq -100$ V. This is related to the combined effect of coherency strains and suppressed growth of the less dense hexagonal phase at intense ion bombardment. The hardness of these multilayered coatings can thus be increased to 33 and 37 GPa, respectively. Thermal analysis revealed that especially the $\text{Al}_{0.75}\text{Cr}_{0.25}\text{N}/\text{Al}_{0.9}\text{Cr}_{0.1}\text{N}$ multilayers prepared with -120 V, with high hardness values around 30 ± 3 GPa over the entire temperature range up to 1100 °C, show superior thermal stability combined with excellent mechanical properties. This is based on the beneficial effect of the bias potential to prepare dense coatings, especially when they are composed of multiple phases, and the specific arrangement of $\text{Al}_{0.75}\text{Cr}_{0.25}\text{N}$ and $\text{Al}_{0.9}\text{Cr}_{0.1}\text{N}$ layers with a bilayer period of ~ 38 nm.

For diffusion studies thin layers of C, Cr, and Fe – which are common transfer-elements during machining – were deposited on arc evaporated TiN, $\text{Ti}_{0.5}\text{Al}_{0.5}\text{N}$, CrN, and $\text{Cr}_{0.3}\text{Al}_{0.7}\text{N}$ coatings. The diffusion processes within these coatings are significantly determined by their microstructural changes upon annealing, especially by the phase decomposition of the supersaturated $\text{Ti}_{1-x}\text{Al}_x\text{N}$ phases towards the stable constituents cubic TiN and hexagonal wurtzite-type AlN. This is in contrast to TiN coatings, where no phase decomposition takes place, and the fraction of structural built-in defects generally decreases upon annealing. Consequently, the diffusion of C, Cr, and Fe is more within $\text{Ti}_{0.5}\text{Al}_{0.5}\text{N}$ than in TiN, especially at elevated temperatures where the supersaturated $\text{Ti}_{1-x}\text{Al}_x\text{N}$ phase decomposes. The dissociation of Cr-N bonds towards Cr under nitrogen release within CrN based coatings is postponed to higher temperatures by the addition of Al. Therefore, the diffusion of C, Cr, and Fe is less pronounced within $\text{Cr}_{0.3}\text{Al}_{0.7}\text{N}$ than in CrN, especially at temperatures where

CrN already dissociates. Our results show that the diffusion of C, Cr, and Fe is significantly different in TiN, $\text{Ti}_{0.5}\text{Al}_{0.5}\text{N}$, CrN, and $\text{Cr}_{0.3}\text{Al}_{0.7}\text{N}$ coatings. For example, their diffusion coefficients are 5 to 15 times higher within $\text{Ti}_{0.5}\text{Al}_{0.5}\text{N}$ than in TiN coatings but up to 30 times higher in CrN than in $\text{Cr}_{0.3}\text{Al}_{0.7}\text{N}$ coatings. We envision that the different diffusion activities have not only a significant influence on microstructure and mechanical properties, but also on the wear behavior of such protective coatings. Consequently, especially diffusion driven wear can be higher for $\text{Ti}_{0.5}\text{Al}_{0.5}\text{N}$ than for TiN coatings and higher for CrN than for $\text{Cr}_{0.3}\text{Al}_{0.7}\text{N}$ coatings.

Acknowledgment for financial and experimental support

First of all the financial support by the Austrian Federal Ministry of Economy, Family and Youth and the National Foundation for Research, Technology and Development, which is the basis for Christian Doppler Laboratories is gratefully acknowledged. Gratitude is also owed to industrial partners Plansee Composite Materials GmbH and Oerlikon Balzers Coating AG.

SEM and XRD measurements were carried out using facilities at the University Service Centre for Transmission Electron Microscopy, (USTEM) and the X-ray center (XRC) of the Vienna University of Technology, Vienna.

This work has also been supported by the European Community as an Integrating Activity 'Support of Public and Industrial Research Using Ion Beam Technology (SPIRIT)' under EC contract no. 227012.

References

- [1] I. Petrov, J. Vac. Sci. Technol., A 10 (1992) 265–272.
- [2] S. Zhang, W. Zhu, J. Mater. Process. Technol. 39 (1993) 165–177.
- [3] H.C. Barshilia, N. Selvakumar, B. Deepthi, K.S. Rajam, Surf. Coat. Technol. 201 (2006) 2193–2201.
- [4] P.H. Mayrhofer, G. Tischler, C. Mitterer, Surf. Coat. Technol. 142–144 (2001) 78–84.
- [5] W.-D. Münz, J. Vac. Sci. Technol., A 4 (1986) 2717–2725.
- [6] O. Knotek, F. Löffler, H.-J. Scholl, Surf. Coat. Technol. 45 (1991) 53–58.
- [7] O. Knotek, J. Vac. Sci. Technol., A 4 (1986) 2695–2700.
- [8] Y. Makino, Surf. Coat. Technol. 193 (2005) 185–191.
- [9] M. Zhou, Y. Makino, M. Nose, K. Nogi, Thin Solid Films 339 (1999) 203–208.
- [10] Y. Makino, K. Nogi, Surf. Coat. Technol. 98 (1998) 1008–1012.
- [11] A. Sugishima, H. Kajioka, Y. Makino, Surf. Coat. Technol. 97 (1997) 590–594.
- [12] J.A. Thornton, J. Vac. Sci. Technol., 12 (1975) 830–835.
- [13] M. Pfeiler, K. Kutschej, M. Penoy, C. Michotte, C. Mitterer, M. Kathrein, Surf. Coat. Technol. 202 (2007) 1050–1054.
- [14] P.H. Mayrhofer, M. Geier, C. Löcker, L. Chen, Int. J. Mat. Res. 100 (2009) 1052–1058.
- [15] W.D. Sproul, D.J. Christie, D.C. Carter, Thin Solid Films 491 (2005) 1–17.
- [16] H. Holleck, M. Lahres, P. Woll, Surf. Coat. Technol. 41 (1990) 179–190.
- [17] H. Holleck, V. Schier, Surf. Coat. Technol. 76–77 (1995) 328–336.
- [18] L. Chen, Y. Du, F. Yin, J. Li, Int. J. Refract. Met. Hard Mater. 25 (2007) 72–76.
- [19] J.-K. Park, Y.-J. Baik, Surf. Coat. Technol. 200 (2005) 1519–1523.

- [20] J. Lin, J.J. Moore, B. Mishra, M. Pinkas, W.D. Sproul, *Surf. Coat. Technol.* 204 (2009) 936–940.
- [21] J. Lin, J.J. Moore, B. Mishra, M. Pinkas, X. Zhang, W.D. Sproul, *Thin Solid Films* 517 (2009) 5798–5804.
- [22] N.A. Abukhshim, P.T. Mativenga, M. a. Sheikh, *Int. J. Mach. Tool. Manu.* 46 (2006) 782–800.
- [23] W.D. Westwood, *Sputter Deposition*, 2003.
- [24] P.M. Martin, *Handbook of Deposition Technologies for Films and Coatings*, 2010.
- [25] M. Ohring, *Material Science of Thin Films*, 2002.
- [26] C.M. Koller, *Thermal Stability and Oxidation Resistance Of Ti-Al-N/Ta-Al-N Multilayer Coatings*, Montanuniversität Leoben, 2012.
- [27] A. Anders, *Cathodic Arcs*, Springer New York, New York, NY, 2008.
- [28] U. Helmersson, M. Lattemann, J. Bohlmark, A.P. Ehasarian, J.T. Gudmundsson, *Thin Solid Films* 513 (2006) 1–24.
- [29] R.L. Boxman, S. Goldsmith, *Surface and Coatings Technology* 52 (1992) 39–50.
- [30] A. Hörling, L. Hultman, M. Odén, J. Sjölen, L. Karlsson, *J. Vac. Sci. Technol., A* 20 (2002) 1815.
- [31] P.. Barna, M. Adamik, *Thin Solid Films* 317 (1998) 27–33.
- [32] R. Messier, *J. Vac. Sci. Technol., A* 2 (1984) 500–503.
- [33] A. Anders, *Thin Solid Films* 518 (2010) 4087–4090.
- [34] S. Vepřek, *J. Vac. Sci. Technol., A* 17 (1999) 2401–2420.
- [35] M. Stüber, S. Ulrich, H. Leiste, H. Holleck, *Surf. Coat. Technol.* 206 (2011) 610–616.
- [36] J. Dunlop, *J. Vac. Sci. Technol., A* 10 (1992) 305–312.
- [37] P.. Mayrhofer, F. Kunc, J. Musil, C. Mitterer, *Thin Solid Films* 415 (2002) 151–159.
- [38] J. Vetter, *77* (1995) 719–724.
- [39] B. Navinšek, P. Panjan, I. Milošev, *Surf. Coat. Technol.* 97 (1997) 182–191.
- [40] H.C. Barshilia, N. Selvakumar, B. Deepthi, K.S. Rajam, *Surf. Coat. Technol.* 201 (2006) 2193–2201.

- [41] F. Lévy, P. Hones, P.E. Schmid, R. Sanjinés, M. Diserens, C. Wiemer, *Surf. Coat. Technol.* 120-121 (1999) 284–290.
- [42] P.H. Mayrhofer, F. Rovere, M. Moser, C. Strondl, R. Tietema, *Scripta Mater.* 57 (2007) 249–252.
- [43] D.S. Stone, *J. Vac. Sci. Technol., A* 9 (1991) 2543–2547.
- [44] J.H. Quateman, S. Sisak, *J. Appl. Phys.* 62 (1987) 2479–2481.
- [45] W.B. Nowak, R. Keukelaar, W. Wang, A.R. Nyaiesh, *J. Vac. Sci. Technol., A* 3 (1985) 2242–2245.
- [46] Y.C. Chim, X.Z. Ding, X.T. Zeng, S. Zhang, *Thin Solid Films* 517 (2009) 4845–4849.
- [47] H. Holleck, *Surf. Coat. Technol.* 36 (1988) 151–159.
- [48] P.H. Mayrhofer, D. Music, T. Reeswinkel, H.-G. Fuß, J.M. Schneider, *Acta Mater.* 56 (2008) 2469–2475.
- [49] H. Willmann, P.H. Mayrhofer, P.O.Å. Persson, A.E. Reiter, L. Hultman, C. Mitterer, *Scripta Mater.* 54 (2006) 1847–1851.
- [50] A.E. Reiter, V.H. Derflinger, B. Hanselmann, T. Bachmann, B. Sartory, *Surf. Coat. Technol.* 200 (2005) 2114–2122.
- [51] A.E. Reiter, C. Mitterer, B. Sartory, *J. Vac. Sci. Technol., A* 25 (2007) 711–720.
- [52] F. Rovere, *Theoretical and Experimental Assessment of Cr-Al-Y-N as Protective Coating for -TiAl Based Alloys*, Rheinisch-Westfälische Technische Hochschule Aachen, 2010.
- [53] H. Willmann, P.H. Mayrhofer, L. Hultman, C. Mitterer, *J. Mater. Res.* 23 (2008) 2880–2885.
- [54] P.H. Mayrhofer, A. Hörling, L. Karlsson, J. Sjöln, T. Larsson, C. Mitterer, L. Hultman, *Appl. Phys. Lett.* 83 (2003) 2049–2051.
- [55] D. McIntyre, J.E. Greene, G. Håkansson, J.-E. Sundgren, W.-D. Münz, *J. Appl. Phys.* 67 (1990) 1542–1553.
- [56] H. Holleck, H. Schulz, *Surf. Coat. Technol.* 36 (1988) 707–714.
- [57] M. Larsson, M. Bromark, P. Hedenqvist, S. Hogmark, *Surf. Coat. Technol.* 76-77 (1995) 202–205.
- [58] M. Čekada, P. Panjan, *Vacuum* 61 (2001) 235–240.
- [59] S. PalDey, S.. Deevi, *Mater. Sci. Eng., A* 342 (2003) 58–79.

- [60] H.C. Barshilia, B. Deepthi, N. Selvakumar, A. Jain, K.S. Rajam, *Appl. Surf. Sci.* 253 (2007) 5076–5083.
- [61] M. Schlögl, B. Mayer, J. Paulitsch, P.H. Mayrhofer, *Thin Solid Films* 545 (2013) 375–379.
- [62] M. Bartosik, R. Daniel, C. Mitterer, I. Matko, M. Burghammer, P.H. Mayrhofer, J. Keckes, *Thin Solid Films* 542 (2013) 1–4.
- [63] E. Martínez, J. Romero, A. Lousa, J. Esteve, *J. Phys. D: Appl. Phys.* 35 (2002) 1880–1883.
- [64] G.S. Kim, S.Y. Lee, J.H. Hahn, *Surf. Coat. Technol.* 171 (2002) 91–95.
- [65] V. Chawla, D. Holec, P.H. Mayrhofer, *J. Phys. D: Appl. Phys.* 46 (2013) 045305.
- [66] J. Lin, B. Mishra, J.J. Moore, W.D. Sproul, *Surf. Coat. Technol.* 202 (2008) 3272–3283.
- [67] F. Rovere, P.H. Mayrhofer, A. Reinholdt, J. Mayer, J.M. Schneider, *Surf. Coat. Technol.* 202 (2008) 5870–5875.
- [68] M.Y.S. D.A. Porter, K.E. Easterling, *Phase Transformations in Metals and Alloys*, 3rd ed., 2009.
- [69] P.H. Mayrhofer, D. Music, J.M. Schneider, *Appl. Phys. Lett.* 88 (2006) 071922.
- [70] P.H. Mayrhofer, H. Willmann, A.E. Reiter, *Surf. Coat. Technol.* 202 (2008) 4935–4938.
- [71] R. Rachbauer, E. Stergar, S. Massl, M. Moser, P.H. Mayrhofer, *Scripta Mater.* 61 (2009) 725–728.
- [72] G. Gottstein, *Physikalische Grundlagen Der Metallkunde*, Springer, Berlin, 2001.
- [73] W.D. Callister, D.G. Rethwisch, *Materialwissenschaften Und Werkstofftechnik*, 1st ed., Wiley-VCH Verlag & Co., 2013.
- [74] P.H. Mayrhofer, *Werkstoffkunde Metallischer Werkstoffe*, Technische Universität Wien, 2013.
- [75] H. Mehrer, *Diffusion in Solids*, Springer, New York, 2007.
- [76] M.B. Chamberlain, *Thin Solid Films* 91 (1982) 155–162.
- [77] H. Wang, A. Tiwari, X. Zhang, A. Kvit, J. Narayan, *Appl. Phys. Lett.* 81 (2002) 1453–1455.
- [78] J.S. Reid, X. Sun, E. Kolawa, M. -a. Nicolet, *IEEE Electr. Device. L.* 15 (1994) 298–300.

- [79] L. Hultman, *Vacuum* 57 (2000) 1–30.
- [80] M. Birkholz, *Thin Film Analysis by X-Ray Scattering*, Wiley-VCH Verlag & Co., Weinheim, 2006.
- [81] M. von Heimendahl, *Einführung in Die Elektronenmikroskopie*, Vieweg Verlag, Braunschweig, 1970.
- [82] W.C. Oliver, G.M. Pharr, *J. Mater. Res.* 7 (1992) 1564–1583.
- [83] L.B. Freund, S. Suresh, *Thin Film Materials*, Cambridge University Press, Cambridge, 2003.
- [84] M.E. Brown, *Handbook of Thermal Analysis and Calorimetry: Volume 1*, Elsevier B.V., Amsterdam, 1998.
- [85] S. Hofmann, H.A. Jehn, *Mater. Corros.* 41 (1990) 756–760.
- [86] J. Vetter, E. Lugscheider, S.S. Guerreiro, *Surf. Coat. Technol.* 98 (1998) 1233–1239.
- [87] M. Kawate, A. Kimura, T. Suzuki, *J. Vac. Sci. Technol., A* 20 (2002) 569–571.
- [88] J.C. Sánchez-López, D. Martínez-Martínez, C. López-Cartes, A. Fernández, M. Brizuela, A. García-Luis, J.I. Oñate, *J. Vac. Sci. Technol., A* 23 (2005) 681–686.
- [89] W. Ensinger, *Surf. Coat. Technol.* 99 (1998) 1–13.
- [90] I. Petrov, P.B. Barna, L. Hultman, J.E. Greene, *J. Vac. Sci. Technol., A* 21 (2003) 117–128.
- [91] J. Paulitsch, M. Schenkel, T. Zufraß, P.H. Mayrhofer, W.-D. Münz, *Thin Solid Films* 518 (2010) 5558–5564.
- [92] R. Daniel, K.J. Martinschitz, J. Keckes, C. Mitterer, *J. Phys. D: Appl. Phys.* 42 (2009) 1–13.
- [93] C.-S. Shin, D. Gall, Y.-W. Kim, N. Hellgren, I. Petrov, J.E. Greene, *J. Appl. Phys.* 92 (2002) 5084–5093.
- [94] P.H. Mayrhofer, D. Music, J.M. Schneider, *J. Appl. Phys.* 100 (2006) 094906.
- [95] P.H. Mayrhofer, C. Mitterer, *Recent Res. Devel. Vacuum Sci. & Tech.* 4 (2003) 71–97.
- [96] I. Petrov, P.B. Barna, L. Hultman, J.E. Greene, *J. Vac. Sci. Technol., A* 21 (2003) 117–128.
- [97] J. Paulitsch, P.H. Mayrhofer, W.-D. Münz, M. Schenkel, *Thin Solid Films* 517 (2008) 1239–1244.

- [98] M.S. J. Paulitsch, P. Mayrhofer, W.-D. Münz, Annual Technical Conference Proceedings of the Society of Vacuum Coaters (2007) 150.
- [99] J.L. Mo, M.H. Zhu, A. Leyland, A. Matthews, Surf. Coat. Technol. 215 (2013) 170–177.
- [100] J.L. Mo, M.H. Zhu, Wear 267 (2009) 874–881.
- [101] M. Kawate, A. Kimura Hashimoto, T. Suzuki, Surf. Coat. Technol. 165 (2003) 163–167.
- [102] P. Li, L. Chen, S.Q. Wang, B. Yang, Y. Du, J. Li, M.J. Wu, Int. J. Refract. Met. Hard Mater. 40 (2013) 51–57.
- [103] Q. Kong, L. Ji, H. Li, X. Liu, Y. Wang, J. Chen, H. Zhou, Mater. Sci. Eng., B 176 (2011) 850–854.
- [104] C. Wüstefeld, D. Rafaja, V. Klemm, C. Michotte, M. Kathrein, Surf. Coat. Technol. 205 (2010) 1345–1349.
- [105] Y.X. Wang, S. Zhang, J.-W. Lee, W.S. Lew, B. Li, Surf. Coat. Technol. 206 (2012) 5103–5107.
- [106] M. Odén, C. Ericsson, G. Håkansson, H. Ljungcrantz, Surf. Coat. Technol. 114 (1999) 39–51.
- [107] Q. Xia, H. Xia, A.L. Ruoff, J. Appl. Phys. 73 (1993) 8198–8200.
- [108] F. Rovere, P.H. Mayrhofer, J. Vac. Sci. Technol., A 26 (2008) 29–35.
- [109] M. Schlögl, J. Paulitsch, P.H. Mayrhofer, Surf. Coat. Technol. 240 (2014) 250–254.
- [110] B. Alling, L. Hultberg, L. Hultman, I.A. Abrikosov, Appl. Phys. Lett. 102 (2013) 031910.
- [111] C. Sabitzer, J. Paulitsch, S. Kolozsvári, R. Rachbauer, P.H. Mayrhofer, Vacuum 106 (2014) 49–52.
- [112] (n.d.).
- [113] P.H. Mayrhofer, C. Mitterer, L. Hultman, H. Clemens, Progress in Materials Science 51 (2006) 1032–1114.
- [114] N. Bagcivan, K. Bobzin, S. TheiB, Thin Solid Films 528 (2013) 180–186.
- [115] I. a. Abrikosov, A. Knutsson, B. Alling, F. Tasnádi, H. Lind, L. Hultman, M. Odén, Materials 4 (2011) 1599–1618.
- [116] L. Aihua, D. Jianxin, C. Haibing, C. Yangyang, Z. Jun, Int. J. Refract. Met. Hard Mater. 31 (2012) 82–88.

- [117] W.-D. Münz, *Journal of Vacuum Science & Technology A: Vacuum, Surfaces, and Films* 4 (1986) 2717.
- [118] R.F. Ávila, R.D. Mancosu, a. R. Machado, S.D. Vecchio, R.B. da Silva, J.M. Vieira, *Wear* 302 (2013) 1192–1200.
- [119] H. Wang, A. Tiwari, X. Zhang, a. Kvit, J. Narayan, *Applied Physics Letters* 81 (2002) 1453.
- [120] G.I. Grigorov, K.G. Grigorov, M. Stojanova, J.L. Vignes, J.P. Langeron, P. Denjean, L. Ranno, *Phys. C.* 241 (1995) 397–400.
- [121] I.G. Polyakova, T. Hübert, *Surf. Coat. Technol.* 141 (2001) 55–61.
- [122] R. Forsén, M. Johansson, M. Odén, N. Ghafoor, *J. Vac. Sci. Technol., A* 30 (2012) 061506.
- [123] J.C. Fisher, *J. Appl. Phys.* 22 (1951) 74.

PUBLICATIONS

Publications included in the thesis

C. Sabitzer, J. Paulitsch, S. Kolozsvári, R. Rachbauer, P. H. Mayrhofer, *Influence of bias potential and layer arrangement on structure and mechanical properties of arc evaporated Al–Cr–N coatings*, Vacuum 106 (2014) 49–52.

C. Sabitzer, S. Kolozsvári, M. Arndt, R. Rachbauer, J. Paulitsch, P. H. Mayrhofer; *Reactive and non-reactive sputter deposition of Al-Cr-N Coatings Using Metallic, Intermetallic, and Ceramic Targets*, Proceedings of the 18th Plansee Seminar 2013 (2013) 1998 - 2005.

C. Sabitzer, J. Paulitsch, S. Kolozsvári, R. Rachbauer, P. H. Mayrhofer, *Influence of bias potential and layer arrangement on thermal stability of arc evaporated Al-Cr-N coatings*, to be submitted to Surface and Coatings Technology

C. Sabitzer, C. Steinkellner, C.M. Koller, S. Kolozsvári, R. Rachbauer, P. H. Mayrhofer, *Diffusion behavior of C, Cr, and Fe in arc evaporated TiN- and CrN-based coatings and their influence on thermal stability and hardness*, in final preparation

Publications not included in the thesis

S. Gangopadhyay, N. Schalk, , T. Weirather, , C. Sabitzer, S. Hirn, V.L. Terziyska, C. Czettl, P. Polcik, M. Kathrein, C.Mitterer, *Combinatorial synthesis of $Cr_{1-x}Al_xN$ and $Ta_{1-x}Al_xN$ hard coatings using industrial-scale co-sputtering from segmented targets*

C.M. Koller, R. Hollerweger, C. Sabitzer, R. Rachbauer, P. Polcik, J. Paulitsch, P.H. Mayrhofer, *Thermal stability and oxidation resistance of arc evaporated TiAlN, TaAlN, TiAlTaN, and TiAlN/TaAlN coatings*, Surface and Coating Technology, in Press

RESUME

Personal Informations

Date of birth: May 7th, 1987
Place of birth: Klagenfurt, Austria
Private Address: Launsdorf 2, 9314 Launsdorf, Austria
Nationality: Austria

Education

Dec. 2012 – present	PhD in Material Science – “Influence of Target composition and phases on arc evaporated AlCrN and AlCrO coatings” CDL AOS, Institute of Materials Science and Technology, Vienna University of Technology
Jan. 2012 – Nov. 2012	PhD in Material Science – “Influence of Target composition and phases on arc evaporated AlCrN and AlCrO coatings” CDL AOS, Department Physical Metallurgy and Materials Testing, Montanuniversität Leoben
Sep. 2005 – Dez. 2011	Graduated study program – Material Science Montanuniversität Leoben (diploma examination June 2012) Specialised on metallic materials and nanostructured thin films (academic title: Dipl.-Ing. or MSc)
Sep. 1997 - Juni 2005	Bundesrealgymnasium St. Veit/Glan (High school, A-Level)

Work Experience

Since Oct. 2012	Junior Lecturer for Mechanics and Materials Science – Carinthia University of Applied Sciences, Engineering & IT
Dec. 2012 – Sep. 2012	Project assistant in the CDL AOS – Institute of Material Science and Technology, Vienna University of Technology Preparing my PhD thesis in the area of hard AlCrN and AlCrO coatings synthesized by cathodic arc evaporation Supervision of Master students

Jan. 2012 – Nov. 2012	Project assistant in the CDL AOS – Department of Physical Metallurgy and Materials Testing, Montanuniversität Leoben Preparing my PhD thesis in the area of hard AlCrN and AlCrO coatings synthesized by cathodic arc evaporation
Juli 2010 – Dez. 2011	Student assistant/graduate, Department Physical Metallurgy and Materials Testing – Montanuniversität Leoben Preparing my diploma thesis in the area of thin films/coating technology (PVD-systems): „Sputtered $\text{Cr}_{1-x}\text{Al}_x\text{N}$ hard coatings with $0.21 \leq x \leq 0.46$ “
Nov. 2008 – Juli 2010	Student assistant, Materials Centre Leoben In the area of surface science, working on thin film characterization and testing
Apr., Juli – Sept. 2009	Internship in Laboratory, Molemab Inotech Schleifmittelindustrie GmbH Materials testing and quality control
Apr., Juli – Sept. 2008	Internship in Laboratory, Molemab Inotech Schleifmittelindustrie GmbH Materials testing and quality control
Juli 2007 – Sept. 2007	Internship in Laboratory, Molemab Inotech Schleifmittelindustrie GmbH Materials testing and quality control
Jan. 2002 - Aug. 2006	Various summer jobs (service in restaurants)

Teaching Experience

2014	Materials Testing Lab (1.5 ECTS), Lecturer
2012	Thin Films Fundamentals and Characterization Lab (1 ECTS), Co-Lecturer

Supervised Masterstudents

C. Steinkellner	Diffusion of Fe, Cr, and C in arc evaporated TiN and TiAlN coatings and the influence on microstructure and hardness
B. Larrieu	Influence of annealing temperature on structure and mechanical properties of CrN and CrAlN coatings